DISPERSOID STABILITY IN ION IRRADIATED OXIDE DISPERSION STRENGTHENED ALLOYS

A Dissertation

by

HYOSIM KIM

Submitted to the Office of Graduate and Professional Studies of
Texas A&M University
in partial fulfillment of the requirements for the degree of

DOCTOR OF PHILOSOPHY

Chair of Committee,	Lin Shao
Committee Members,	Kenneth L. Peddicord
	Sean M. McDeavitt
	Ibrahim Karaman
Head of Department,	John E. Hurtado

May 2019

Major Subject: Nuclear Engineering

ABSTRACT

The purpose of this study is to evaluate oxide dispersoid stability in oxide-dispersoid-strengthened (ODS) alloys under different ion irradiation conditions. ODS alloys are considered as future generation IV reactor cladding and in-core structure materials due to their good swelling resistance and high temperature strength. The ferritic-martensitic (FM) 12Cr ODS alloy which has uniform distribution of oxide dispersoids in both phases was selected for this study. Previous studies on this alloy have shown good void swelling resistance after 800 peak dpa Fe ion irradiation at high temperature and have revealed equilibrium oxide dispersoid size dependency of irradiation temperature. It is also found that equilibrium size is closely related to a coherency with matrix. In this study, oxide dispersoid size and density of coherent and incoherent dispersoids were further studied and analyzed as a function of depth for both phases after ion irradiation. Furthermore, He preimplantation study was conducted to see how preimplanted He bubbles affect coherent dispersoid size and density under irradiation in TM phase, since He is generated by (n,α) transmutation in real reactor which causes He embrittlement. The study revealed that He implantation itself does not affect dispersoid size or density, but subsequent ion irradiation after 1×10^{15} ions/cm^2 leads to oxide dispersoid density increase, while 1×10^{16} ions/cm^2 does not, suggesting that small bubbles promote nucleation of coherent oxide dispersoid.

Other factors that affect equilibrium dispersoid size are dpa rate and damage cascade factor. The effect of dpa rate on dispersoid size and density was studied on Hf

doped ODS alloy, and coherent and incoherent particle size and density were studied as a function of local dpa rate (depth). The result showed no noticeable difference on dpa rate, and in order to explain the experimental observations, defect-assisted-diffusion mechanisms were taken into consideration. A high dpa rate results in enhanced dispersoid dissolution, while dispersoid recovery is increased due to defect-assisted diffusion. Therefore, the two effects are balanced, leading to a relative insensitivity of dispersoid size to dpa rate. The result showed the possibility of utilizing ion accelerator on studying ODS alloys to predict their behavior in real reactor environment.

DEDICATION

This dissertation is dedicated to my family who has supported me with their love and strong belief in me throughout 5 years of doctoral program from a distance. I thank my partner who has stood by me giving encouragement and great help whenever I felt lost in graduate school. Without their love and support, it would be very hard to achieve goals and chase my dream in United States.

I would also like to thank all my advisors and colleagues who have helped me to grow up to become a better researcher by being a good companion and role model. I have not only learned a lot of knowledge from them, but also they motivated me with their self-motivated and proactive attitude and passion toward research. It was always pleasurable to work with them on the accelerator and microscopies day and night.

ACKNOWLEDGEMENTS

I greatly thank my advisor and committee chair Dr. Lin Shao for his guidance and support throughout my PhD research. I have always felt very honored and grateful to be in his group, and the lessons he taught will be never forgotten by me. He has been a very good role model and he always tried his best to make his students become successful in graduate school and even careers after. He is and definitely will be one of the best mentors I have ever met in my life.

I would like to also thank to my committee members, Dr. Peddicord, Dr. McDeavitt, and Dr. Karaman for taking their precious time to guide my research by providing helpful advises, and to attend preliminary exam and final exam among their busy schedules.

I cannot thank enough to Dr. Frank A. Garner for his guidance on my research projects. His passion on research inspires me and I have always enjoyed having a phone call discussion with him every week. His deep and wide knowledge on nuclear materials always astonished me and made me feel humble and motivated.

Thanks also go to my friends and colleagues who helped me to grow up, especially Jonathan Gigax and Tianyi Chen for teaching and guiding me to become better at accelerator and microscopies. Their self-motivation and passion on research also motivated me and learning from them and working with them have been always a pleasure.

I would like to thank faculties and staffs in our department for their effort toward high quality classes, great learning environment and for their support during my PhD. I

appreciate MIC (Microscopy Imaging Center) and MCF (Materials Characterization Facility) staffs for their help on research, especially thank to Dr. Hansoo Kim and Dr. Winson Kuo for TEM and FIB training and the helps.

CONTRIBUTORS AND FUNDING SOURCES

Contributors

This work was supervised by a dissertation committee consisting of Professors Lin Shao, Kenneth L. Peddicord and Sean M. McDeavitt of the Department of Nuclear Engineering and Professor Ibrahim Karaman of the Department of Material Science and Engineering.

The data depicted in Chapter 1.2.3 Previous work was conducted by Tianyi Chen of Department of Nuclear Engineering who was a former student of our lab and those results were published in 2015 and 2016. Some of his work were introduced in this dissertation with a permission of copyright holder.

Lab manager Xuemei Wang, and my colleagues, Jonathan Gigax and Tianyao Wang, helped me greatly with accelerator operation and beam watching on 1.7 MV and 140 kV.

All other work conducted for the dissertation was completed by the student independently.

Funding Sources

This study was supported by the United States National Science Foundation through grant number 1708788, and also by US Department of Energy Office of Basic Energy Sciences, under grant number DE-SC0006725. The contents inside are solely the

responsibility of the authors and do not necessarily represent the official view of the United States Government.

NOMENCLATURE

APT	Atom Probe Tomography
ATR	Advanced Test Reactor
BCC	Body Centered Cubic
BF	Bright Field
DF	Dark Field
dpa	displacements per atom
EDS	Energy Dispersive Spectroscopy
EELS	Electron Energy Loss Spectroscopy
EFTEM	Energy Filtered Transmission Electron Microscopy
FCC	Face Centered Cubic
FEG	Field Emission Gun
FFT	Fast Fourier Transform
FIB	Focused Ion Beam
FM	Ferritic Martensitic
Gen IV	Fourth Generation reactors
GFR	Gas-cooled Fast Reactor
GIF	Generation IV International Forum
GIS	Gas Injection System
HRTEM	High Resolution Transmission Electron Microscopy
IVAS	Integrated Visualization and Analysis Software

LEAP	Local Electrode Atom Probe
LFR	Lead-cooled Fast Reactor
LWR	Light Water Reactor
MSR	Molten Salt Reactor
O	Oxygen
ODS	Oxide Dispersion Strengthened
Pt	Platinum
PWR	Pressurized Water Reactor
SCWR	Super Critical Water Reactor
SE	Secondary Electron
SEM	Scanning Electron Microscopy
SFR	Sodium-cooled Fast Reactor
SiC	Silicon carbide
SNICS	Source of Negative Ions by Cesium Sputtering
SRIM	Stopping and Range of Ions in Matter
STEM	Scanning Transmission Electron Microscopy
TEM	Transmission Electron Microscopy
Ti	Titanium
VHTR	Very High Temperature Reactor
WBDF	Weak Beam Dark Field
Y	Yttrium

TABLE OF CONTENTS

Page

LIST OF FIGURES

Page

LIST OF TABLES

Page

1. INTRODUCTION

The need for cladding and structural materials that can withstand high temperature and high radiation environment has been increasing in nuclear material field for future Gen IV and fusion reactors. This chapter provides background knowledge about some advanced Gen IV reactors and ODS alloy which is the one of the promising candidate alloys for Gen IV and fusion reactors. Previous studies on ODS alloys, especially 12Cr ODS alloy, will be briefly introduced.

1.1. Advanced Reactors

1.1.1. Background

The nuclear energy is one form of energy sources that we have been heavily relied on to get an electricity. There are about 450 operable fission reactors worldwide, producing about 396,446 MWe which is approximately 10.5 % of global electricity [1]. Nuclear fission reactors have been proven its safety and sustainability during past 60 years, and with the increasing demand of clean energy, about 55 more reactors are under construction worldwide as of 2019 [1]. The current commercial reactors that were built and are under constructions are mostly Gen II or Gen III PWR and LWR. To further improve current fission reactor designs for better safety, efficiency and sustainability, the Gen IV reactors have been proposed and coordinated by Generation IV International Forum (GIF). The six Gen IV reactors are VHTR, SFR, SCWR, GRF, LFR and MSR and, these designs produce radioactive nuclear wastes that decay within few centuries instead of millennia while having 100 to 300 times more energy yield from the same amount of

fuel [2,3]. For reactor designs like SFR, GRF, LFR and MSR which have closed fuel cycle allow decrease fuel waste volume and fuel refilling cost.

However, those new Gen IV reactors require higher operation temperature and the damage generated from thermal and fast neutrons is much higher than conventional PWR and BWR reactors as shown in Figure 1.1 [4]. The expected inlet and outlet temperature range is 290-1000 ℃, and the expected highest neutron dose is 200 dpa, which is not acceptable for current nuclear materials that have been used in the reactors. On top of this, accident tolerant reactor concept uses corrosive chemicals such as sodium, lead bismuth, and molten salt as a coolant to reduce a risk of hydrogen gas production and also these type of reactors does not have geological limitation on construction site, as they do not need a massive amount of water as a coolant. Therefore, future material challenges come from various aspects, and the key for feasibility and sustainability of these future reactors depends on the nuclear material lifetime.

Among these Gen IV reactors, SCWR, SFR, and LFR where fast neutron is utilized and the operation temperature and neutron dose are high (290-800 ℃, over 200 dpa) are the reactor types that ODS alloys are expected to be used as a cladding material or an in-core structural material [4,5]. In next section, therefore, principle and brief background of each reactors will be introduced.

Table 3
Reactor core environment and materials for light water reactors and advanced fission reactor concepts [7].

System	Coolant	Pressure (MPa)	T_{in}/ T_{out} (°C)	Neutron spectrum, maximum dose (dpa)	Fuel	Cladding
Pressurized water reactor – PWR	Water – single phase	16	290/ 320	Thermal, ~80	UO_2 (or MOX)	Zirconium alloy
Boiling water reactor – BWR	Water – two phase	7	280/ 288	Thermal, ~7	UO_2 (or MOX)	Zircaloy
Supercritical water cooled reactor – SCWR	Supercritical water	25	290/ 600	Thermal, ~30, fast, ~70	UO_2	F-M (12Cr, 9Cr, etc.) (Fe–35Ni–25Cr–0.3Ti), Incoloy 800, ODS, Inconel 690, 625, and 718
Very high temperature reactor – VHTR	Helium	7	600/ 1000	Thermal, <20	UO_2, UCO	SiC or ZrC coating and surrounding graphite
Gas fast reactor – GFR	Helium, supercritical CO_2	7	450/ 850	Fast, 80	MC	Ceramic
Sodium fast reactor – SFR	Sodium	0.1	370/ 550	Fast, 200	MOX or U–Pu–Zr or MC or MN	F-M or F-M ODS
Lead fast reactor – LFR	Lead or lead–bismuth	0.1	600/ 800	Fast, 150	MN	High-Si F-M, ODS, ceramics, or refractory alloys
Molten salt reactor – MSR	Molten salt, for example: FLiNaK	0.1	700/ 1000	Thermal, 200	Salt	Not applicable

System	Structural materials	
	In-core	Out-of-core
Pressurized water reactor – PWR	Stainless steels, nickel-based alloys	Stainless steels, nickel-based alloys
Boiling water reactor – BWR	Stainless steels, nickel-based alloys	Stainless steels, nickel-based alloys
Supercritical water cooled reactor – SCWR	Same as cladding options, plus low swelling stainless steels	F-M, low-alloy steels
Very high temperature reactor – VHTR	Graphites, PyC, SiC, ZrC, vessel: F-M	Ni-based superalloys, 32Ni–25Cr–20Fe–12.5W–0.05C, Ni–23Cr–18W–0.2C, F-M w/thermal barriers, low-alloy steels
Gas fast reactor – GFR	Refractory metals and alloys, Ceramics, ODS, vessel: F-M	Ni-based superalloys, 32Ni–25Cr–20Fe–12.5W–0.05C, Ni–23Cr–18W–0.2C, F-M w/therm barriers
Sodium fast reactor – SFR	F-M ducts, 316SS grid plate	Ferritics, austenitics
Lead fast reactor – LFR		High-Si austenitics, ceramics, or refractory alloys
Molten salt reactor – MSR	Ceramics, refractory metals, Mo, Ni-alloys, (e.g., INOR-8), graphite, Hastelloy N	High-Mo, Ni-based alloys (e.g., INOR-8)

Abbreviations: F-M, Ferritic–martensitic stainless steels (typically 9–12 wt.% Cr); ODS, oxide dispersion-strengthened steels (typically ferritic–martensitic); MC, mixed carbide (U,Pu)C; MN, mixed nitride (U,Pu)N; MOX, mixed oxide $(U,Pu)O_2$.

Figure 1.1 A table shows reactor core environment and materials for LWR and advanced fission reactor concepts (adapted with permission) [4].

1.1.2. SFR, LFR and SCWR

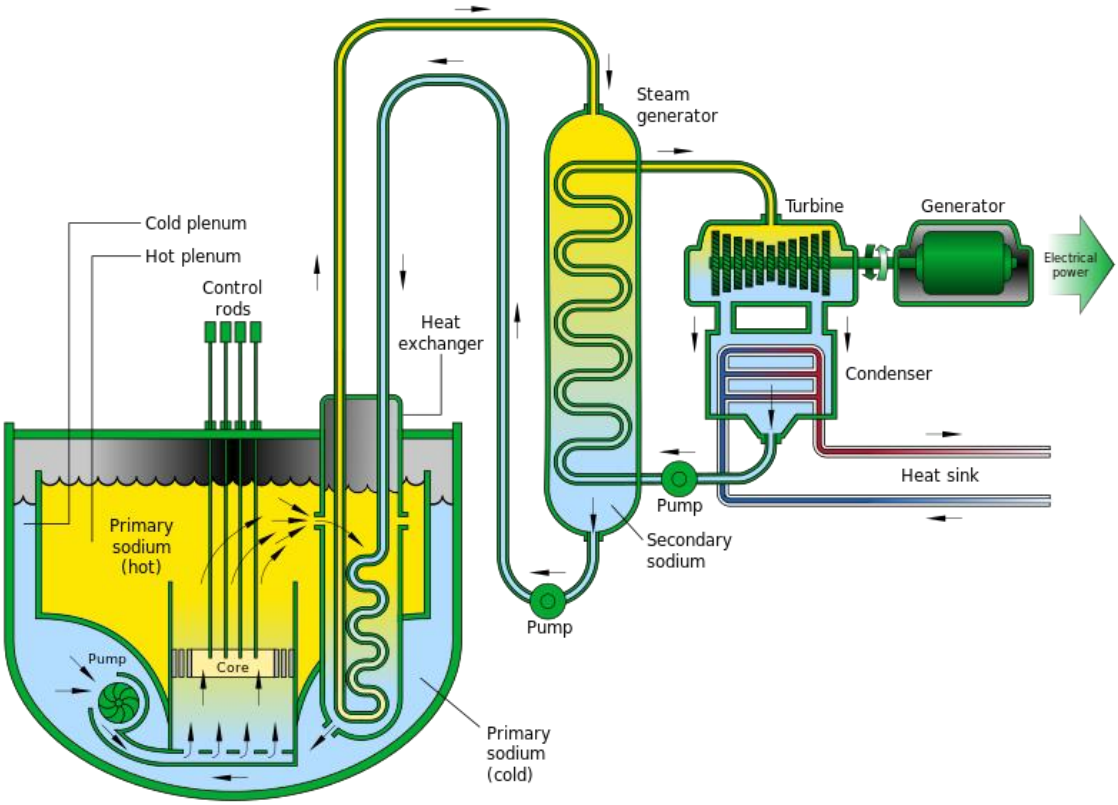

Figure 1.2 A schematic of sodium-cooled fast reactor [6].

Figure 1.2 provides a schematic of typical SFR. The SFR utilized liquid sodium as a reactor coolant and it can be operated at low pressure with high power density. As shown in Fig. 1.2, whole system needs to be a closed system to prevent chemical reaction with air and water [7,9]. The advantages of this reactor design are: (1) sodium has low neutron absorption cross-section and its isotope decays fast to stable element, (2) sodium has high boiling point and it does not need to be pressurized, (3) sodium has excellent heat transfer properties, and (4) fast neutrons can consume transuranic elements reducing a nuclear

waste. The down side is the risk of using chemically reactive sodium, and if sodium is exposed to water, it generates sodium hydroxide and hydrogen [7,9].

As the outlet temperature is about 550 ℃, the cladding and structural materials are exposed to high temperature during operation, and due to the nature of utilizing fast neutron, the materials will get high level of radiation, reaching 200 dpa. As ferritic ODS alloys have shown very good swelling resistance under high dose irradiations, it can be a

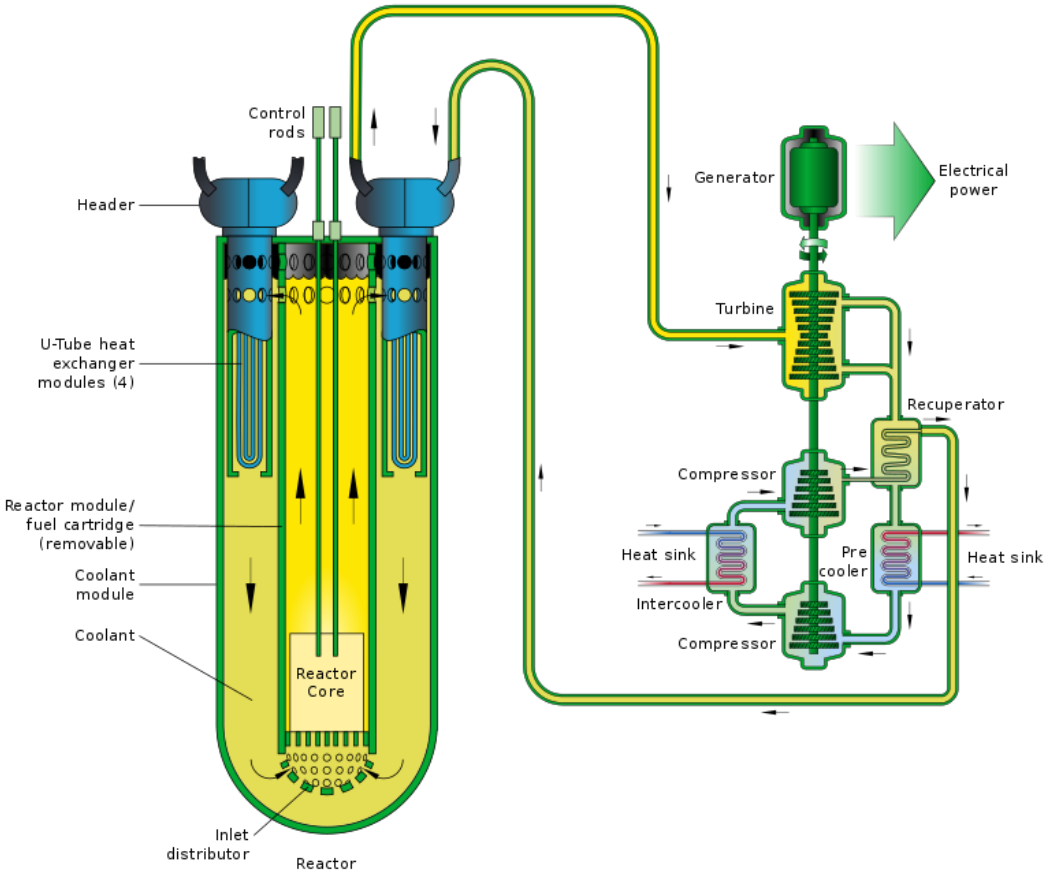

Figure 1.3 A Schematic of lead-cooled fast reactor [6].

good candidate material for this type of reactor, and also due to its high temperature strength and creep resistance, it is suitable to use under high temperature.

Figure 1.3 shows a schematic of typical LFR, and it uses liquid lead or lead-bismuth eutectic as a coolant. As all liquid metals do, the heat transfer is superior and they both have low neutron absorption with low melting temperature and high boiling point. It is operable under low pressure, and safer than sodium when exposed to air and water [7,8]. This reactor concept, however, has some disadvantages: (1) lead and lead-bismuth are heavy and require more structural support which increases building cost, (2) bismuth is expensive and a rare element compare to lead or sodium, (3) solidification and leaking can cause a damage on reactor, and (4) lead-bismuth produces radioactive element polonium [7,8].

The reactor outlet temperature is higher than SFR ranging from 500-800 ℃, and it is also expected to get a high dose of radiation from fast neutron reaching 150 dpa. For the same reason with SFR, ferritic ODS alloys are the promising candidate material for this design.

Figure 1.4 shows a schematic of SCWR. From the advantage of using water as a coolant, this reactor design can be either thermal or a fast neutron reactor depending on the fuel core design. Difference between current LWR and SCWR is that SCWR is operated at supercritical pressure. The water temperature is above critical point but under very high pressure which makes it possible to become a superheated steam from liquid water. Then, the superheated steam will be supplied to turbine directly to generate electricity [7]. Thanks to its design, the efficiency reaches over 44 %, higher than current

reactors (34-36 %). It can also be a breeder reactor when it is utilizing fast neutrons. However, its high pressure and high temperature design challenges reactor component materials greatly. Therefore, materials that can withstand high mechanical and thermal stress are needed for fuel cladding and in-core structural materials, and this is why ferritic ODS alloys are also a good candidate for this reactor type due to the superior properties mentioned above [8].

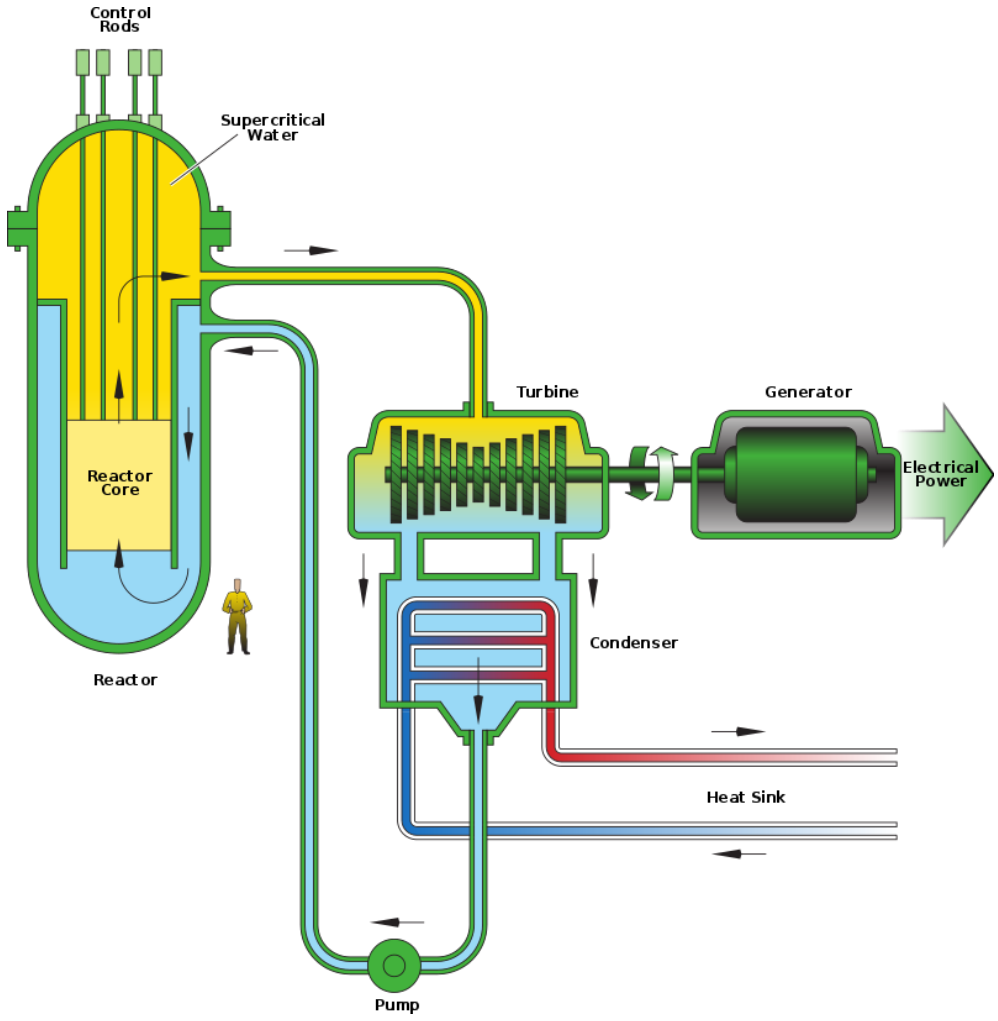

Figure 1.4 A schematic of Supercritical Water Reactor [6].

1.2. Ferritic ODS Alloy

1.2.1. Background

ODS alloy is first developed in 1996 by company called INCO, and they used mechanical alloying (MA) process to fabricate it. Details on current MA process is introduced in section 2.1.1. Until the current ODS alloys are developed, there have been many trial and errors in fabrication and testing process. For example, one of the previous studies on MA957 ODS alloy showed that the uniformity and stability of dispersoids are very important to suppress swelling under irradiation [10]. The MA957 ODS alloy showed varying levels of dispersoids in each ferrite grains prior to irradiation, and after 400 dpa irradiation at 450 ℃, each grain showed different swelling behavior due to different dispersoid levels. The grains contain more oxide dispersoids swelled less than those with less oxide dispersoids.

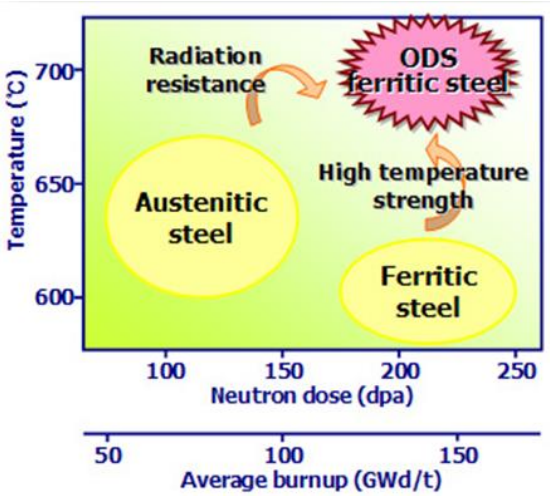

Figure 1.5 A schematic shows the temperature and neutron dose range where each steel can be used [13].

It is well known that ferritic-martensitic (F/M) dual-phase alloy are good at good swelling resistance at high temperature [11,12]. F/M steels also have higher thermal conductivity and lower expansion coefficients than those of austenitic steels [11,12], which is appealing to be used as future reactor cladding or in-core structural materials. Especially tempered martensite phase has shown superior void swelling resistance compared to ferrite phase when they were irradiated at the same condition. As shown in Figure 1.6, the austenitic steels are good for high temperature environment, but they are susceptible to high dose radiation. In contrast, ferritic steels are known to be resistant at void swelling but the operation temperature is only limited to less than 600 ℃ because of their mechanical property deterioration. To overcome this problem, ferritic ODS steels have been developed and tested, and they showed good high temperature strength while maintaining good radiation resistance. During this process, introducing oxide dispersoids uniformly within both ferrite and martensite phase was a challenging part. Recently, dual-phase 12Cr ODS alloy was successfully developed [14,15], and small size of oxide dispersoids are evenly distributed in both ferrite and tempered martensite phases [16,17]. Self-ion irradiation test at high temperature and high damage level demonstrated good swelling resistance behavior of this alloy in recent studies [16,17], and will be further introduced in section 1.2.3.

1.2.2. Benefits of ODS alloy

The oxide dispersions help stabilizing grain boundaries and block dislocation motion so that the dislocation can act as a point defect recombination site. Oxide dispersion itself can act as a defect sinks for point defects trapping and defect annihilation

[18-20]. Figures 1.7 provide TEM bright field images of two as-received Japanese alloys, SP10 (left) and 15Cr (right) ODS alloys. Left figure shows oxide dispersoids located on the grain boundary marked with three red arrows, which further prevent grain growth under high temperature and high dose irradiation environment. The right figure reveals that oxide dispersoids hinder dislocation movement with oxide dispersoids marked by yellow dashed circles.

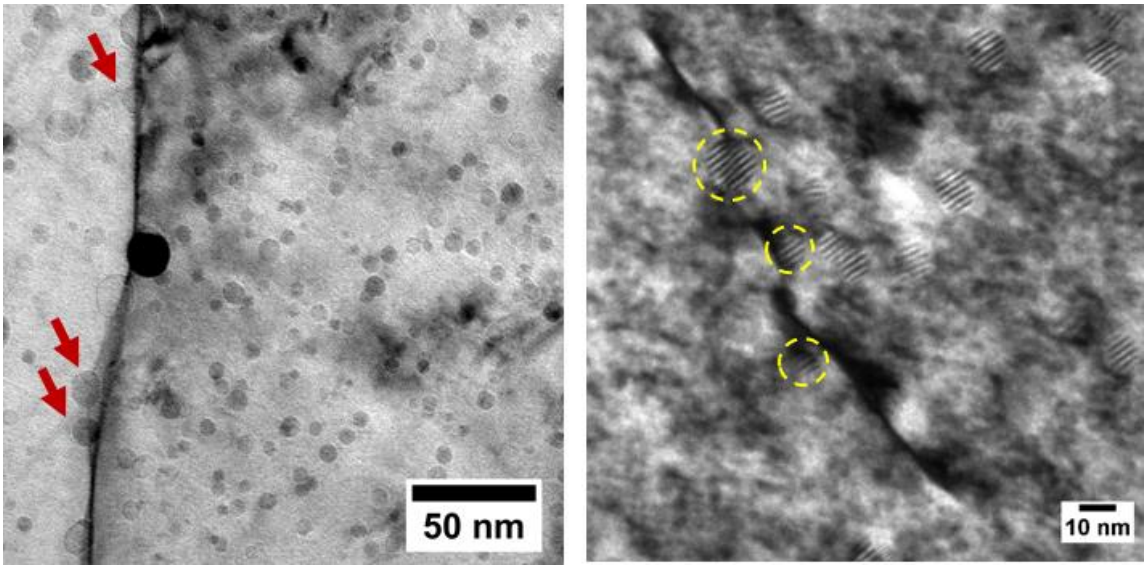

Figure 1.6 TEM bright field images of as-received SP10 alloy (left) and as-received 15Cr ODS alloy (right). Red arrows and yellow dashed circles are all indicating oxide dispersoids.

Due to those effects of oxide dispersoids, ODS variant alloy shows better swelling resistance behavior than ODS non-variant part. As an example, 18Cr10NiTi austenitic steel was compared against its ODS variants in Figure 1.8 in terms of void swelling. With increasing dpa, non-ODS austenitic steel shows very short transient regime and reaches

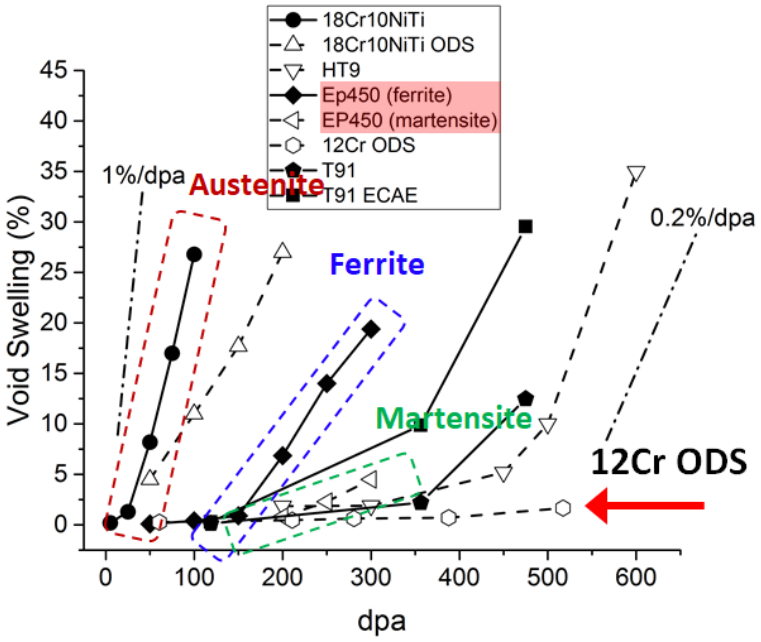

Figure 1.7 Void swelling as a function of dpa for various alloys (adapted with permission) [21,22].

steady-state swelling rate for austenitic steel (1%/dpa) at 50 dpa. On the other hand, its ODS variant showed less steep slope of swelling compared to non-ODS alloy, and also it does not show 1%/dpa swelling rate anymore. The comparison of two different phases in EP450 Russian alloy revealed that martensite phase has much stronger void swelling resistance than ferrite phase. The alloy that shows the most swelling resistance behavior is the 12Cr ODS alloy which was introduced earlier. Even after 500 dpa irradiation, the void swelling did not even reach 2.5 % for this alloy. Along with swelling resistance property, the ODS alloys have also shown a superior high temperature strength and creep resistance [18,23-25], which make them a very promising candidate alloy for future Gen IV and fusion reactors. For example, Russian dual-phase FM alloy EP-450 and its ODS

variant showed very different creep behavior under high temperature and stress as shown in Figures 1.9 [26]. The Fig. 1.9(a) shows deformation of both EP-450 and ODS variant alloys as a function of time under 650 ℃ and 140 MPa stress. The EP-450 alloy showed more than 10 % deformation before time reaches 500 hrs, while EP-450 ODS showed only 2 % deformation even after 4000 hrs. At 700 ℃ and 120 MPa, EP-450 showed more dramatic deformation rate reaching 20 % of deformation within 10 h of exposure with creep rate of 9.1 %/h, and ODS variant showed very low creep rate of 1.82×10^{-3} %/h showing three orders of magnitude difference compared to non-ODS variant.

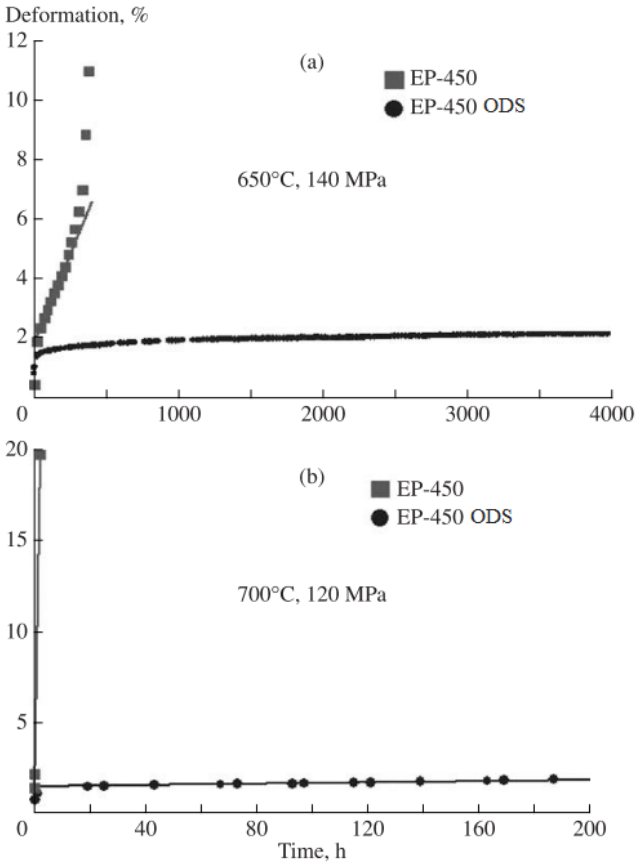

Figure 1.8 Thermal creeps of EP-450 and EP-450 ODS alloys obtained at (a) 650 ℃ and 140 MPa, and (b) 700 ℃ and 120 MPa (reprinted with permission) [26].

1.2.3. Previous work

Since chapter 3 and 4 are closely related to the previous studies on 12Cr ODS alloy, this section will briefly introduce and summarize those previous works done by our group [16,17]. Figures 1.10 show different void swelling behavior of ferrite and tempered martensite phases after the similar irradiation doses. Ferrite grain showed increasing void

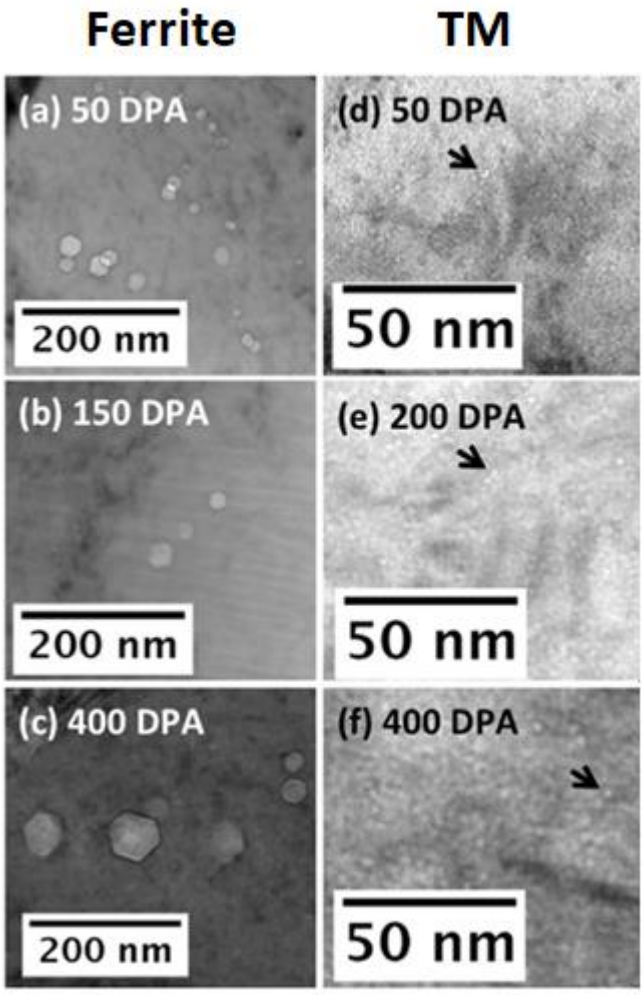

Figure 1.9 TEM micrographs obtained from 500 nm depth region of 100, 300, and 800 peak dpa irradiated sample from (a-c) ferrite grains and (d-f) tempered martensite grains (adapted with permission) [16].

size with increasing local dpa values. TM phase did not show any large void as shown in the ferrite phase, and instead, small size microcavities were observed.

Figures 1.11 provide void swelling as a function of depth, and the top figure is from ferrite phase and the bottom figure is from TM phase. In ferrite phase, with increasing damage level, void swelling tends to increase too although there are some fluctuations between doses. The TM grain showed a similar trend, however, the maximum swelling was about 0.06 % which is much lower than the maximum swelling of ferrite phase (1.6

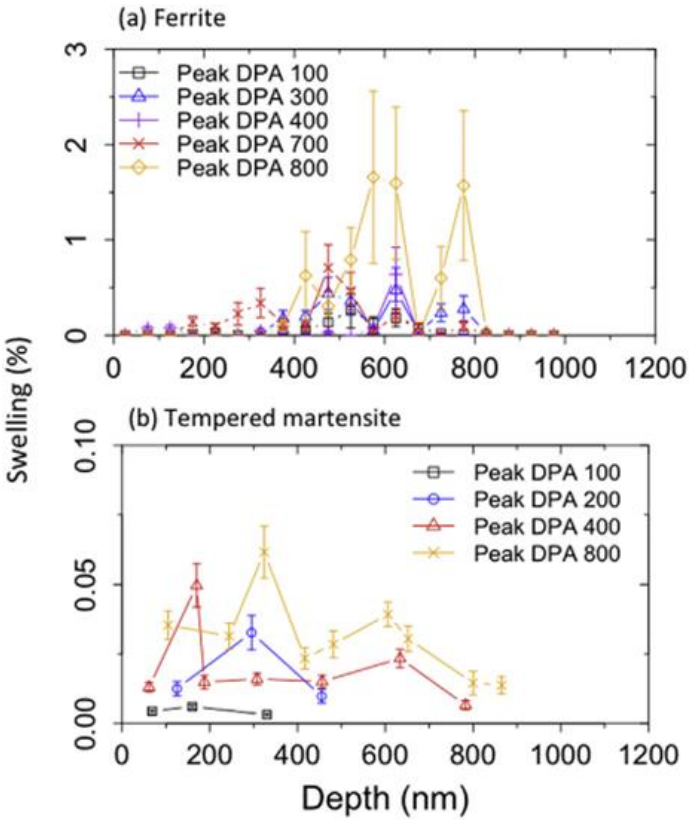

Figure 1.10 Oxide dispersoid size distribution of TM phase of (a) unirradiated sample and (b) 100 local dpa irradiated sample at 475 ℃ (reprinted with permission) [17].

%). Considering that the maximum peak dpa was 800, both phases showed very high swelling resistance behaviors.

In oxide dispersoid stability wise, both ferrite and TM phase dispersoids showed shrinkage in their size after irradiation, and the change was more dramatic for TM phase where large size oxide dispersoids were observed as shown in Figures 1.12. Those large oxide dispersoids in TM phase are mostly incoherent as shown in Figures 1.13. The Fig. 1.13(a) shows unirradiated martensite phase dispersoid size distribution, and large size dispersoid was not coherent with matrix (110), while small size dispersoids are mostly

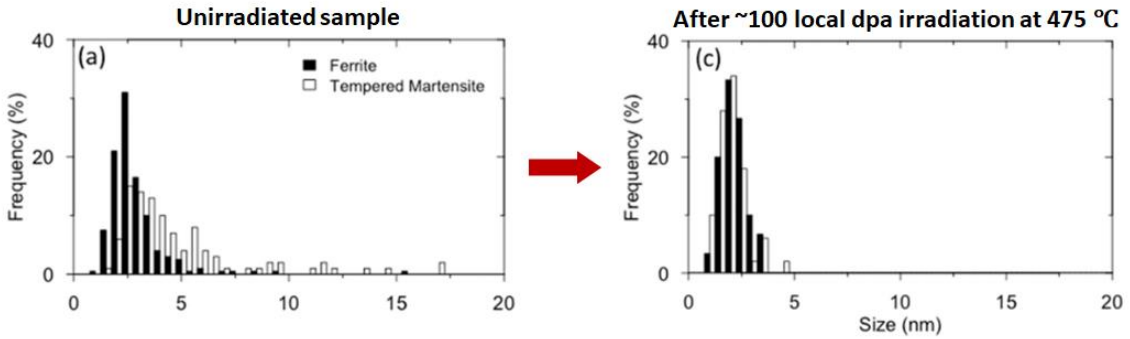

Figure 1.11 Oxide dispersoid size distribution of (a) unirradiated sample and (c) 100 local

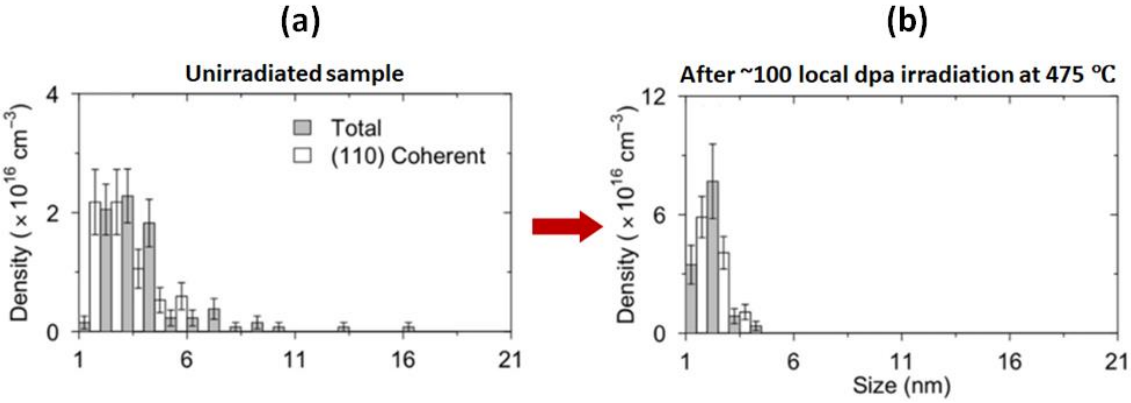

Figure 1.12 Oxide dispersoid size distribution of TM phase of (a) unirradiated sample and (b) 100 local dpa irradiated sample at 475 ℃ (adapted with permission) [17].

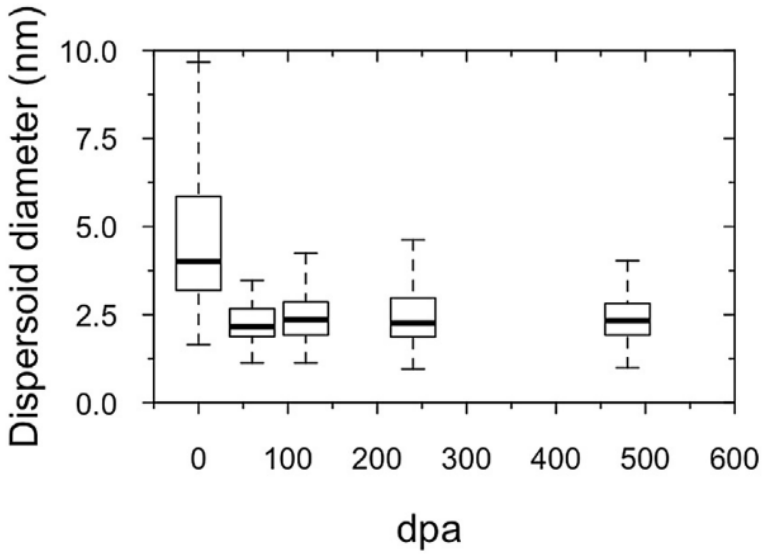

Figure 1.13 Dispersoid diameter as a function of increasing dpa in TM phase (reprinted with permission) (reprinted with permission) [16].

coherent with matrix. Comparison with the irradiated sample (Fig. 1.13(b)) tells us that large incoherent dispersoids are not stable under high temperature irradiation and only coherent small size dispersoids remain. As a follow-up study, the study on dispersoid coherency of each phase as a function of irradiation depth was conducted and the results are presented in chapter 3, since the previous study only focused on dispersoid coherency of TM phase at one certain depth and damage level.

Another thing we have learned from previous study is that the dispersoid size change reaches equilibrium state after ~60 dpa of self-ion irradiation at high temperature as shown in Figure 1.14. They showed a size reduction after 60 dpa, but the mean size and size distribution remained almost the same afterwards even at 500 dpa. Another temperature dependent study revealed that dispersoid equilibrium size varies with

irradiation temperatures. Figure 1.15 shows that the equilibrium dispersoid size is larger at higher temperature, and with decreasing temperature, equilibrium size also decreases. This dispersoid equilibrium size temperature dependent behavior was further explained by radiation induced dispersoid shrinkage equation and the thermal diffusion model from Gibbs and Thomson effect as shown in Figures 1.16. When those two terms are in equilibrium state, the equilibrium dispersoid size r can be represented by a curve. The dispersoid inside a curve will grow, while the dispersoids outside of curve will shrink. Then, the right figure in Fig. 1.16 plots numerical solutions of equilibrium states with varying irradiation conditions. When the temperature increases and other conditions are the same, diffusion coefficient D will also increase, leading equilibrium size curve to

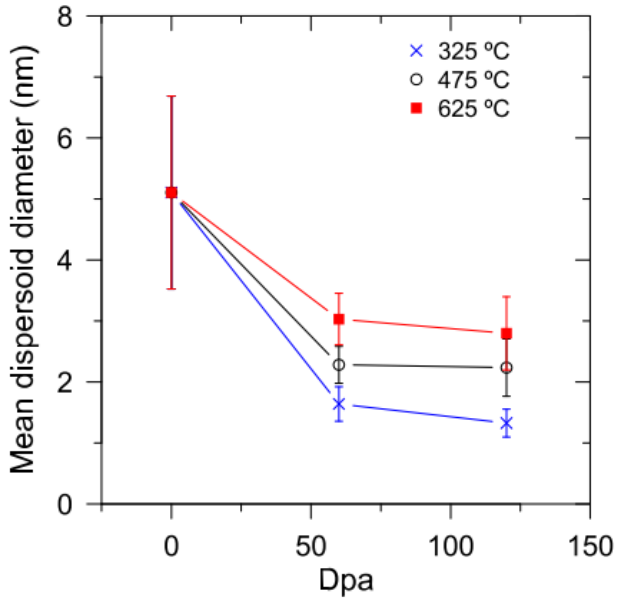

Figure 1.14 Mean dispersoid diameter as a function of increasing dpa with varying irradiation temperatures (reprinted with permission) [17].

change from black solid line to red dashed line, which means that equilibrium size is larger at elevated temperature. To see the other irradiation parameter effects on dispersoid equilibrium size, dpa rate K is further studied in chapter 5 on Hf-doped ODS alloy.

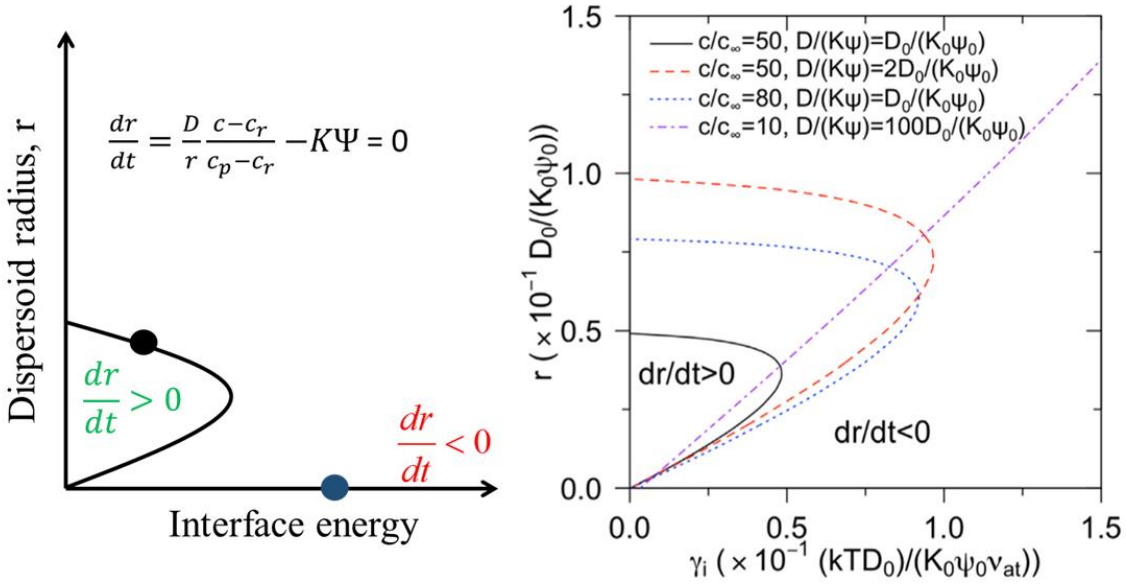

Figure 1.15 A schematic and equation showing the relationship between dispersoid radius and interfacial energy (left) and its numerical solutions at different irradiation conditions (right) (adapted with permission) [17].

1.3. References

[1] Reactor Database, www.world-nuclear.org, 2019.

[2] S. J. Zinkle, J. T. Busby, Structural materials for fission & fusion energy, Materials Today 12 (2009) 12-19.

[3] S. J. Zinkle, L. L. Snead, Designing radiation resistance in materials for fusion energy, Annu. Rev. Mater. Res. 44 (2014) 241–267.

[4] S. J. Zinkle, G. S. Was, Materials challenges in nuclear energy, Acta Mater. 61 (2013) 735-758.

[5] T. R. Allen, J. Gan, J. I. Cole, S. Ukai, S. Shutthanandan, S. Thevuthasan, The stability of 9Cr-ODS oxide particles under heavy-ion irradiation, Nucl. Sci. and Engin. 151 (2005) 305-312.

[6] T. Abram, S. Ion. Generation-iv nuclear power: A review of the state of the science. Energy Policy 36 (2008) 4323-4330.

[7] J. E. Kelly, Generation IV international forum: A decade of progress through international cooperation, Progress in Nucl. Energy 77 (2014) 240-246.

[8] J. Kaneda, S. Kasahara, F. Kano, N. Saito, T. Shikama, H. Matsui, Material development for supercritical water-cooled reactor, Proc. ISSCWR-5, Vancouver, Canada, 13-16 March 2011.

[9] A. Alemberti, V. Smirnov, C. F. Smith, M. Takahashi, Generation IV - Overview of lead-cooled fast reactor activities. Prog. Nucl. Energy 77 (2014) 300-307.

[9] K. Aoto, P. Dufour, Y. Hongyi, J. P. Glatz, Y. Kim, Y. Ashurko, R. Hill, N. Uto, A summary of sodium cooled fast reactor development. Prog. Nucl. Energy 77 (2014) 247-265.

[10] F. A. Garner, The challenge of using ion irradiation to develop and test advanced alloys for application to very high neutron exposures in future reactor concepts, pp. 4-22, in INTERNATIONAL ATOMIC ENERGY AGENCY, Accelerator Simulation and Theoretical Modelling of Radiation Effects in Structural Materials, Nuclear Energy Series No. NF-T-2.2, IAEA, Vienna (2018).

[11] R. L. Klueh, A. T. Nelson, Ferritic/martensitic steels for next-generation reactors, J. Nucl. Mater. 371 (2007) 37-52.

[12] A technology roadmap for Generation IV nuclear energy systems, US DOE NERAC and Generation IV International Forum, GIF-002-00, 2002.

[13] Web image, https://www.jaea.go.jp/english/news/p06101302/z1.jpg (2018).

[14] R. L. Klueh, D. R. Harries, High-chromium ferritic and martensitic steels for nuclear applications, ASTM International, West Conshohocken, PA, 2001.

[15] S. Ukai, Y. Kudo, X. Wu, N. Oono, S. Hayashi, S. Ohtsuka, T. Kaito, Residual ferrite formation in 12Cr ODS steels, Journal of Nuclear Materials 455 (2014) 700–703.

[16] T. Chen, E. Aydogan, J. G. Gigax, D. Chen, J. Wang, X. Wang, S. Ukai, F. A. Garner, L. Shao, Microstructural changes and void swelling of a 12Cr ODS ferritic- martensitic alloy after high-dpa self-ion irradiation, J. Nucl. Mater. 467 (2015) 42-49.

[17] T. Chen, J. G. Gigax, L. Price, D. Chen, S. Ukai, E. Aydogan, S. A. Maloy, F. A. Garner, L. Shao, Temperature dependent dispersoid stability in ion- irradiated ferritic-martensitic dual-phase oxide-dispersion-strengthened alloy: coherent interfaces vs. incoherent interfaces, Acta Mater. 116 (2016) 29-42.

[18] G. R. Odette, M. J. Alinger, B. D. Wirth, Recent developments in irradiation- resistant steels, Annu. Rev. Mater. Res. 38 (2008) 471-503.

[19] G. R. Odette, Recent progress in developing and qualifying nanostructured ferritic alloys for advanced fission and fusion applications, JOM 66 (2014) 2427-2441.

[20] C. H. Zhang, Y. T. Yang, Y. Song, J. Chen, L. Q. Zhang, J. Jang, A. Kimura, Irradiation response of ODS ferritic steels to high-energy Ne ions at HIRFL, J. Nucl. Mater. 455 (2014) 61-67.

[21] Y. E. Kupriiyanova, V. V. Bryk, O. V. Borodin, A. S. Kalchenko, V. N. Voyevodin, G. D. Tolstolutskaya, F. A. Garner, Use of double and triple-ion irradiation to study the influence of high levels of helium and hydrogen on void swelling of 8-12% Cr ferritic-martensitic steels, J. Nucl. Mater. 468 (2016) 264-273.

[22] J. G. Gigax, T. Chen, H. Kim, J. Wang, L. M. Price, E. Aydogan, S. A. Maloy, D. K. Schreiber, M. B. Toloczko, F. A. Garner, L. Shao, Radiation response of alloy T91 at damage levels up to 1000 peak dpa, J. Nucl. Mater. 482 (2016) 257-26.

[23] L. K. Mansur, A. F. Rowcliffe, R. K. Nanstad, S. J. Zinkle, W. R. Corwin, R. E. Stoller, Materials needs for fusion, Generation IV fission reactors and spallation neutron sources - similarities and differences, J. Nucl. Mater. 329-333 (2004) 166-172.

[24] J. Chen, P. Jung, T. Rebac, F. Duval, T. Sauvage, Y. de Carlan, M. F. Barthe, Helium effects on creep properties of Fe-14CrWTi ODS steel at 650 ºC, J. Nucl. Mater. 453 (2014) 253-258.

[25] J. Chen, P. Jung, W. Hoffelner, H. Ullmaier, Dislocation loops and bubbles in oxide dispersion strengthened ferritic steel after helium implantation under stress, Acta Mater. 56 (2008) 250-258.

[26] V. S. Ageev, N. F. Vil'danova, K. A. Kozlov, T. N. Kochetkova, A. A. Nikitina, V. V. Sagaradze, B. V. Safronov, V. V. Tsvelev, A. P. Chukanov, Structure and thermal creep of oxide-dispersion-strengthened EP-450 reactor steel, Phys. of Metals and Metallography 106 (2008) 315-325.

2. EXPERIMENT PROCEDURE: EQUIPMENT AND TECHNIQUES

In this chapter, the equipment and techniques used in this research will be introduced in detail from sample preparation to characterization. The sample preparation step is especially very critical to conduct a clean irradiation and it greatly affects entire experiment quality and result. Since we are operating ion accelerator by ourselves to irradiate specimens in Texas A&M accelerator laboratory, it is also important to know how accelerator works and how entire irradiation procedure goes. Using ion accelerator to irradiate sample is a high-cost and time-consuming process. To conduct a successful experiment without failure, good accelerator operating skill and years of experience are essential. Last but not least, obtaining a high quality meaningful data from specimens is crucial to research, and to do that, it is important to know how each equipment works. Principles, background and operating skills on each characterization equipment will be introduced in this chapter.

2.1. Sample Preparation

2.1.1. Alloy Manufacturing

The 12Cr and Hf-doped ODS alloys used in this study were supplied by our collaborator, professor Shigeharu Ukai of Hokkaido University, Japan. These alloys were manufactured by mechanical alloying (MA) method as shown in Figure 2.1 [1]. The ferritic alloy powders were atomized to a size of 150 μm under Ar gas atmosphere and further mixed with 20 nm size Y_2O_3 powder. Those powders were mechanically alloyed using attrition type ball milling and agitated at up to 220 rpm for 48 hrs under high-purity

Ar gas atmosphere. Then, the resulting powder was moved into a steel can, sealed and degassed at 673 K for 2 hrs. After a hot-extrusion at 1423 K, 25 mm diameter consolidated

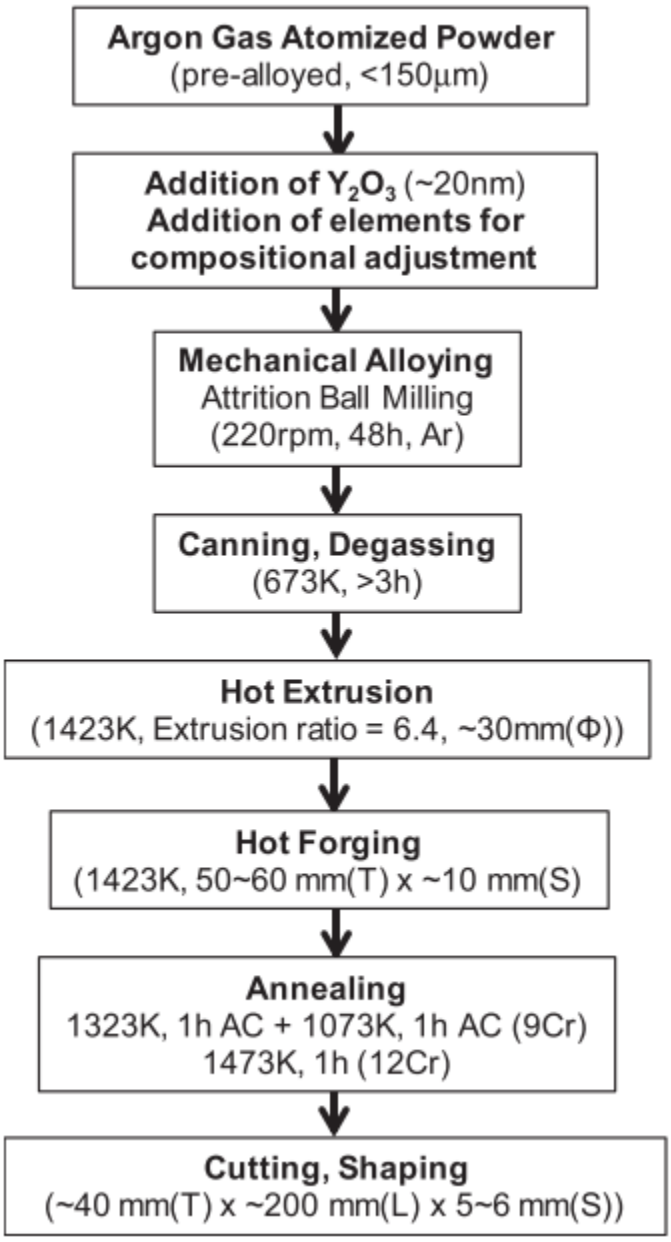

Figure 2.1 Manufacturing process of ODS alloys (reprinted with permission) [1].

bar was made. This bar can be further machined to a mother tube and final cladding tube by cold-rolling and heat treatment.

The ODS alloy samples that were shipped from Japan are 25 mm diameter consolidated bars, and those were further cut and polished to the size suitable for the experiment and post-irradiation characterization which is normally less than 5 mm x 5 mm size. The final chemical composition of 12Cr ODS and Hf-doped ODS alloy will be introduced in Chapter 3 and 5, respectively.

2.1.2. Sample Cutting and Polishing

Prior to surface polishing, samples were cut into 3 mm × 6 mm × 2 mm size by using high-speed manual cut-off saw SYJ-40 (MTI Corporation) in the lab and IsoMet 1000 (Buehler) precision cutter in Microscopy Imaging Center in Texas A&M University. In both machines, silicon carbide (SiC) cut-off blade 80-11195 (Allied) was used. The rough cutting was done using SYJ-40 saw, while precise cutting to a smaller dimension utilized IsoMet 1000, as it uses gravity fed force which gives less deformation during cutting process and also has precise x-axis control.

Samples are mechanically polished by using Nano 2000 polisher (Pace Technologies) and SiC fine grit 8-inch discs. The rough 320 grit is used for grinding down the specimen to certain thickness, and 600 (26 μm), 1200 fine grit (15 μm), 800 (P-2400, 10 μm), 1200 (P-4000, 5 μm) grits are used to further polish down to desired thickness and to remove deformation. As 1200 (p-4000) grit is sputter coated and SiC particles are randomized, it is good for removing deformation. The 1200 fine grit is electrostatically coated and SiC particles are aligned which give more material removal action. Therefore,

1200 fine grit is used after 600 grit, while 1200 (p-4000) grit is used at final step. Then, red final C polishing cloth is used with water-based diamond colloidal suspensions (0.25 micron) followed by silica colloidal suspension (0.04 micron). Specimens are further sonicated by using Ultrasonic cleaner 1510 (Branson) soaked in acetone for 10-15 mins to remove residues, and immediately cleaned by methanol and dried using nitrogen gas spray gun. After this final process, the deformation layer on specimens is mostly removed, and if there is any deformation layer left, electropolishing can be used to chemically etch away the surface.

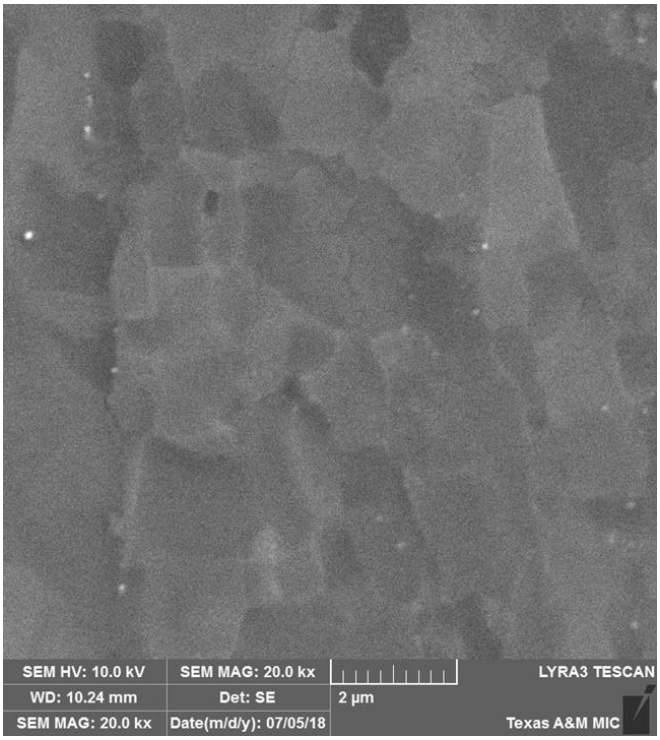

Figure 2.2 SEM SE image of electropolished SOC-14 ODS alloy surface.

Specimens are electropolished by using TenuPol-5 jet electropolisher (Struers) with 5 vol% perchloric acid and 95 vol% methanol. The voltage of 20 V is applied, and polishing is conducted at room temperature or at -20 ℃. After electropolishing, the specimen is rinsed in two methanol containing beakers sequentially to remove any remaining electrolyte.

2.1.3. Sample Surface Quality Examination

To ensure the specimen surface quality before irradiation, secondary electron (SE) beam imaging is used. The Vega 3 SEM (Tescan) and Lyra 3 FIB-SEM (Tescan) are used to check the surface, and if the specimen is well polished without scratch and deformation layer, the grains and grain boundaries are visible under SE image as shown in Figure. 2.2. For this particular image, the Lyra 3 FIB-SEM with 10 kV operation voltage was used. This image is taken from one of the Japanese ODS alloys, SOC-14, after mechanical polishing and electropolishing by the methods introduced in Chapter 2.1.2. The grains are clearly distinguishable from each other and no large scratch is visible in this image. Occasionally, white contrast particles are observed on the surface as shown in Fig. 2.2 and those are possibly a leftover silica from colloidal silica suspension, or it can be a residue from electropolishing.

If the surface looks good under SEM, the specimens are further cleaned with acetone to remove copper tape residue on the bottom and with methanol again prior to irradiation. Nitrogen gas blower gun was used to dry residual methanol quickly from the sample surface. Especially, if it is a high temperature irradiation, specimens need to be cleaned thoroughly to prevent any contamination during irradiation.

2.2. Irradiation Using Ion Accelerator

2.2.1. Accelerator Background

The 1.7 MV Tandem accelerator and 140 kV linear accelerator were used for ODS alloy studies. The background and principle of each accelerator will be introduced in this section to explain how they work and to shed light on why specific accelerator is used for certain experiment.

2.2.1.1. General Ionex 1.7 MV Tandem Accelerator

The 1.7 MV Tandem accelerator was manufactured by General Ionex Corporation and it is designed to have two separate ion sources. One is SNICS (Source of Negative Ions by Cesium Sputtering) and the other one is Duoplasmatron. The SNICS source uses a cylindrical shape solid cathode bar, while Duoplasmatron uses injected gas to produce ion beam. The SNICS source can produce any elements from H up to Au, except noble gases (He, Ar, Xe, Kr etc.). For ODS alloy studies, SNICS source is utilized with pure Fe cathode bar, therefore, only SNICS source will be introduced in this section.

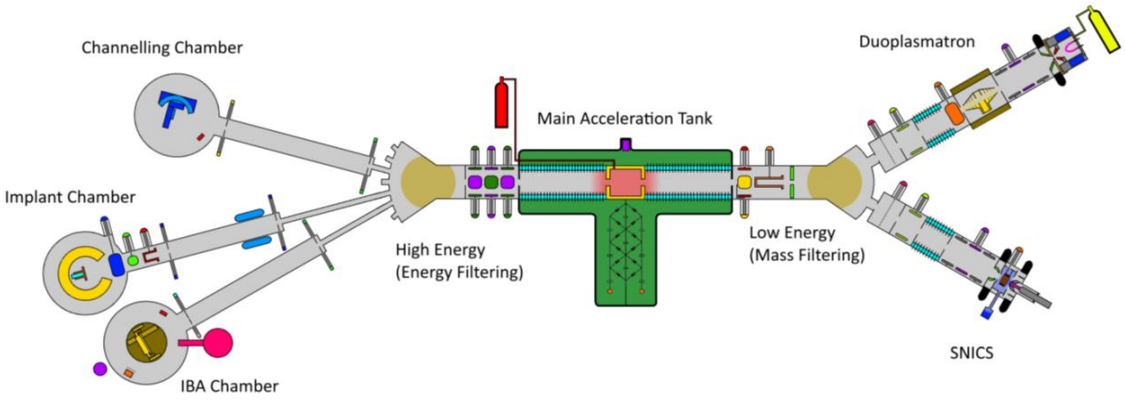

Figure 2.3 A schematic of 1.7 MV Tandem accelerator (reprinted with permission) [2].

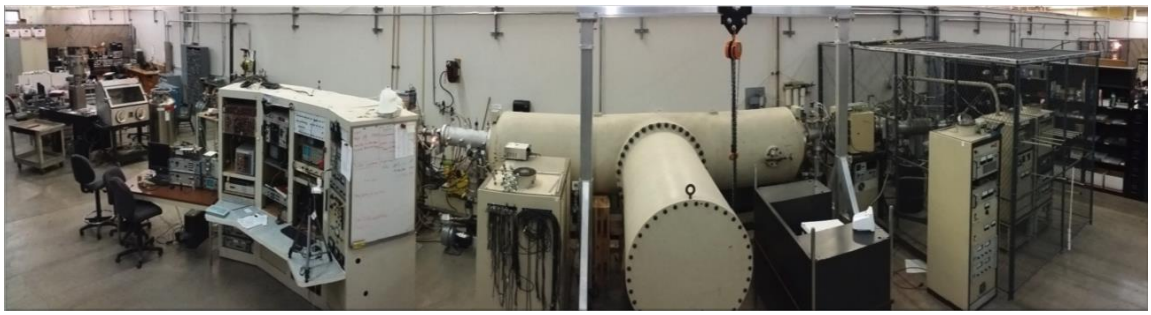

Figure 2.4 The 1.7 MV Tandem accelerator in Texas A&M Ion Beam Laboratory.

Figure 2.3 shows the entire 1.7 MV Tandem accelerator from the source to the target chambers. Right end side has SNICS and Duoplasmatron sources which produce low energy negatively charged ion beam. Then, the ion beam is fed to low energy magnet which is located between sources and main acceleration tank as shown in Figure 2.4. The low energy magnet bends ion beam by applying magnetic field which makes it possible to select certain mass and send it into main acceleration tank. The light ions like H and He need less magnetic field to bend, and heavy ions like Fe and Cu need more voltage applied to magnet to bend them. Once the negative ions enter the tank, they are accelerated toward high positive voltage terminal at the middle of the tank, and the electrons are stripped by injected nitrogen gas. Then, these negative ions become positive ions, and depending on how many electrons they lose, they are charged +, 2+ or more. Once they become positive, they will be repulsed away from the positive terminal and accelerated toward target chamber which has ground potential. Having high positive voltage terminal at the middle of the tank makes the ions accelerated twice and this is the reason why this type of accelerator is called as a Tandem. To keep the high voltage safe without discharge, the whole acceleration tank is filled with SF_6 insulating gas, and the pressure is regularly

monitored by operators before experiment. The high voltage is achieved by a Cockcroft and Walton type cascade generator, consisted of identical stages of capacitors and rectifiers. The final energy of ion beam is calculated by using Eq. 2.1,

$$\mathrm{E\ [MeV]} = V_n + (q+1) \cdot V_T \tag{2.1}$$

where V_n is the energy of injected negative ions, V_T is the terminal voltage applied, q is a charge state of ion. This equation implies that if the ions are double charged, the final energy will be higher than single charged ions. The injected negative ion energy can be calculated by adding extraction and pre-acceleration voltages, and normally those values (several kV) are relatively smaller than the terminal voltage (few MV) which do not affect that much on final energy.

After acceleration tank and focusing quadrupoles, ion beam reaches at high energy magnet as shown in Fig. 2.3, and the beam is selected by magnet and directed to desired

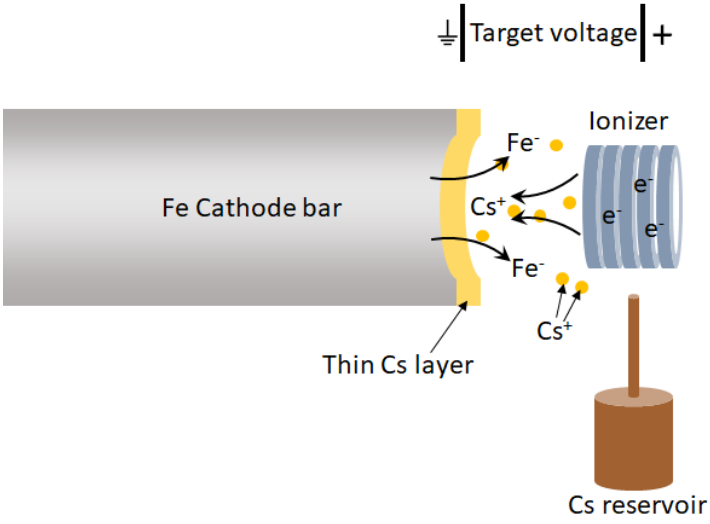

Figure 2.5 Schematic showing the principle of SNICS source**.**

beam line. By using high energy magnet, different charge state ion beams can be distinguished and even isotopes can be separated too. For ODS studies, only implantation chamber which is located at left side 11° (L11) was used for Fe implantation, and we used 3.5 MeV Fe^{2+} ions.

Figure 2.5 shows the schematic of SNICS source and how the negative ions are produced by Cs sputtering. To produce negatively charged ions from solid cathode bar, Cs reservoir needs to be heated first to 100-200 ℃, so that Cs can be evaporated and go

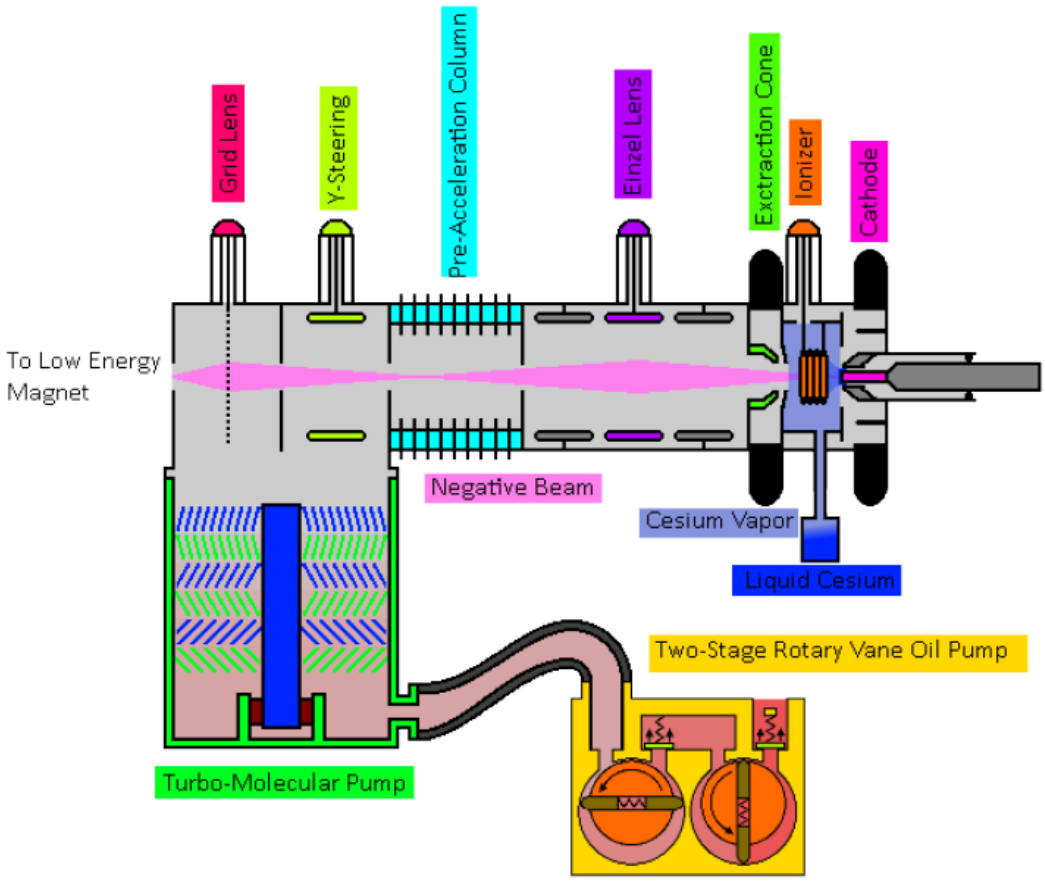

Figure 2.6 A schematic of internal structure and operation principles of the SNICS source (reprinted with permission) [2].

up through the chimney to reach at the ionizer. The ionizer is heated by high current and emits thermal electrons. Then, the Cs vapors are enclosed by cool cathode and heated ionizer, and some of Cs vapors condense on the cathode surface forming a thin layer, while others are ionized by thermal electrons turning into Cs^+. These Cs^+ ions are further accelerated by target voltage toward cathode, sputtering the material out. When Fe is sputtered, the thin Cs layer on the cathode surface gives electrons to Fe due to their weak electronegativity, and makes negatively charged Fe ions. Those ions leave the cathode surface and are accelerated toward ionizer by target voltage, and then further extracted by extraction voltage applied to extraction cone as shown in Figure 2.6.

Once ions leave extraction cone, beam is focused by einzel lens, and further accelerated by pre-acceleration column. The Y-steerer located after pre-accelerator helps beam positioning in vertical direction and grid lens focuses the beam before it is sent to low energy magnet.

From source to the target chamber, all system requires high vacuum for better beam transmission and for clean irradiation without contamination. Source part vacuums are maintained at low 10^{-7} torr range, tank is at 10^{-6} torr due to nitrogen gas feeding, beam lines are maintaining low 10^{-7} torr, and implantation target chamber is kept at 10^{-8} torr during irradiation. To maintain high vacuum system, each part uses either turbo pump with roughing pump or ion pump. We use two types of roughing pump in our system, which are rotary vane oil pump and oil-free scroll pump. For the parts where pumps run continuously without stopping like sources and beam lines, rotary vane oil pumps are used for roughing pump, since back streaming of oil is not a problem. Also, to further prevent

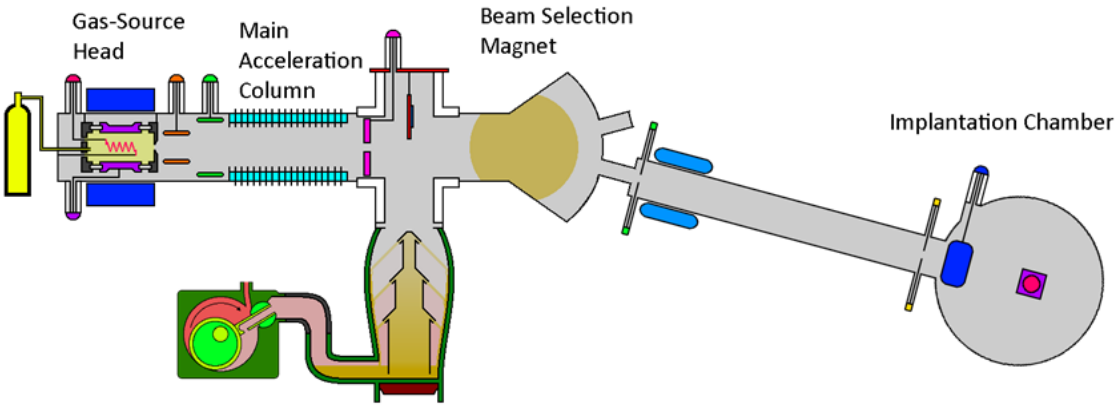

Figure 2.7 A Schematic of 140 kV accelerator from source to the implantation chamber (reprinted with permission) [2].

back streaming, filters are attached between all oil pumps and turbo pumps. However, the part we constantly start and shut off pumping system like target chamber, dry scroll pump is used with turbo pump to prevent any oil back streaming to the chamber, since oil can be a critical source of carbon.

2.2.1.2. 140 kV Accelerator

140 kV accelerator uses gas source to generate positive ions with high current. A schematic and a photo of the accelerator are shown in Figure 2.7 and 2.8, respectively. The source is in cylindrical shape with small hole at one end with tungsten filament inside. When the filament is heated, thermal electrons are generated, and they interact with injected gas forming a plasma. To continue the plasma, entire cylindrical source head is surrounded by an electromagnet. With this magnet, thermal electrons are confined and travel in a long spiral path, increasing an interaction between gas and electrons [2]. The bias between anode and filament also helps plasma confinement and shaping [2]. Once

Figure 2.8 A photo of 140 kV accelerator in Texas A&M Ion Beam Laboratory.

positively charged ion beam is extracted from source toward main acceleration column, it gains energy through acceleration column and goes to selection magnet. This accelerator has one selection magnet and one beam line. The beam line has scanning coils which can be used for raster beam and slits to confine a beam size. Implantation chamber is vacuumed by turbo and dry scroll pumps to avoid back streaming oil contamination while source and acceleration column are vacuumed by diffusion oil pump with mechanical oil roughing pump. The implantation chamber can do both room temperature and high temperature irradiation, and both defocused beam and raster beam can be used in this accelerator. Although the beam energy can be obtained from this machine is relatively low compare to other 1.7 MV and 3 MV tandem accelerators, this accelerator can produce high current beam straightforwardly. For ODS study, therefore, this accelerator was used for room temperature He implantation with 120 keV energy He^{+} and dose of 1E15 and 1E16 ions/cm^2.

2.2.2. Irradiation Process

Before mounting samples on the hot stage, beam size and position need to be known. After all beam parameter adjustments including beam defocusing and deflection, a clean paper piece is cut and attached on the stage with copper tape. When the paper piece is irradiated, it turns color to brown which tells us beam uniformity and size. Once right

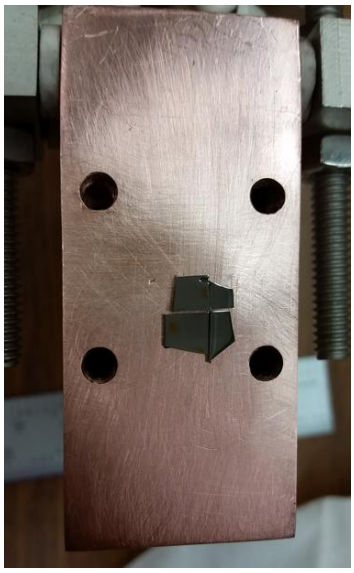

Figure 2.9 A photo of 1.7 MV accelerator hot stage with samples mounted.

beam size and uniformity are obtained, the beam area is marked by razor blade on the copper stage and paper and copper tape are removed. To prevent any contamination during irradiation, the stage is cleaned with acetone to remove any adhesives from copper tape and cleaned once again with methanol. Then, samples are mounted by using water-based carbon free silver paste, and a heat gun is used to dry silver paste for better adhesion. Figure 2.9 shows a typical photo of 1.7 MV accelerator copper hot stage with 4 samples attached with silver paste. To minimize the exposure of silver paste to beam, and to ensure

a good contact between sample and stage for heat conduction, proper amount of silver paste needs to be applied.

The total irradiation time can be calculated when fluence, charge state q, beam area and beam current on the stage are known as shown in Eq. 2.2. The beam current is monitored every hour and recorded with stage temperature to adjust the total irradiation time.

$$\text{Total time [s]} = \frac{Fluence\left[\frac{1}{cm^2}\right] \cdot 1.602 \times 10^{-19}[C] \cdot q \cdot beam\ area[cm^2]}{Beam\ current\ [A]} \quad (2.2)$$

The recent study on effect of carbon and other contaminants during accelerator irradiation revealed that utilizing beam deflectors can mitigate the problem [3-5]. Those carbon and oxygen rich molecules and nitrogen contaminants are dragged to main beam by Coulomb-drag effect and delivered to specimens. To avoid this problem, three bending magnets were located at the implant chamber beam line, and they deflect the beam to zigzag path while the contaminants with lower mass will be bent even with higher angle and filtered out during this process. Other charge-neutral molecules are trapped by liquid nitrogen cold trap located at the beam line between deflectors and also another cold trap is located at the target chamber to maintain high vacuum in the chamber during irradiation.

For all irradiations on 1.7 MV using Fe beam at high temperature, uniformly defocused beam was used instead of raster beam due to the reason that the static defocused beam gives more neutron-atypical effects than the raster beam in terms of swelling behavior [5].

2.3. Sample Characterization

2.3.1. Scanning Electron Microscopy (SEM)

The SEM is normally used to check the specimen surface quality before irradiation and also to see the surface change after irradiation. Figure 2.10 shows a photo of Vega 3 (Tescan) in MIC at Texas A&M University. The electrons are generated by Schottky type field emission gun (FEG) and accelerated by applied voltage which is normally 5-20 kV. For metal specimens, normally higher operating voltage gives better resolution while sacrificing some surface details. In the studies here, operating voltage of 10 kV was used, and it was sufficient enough to see the features on the surface and to find a specific region (10μm × 2 μm) to do FIB on. The condenser lens, objective lens, stigmator and deflection coils are used to focus and shape the beam down through the column. Depending on the

Figure 2.10 A photo of Tescan Vega3 in Texas A&M MIC.

purpose, SE and BSE imaging can be used and chemical analysis using characteristic X-ray (EDX) can be also used with special detector system inserted.

The SE imaging mode utilizes secondary electrons generated from the surface by interaction between surface material's free electrons and the main electron beam. Therefore, the specimen needs to be conductive to obtain a good quality surface image, and sometimes Pt coating can be used for nonconductive materials. BSE imaging uses backscattered electrons from sample atoms, and it gives Z-contrast image. With increasing atomic number, the number of backscattered electrons increases too, which gives higher signal to detector. The high Z-number elements, therefore, look brighter in BSE image than the low Z-number elements..

2.3.2. Focused Ion Beam (FIB) Preparation

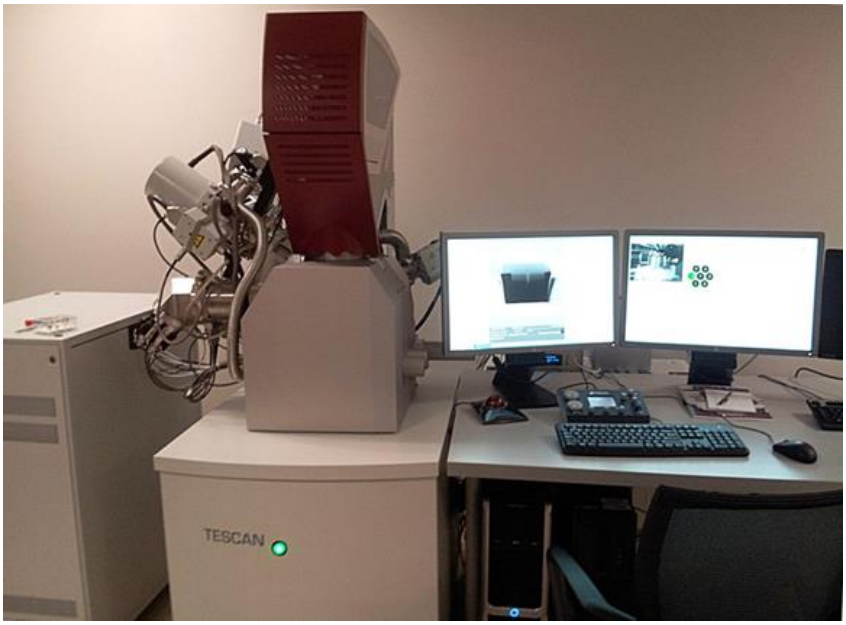

Figure 2.11 A photo of Tescan Lyra 3 FIB-SEM machine in Texas A&M MCF.

Figure 2.11 shows a photo of Lyra 3 (Tescan) in MCF at Texas A&M University. This FIB-SEM machine enables to cut out small volume from unirradiated and irradiated samples, and move it to TEM grid, so that it can be inserted in the TEM machine for further analyses. Figure 2.12 shows general e-beam, Ga ion beam and gas injection system (GIS) configurations. As e-beam and Ga ion beam columns are located at 55 degree angle, stage and specimen need to be tilted to 55 degree for this specific FIB-SEM machine. Due to large atom size of Ga, sample is etched out with high sputtering rate, and normally 30 kV energy Ga beam is used with different aperture and current settings. The sputtering rate differs by each material, and softer material like Si normally has higher sputtering rate than harder material such as Fe based alloys. The working distance of sample for both e-beam and i-beam is 9 mm, and this distance need to be kept at all FIB processes to avoid any damage when inserting manipulator or GIS. The GIS has five different nozzles and Pt is commonly used to protect the material surface from Ga beam while making a TEM lamella. A typical TEM lamella lift-out process is shown in Figure 2.13. The 10 μm × 2 μm area with 2-3 μm thickness of Pt layer is deposited on the surface of region of interest as shown in Fig. 2.13(a). Current settings between 70 pA – 200 pA are used for Pt deposition. Then, surface around Pt layer is etched out using stair rectangular and polishing rectangular options, and when the sample thickness reaches to 1.5-2 μm, J-cut is used to further cut out the bottom and side connections, except small portion on the top left side to hold the sample while welding the manipulator to lamella. 10 nA current is used for initial rough etching, and 1 nA and 3 nA current settings are used for polishing and cutting afterwards before the sample is moved to TEM grid. When it is ready to be

lift-out, manipulator is inserted and attached to the sample by using Pt as shown in Fig. 2.13(b). The inset figure in Fig. 2.13(c) is a typical TEM copper grid with 4 posts which is frequently used for TEM lamellas. The 10 µm × 10 µm size with thickness of 1.5 µm

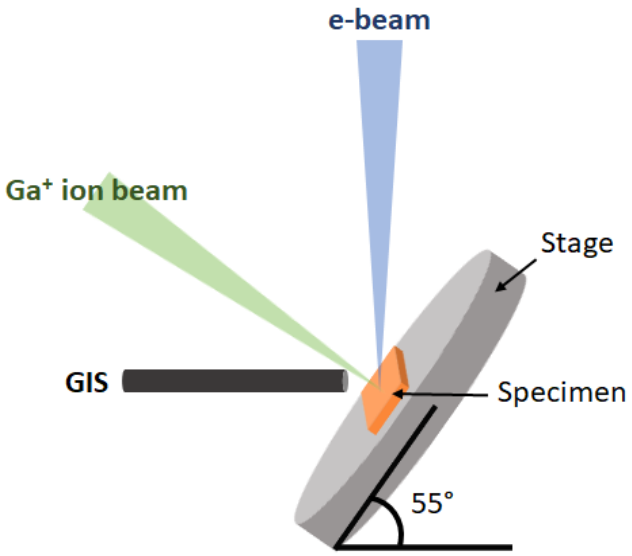

Figure 2.12 A configuration of e-beam, ion beam and GIS in Tescan Lyra 3 FIB-SEM machine.

cross-sectioned specimen is welded on one of the posts like Fig. 2.13(c) using Pt deposition. Once it has a firm connection, a 3 nA beam current beam is used to break the connection between manipulator and lamella. As TEM specimen needs to be thinned enough so that 200 kV energy electron beam can transmit, specimen is further thinned by lowering Ga beam currents from 1 nA down to 70 pA until the specimen thickness becomes less than 200 nm. While this process, sample is tilted to ± 2º with different polishing directions. Then, final cleaning process utilizes 5 kV low energy Ga beam to

remove all FIB-induced damage and to reduce the thickness down to less than 100 nm. Once it reaches to desired thickness, the specimen looks bright under SEM as shown in Fig. 2.13(d). During the thinning process, in-beam BSE view needs to be always turned on and Pt layer needs to be carefully watched, so that sample beneath the Pt layer is not etched away. Also, to make a firm connection with grid post, polishing rectangular boxes are gradually moved away from the connection, so that it has a gradual thickness decrease rather than dramatic thickness change while thinning.

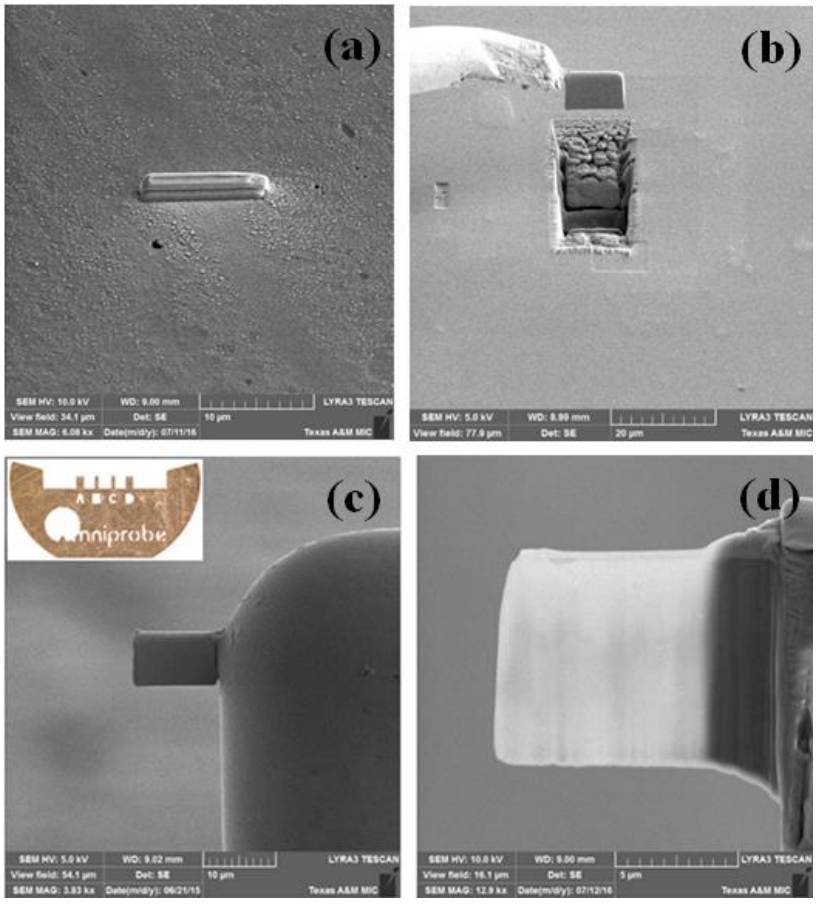

Figure 2.13 SEM images of TEM lamella lift-out process.

2.3.3. Transmission Electron Microscopy (TEM) Analysis

TEM is a very useful tool for analyzing sample microstructures, especially for void swelling analysis, oxide dispersion stability study, and chemical analysis using EDX. In this study, both FEI Tecnai G2 F20 ST FE-TEM and F20 FE-TEM were used for analysis by using various technique like bright field, dark field, STEM, EELS, and EDX etc. Most of the characterizations were conducted using F20 ST FE-TEM and only EELS thickness

Figure 2.14 A photo of FEI Tecnai G2 F20 ST FE-TEM in MIC at Texas A&M.

measurement was conducted on F20 FE-TEM which is shown in Figure 2.14. They are almost identical with the same operating voltage of 200 kV, but F20 FE-TEM is more

frequently used for Cryo-TEM, EFTEM and EELS and has lower resolution than the other one, while F20 ST FE-TEM is especially used for HRTEM and EDX analysis.

Figure 2.15 shows schematic of TEM components and principles of bright field, dark field, and diffraction modes. Electrons are generated by ZrO2/W (100) Schottky FEG and accelerated toward specimen. Condenser lens magnet focuses the beam and condenser aperture determines the total amount of beam arrives at the specimen. Once the beam passes through the specimen, objective lens magnet focuses the beam and objective

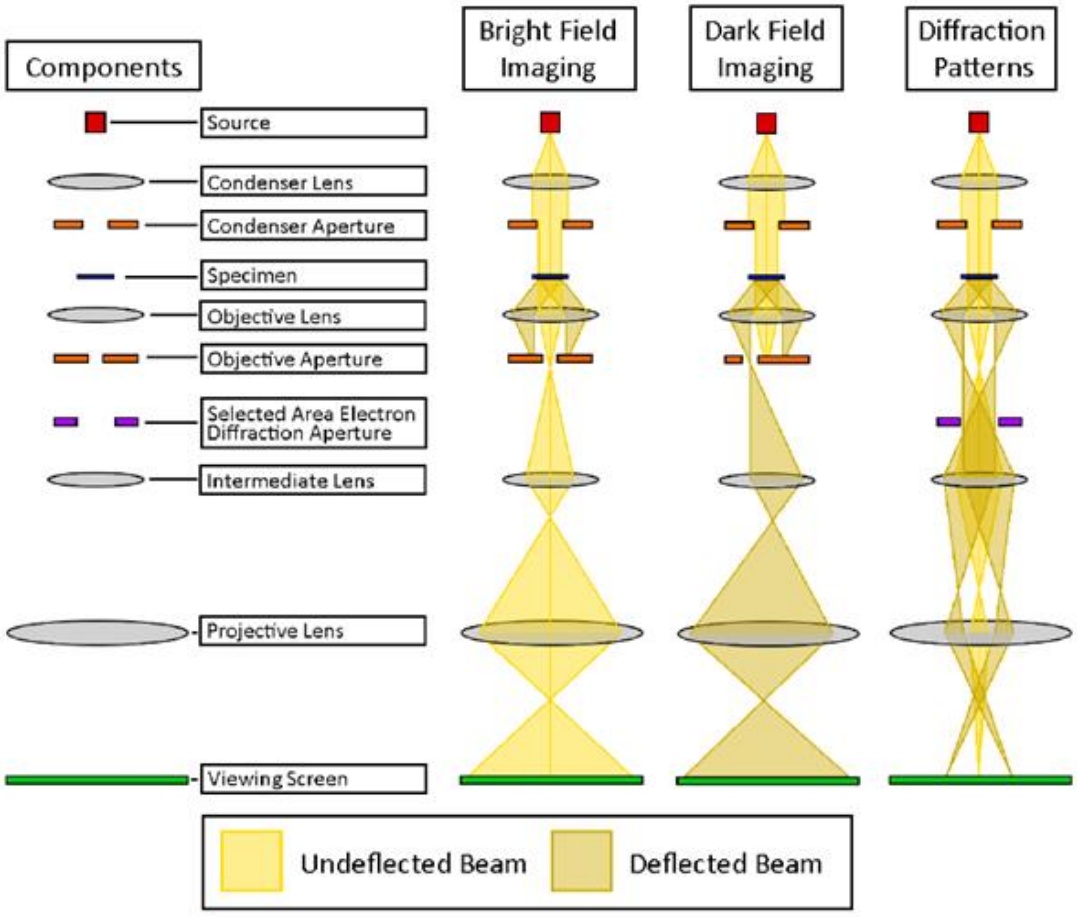

Figure 2.15 Schematics of TEM components and principles of each imaging mode [2].

aperture under the lens helps selecting one or more beams that contribute to the final image. It is also used to give a higher contrast to bright field imaging. The smaller the aperture, the higher contrast can be obtained. The selected area aperture defines a region where diffraction pattern is obtained, and the intermediate lens coil magnifies the image coming from objective lens. Finally, the projector lens coil further magnifies the image

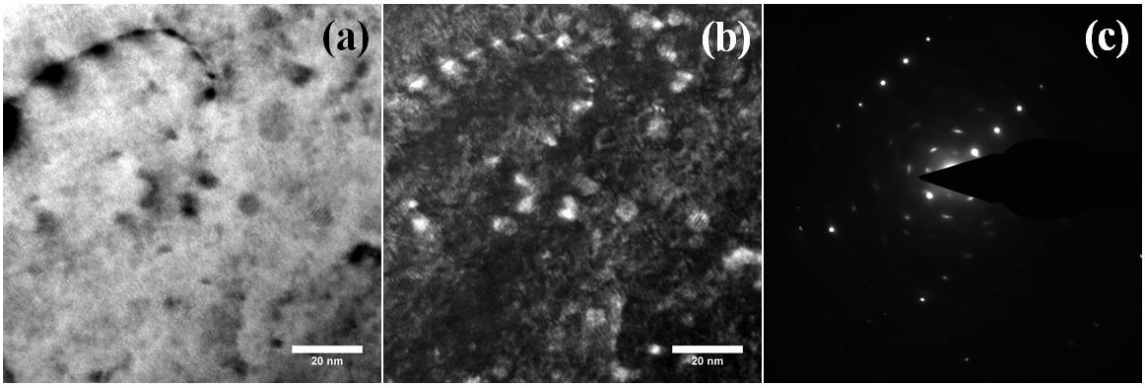

Figure 2.16 Typical (a) bright field, (b) dark field, and (c) diffraction pattern taken from this region of 12Cr ODS alloy.

from intermediate lens coil and projects it on a phosphorescent screen.

Depending on the aperture positions, different imaging modes can be selected as shown in Fig. 2.15 and Figure 2.16. For example, bright field with good contrast can be obtained by using small size objective aperture (10) which only allows main beam to penetrate. If certain diffraction pattern is chosen by objective aperture for imaging, dark field image can be obtained like Fig. 2.16(b), which is very useful for dispersoid coherency study, dislocation loop and dislocation imaging etc. In dark field image, electrons only diffracted toward the direction of selected diffraction beam appear bright, while all other

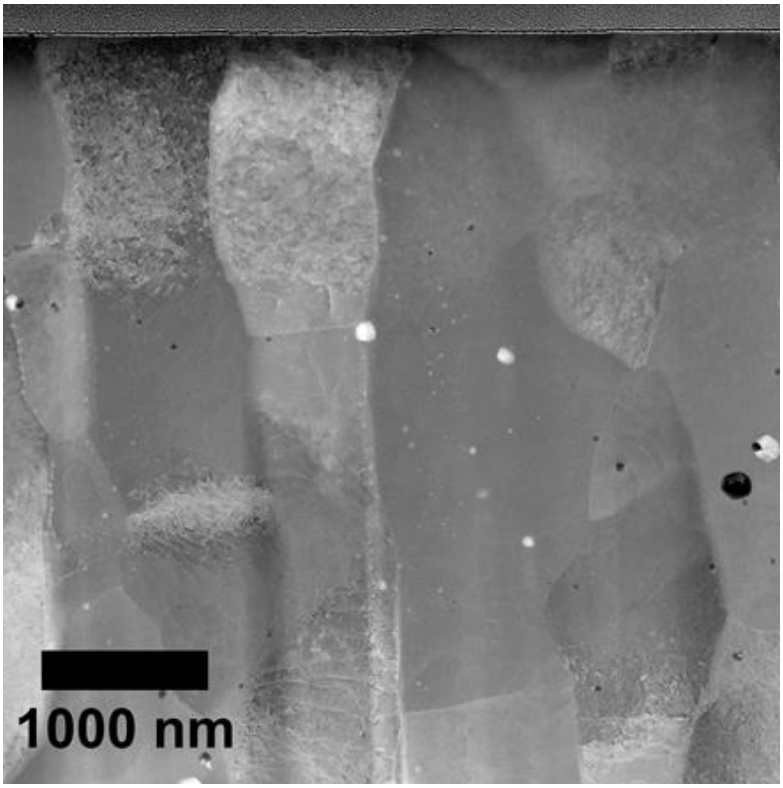

Figure 2.17 A typical STEM image taken form Hf-doped ODS alloy.

features remain dark. In this way, coherency of oxide dispersoids in the matrix can be distinguished.

Figure 2.17 shows a typical STEM image taken from Hf-doped ODS alloy. This particular imaging technique uses a focused fine spot size beam to scan over the specimen to obtain an image. It is suitable to see a grain morphologies and Z-contrast by using high-angle-annular-dark-field (HAADF) detector, and EDX analysis is also can be used under this mode. As shown in Fig. 2.17, the particles which have different atomic number clearly

show different contrast, and higher Z material appears brighter due to higher scattering intensity.

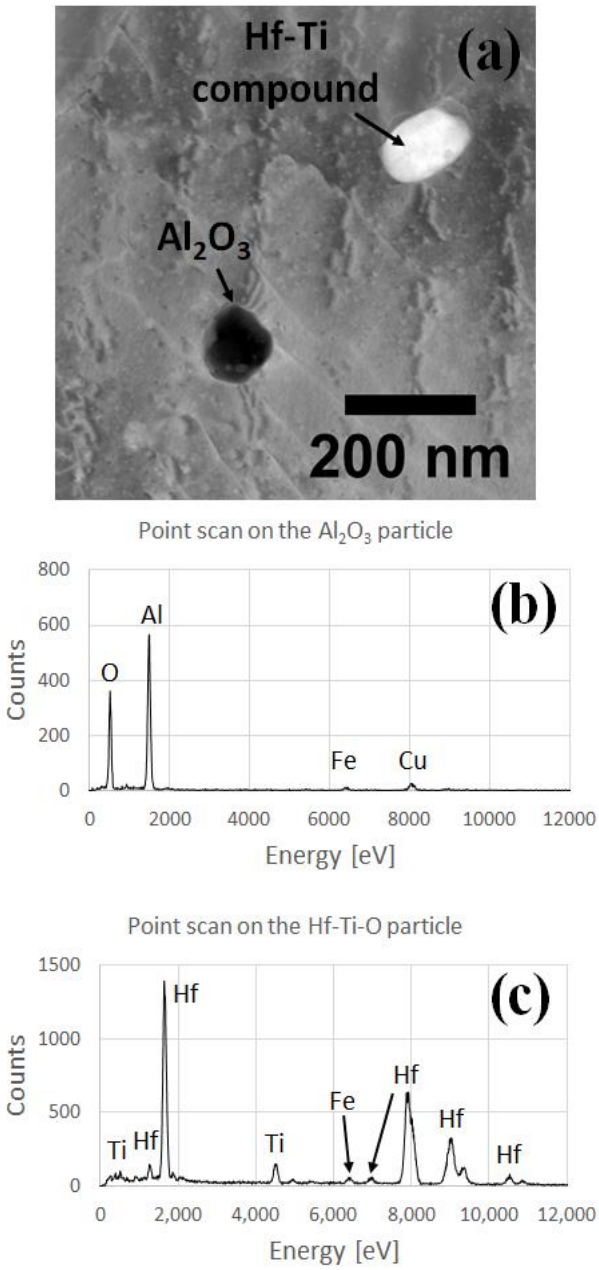

Figure 2.18 (a) STEM image of two different contrast particles, and EDX point scan spectroscopies from (b) dark contrast particle and (c) bright contrast particle.

The EDX spectroscopy is a type of microscopy uses finely focused electron beam to generate characteristic X-ray for chemical analysis. Each element has distinguishable characteristic X-ray energy and EDX spectroscopy can be obtained from certain region of STEM image by using AZtec or INCA software. In Figure 2.18, a STEM image shows two different contrast particles, and bottom two point scan spectroscopies are from those particles. The dark contrast particle is confirmed as Al and O rich particle, possibly an Al_2O_3, while bright contrast particle shows high Hf and Ti concentration, which can be a Hf-Ti-O. Other EDX functions like 1D line scan and 2D mapping are also a very useful tool to analyze chemical compositions of compounds and matrix. The EFTEM is also good for enhancing image contrast, element mapping and quantifying in the image. It utilizes energy loss spectrum properties to increase image contrast. In this study, however, EFTEM is not used and therefore will not be introduced here. Instead, another powerful chemical analysis equipment, which is APT, will be introduced in section 2.3.4.

Another TEM analysis used in this study is EELS. When known energy of electrons lose their energy while interacting with specimen by inelastic scattering, those energy losses can be measured by electron spectrometer and the peaks can be distinguished from each other. The energy losses are commonly caused by plasmon excitation, inner shell ionization, Cherenkov radiation, inter and intra band transitions, and phonon excitation. The spectrum peaks from inner shell ionization can be used for elemental mapping, because each element requires unique energy for ionization. It is very useful to analyze low atomic number materials and has better resolution than EDX. Figure 2.19 shows a typical EELS. Among many features we can do with EELS, only sample

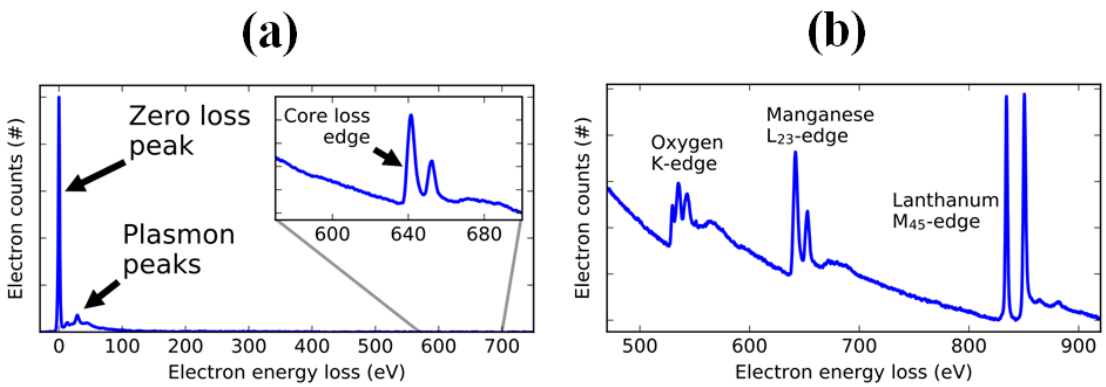

Figure 2.19 A typical EELS show (a) zero-loss peak and plasmon peaks and enlarged core-loss edge peaks and (b) inner shell ionization edge from $La_{0.7}Sr_{0.3}MnO_3$ [7].

thickness measurement using zero-loss peak is used in this study. The sample thickness can be easily calculated by using electron mean free path λ, total beam intensity I_t and zero-loss intensity I_o as shown below in Eq. 2.3.

$$\text{Thickness} = -\lambda \cdot \ln\left(\frac{I_o}{I_t}\right) \tag{2.3}$$

When using log-ratio method, log-rate absolute method was used in this study and this method is only valid for high refractive index materials like metal and semiconductors. During the process, effective atomic number needs to be inputted and inelastic mean free path is computed. The zero-loss counts are isolated for computing relative thickness t, and then, the relative thickness value is converted to absolute thickness by using computed inelastic mean free path value. It is a quick and reliable thickness measurement tool and all TEM specimens examined in this study used EELS to get a thickness data.

The final important TEM technique used in this paper is high-resolution TEM (HRTEM). The HRTEM is very useful when checking coherency of particle with matrix and measuring lattice parameter of unknown precipitates. Along with Fast Fourier Transform (FFT), HRTEM helps examining crystal structure of unknown material. To obtain a good HRTEM image, good beam alignment is essential. Once alignment is done at high magnification, specimen is tilted until it is at certain zone axis under diffraction

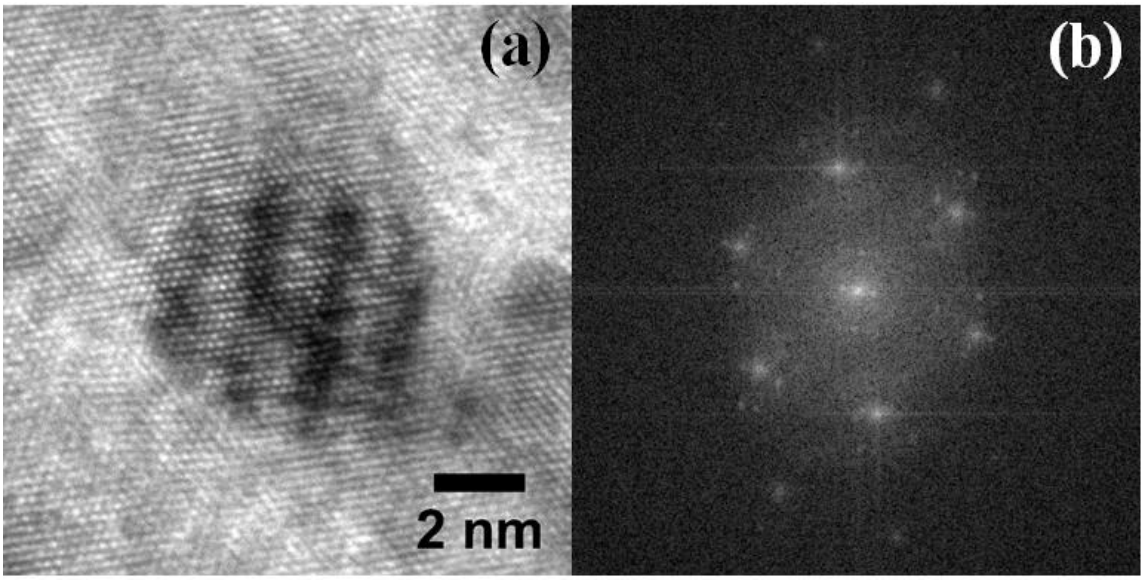

Figure 2.20 (a) HRTEM image of oxide dispersoid in Hf-doped ODS alloy and (b) its FFT image.

mode. By using proper size of objective lens aligned with beam axis, HRTEM image can be obtained like shown in Figure 2.20(a). The Fig. 2.20(b) is a FFT image of HRTEM which shows frequencies of lattice parameter. From this image, both matrix and oxide dispersoid lattice parameters can be obtained from each dot and we can also see which zone axis this HRTEM is taken from.

2.4. References

[1] T. Muroga, T. Nagasaka, Y. Li, H. Abe, S. Ukai, A. Kimura, T. Okuda, Fabrication and characterization of reference 9Cr and 12Cr-ODS low activation ferritic/martensitic steels, Fusion Eng. Design 89 (2014) 1717-1722.

[2] L. M. Price, A study of the crystallization and amorphization mechanisms of metallic glasses under ion bombardment, PhD diss., Texas A&M University, College Station, 2016.

[3] J. G. Gigax, H. Kim, E. Aydogan, F. A. Garner, S. Maloy, L. Shao, Beam-contamination-induced compositional alteration and its neutron-atypical consequences in ion simulation of neutron-induced void swelling, Mater. Res. Lett 5 (7) (2018) 478-495.

[4] L. Shao, J. G. Gigax, D. Chen, H. Kim, F. A. Garner, J. Wang, M. B. Toloczko, Standardization of accelerator irradiation procedures for simulation of neutron induced damage in reactor structural materials, Nucl. Instrum. Meth. Phys. Res. B 409 (2017) 251-254.

[5] J. G. Gigax, H. Kim, E. Aydogan, L. M. Price, X. Wang, S. A. Maloy, F. A. Garner, L. Shao, Impact of composition modification induced by ion beam Coulomb-drag effects on the nanoindentation hardness of HT9, Nucl. Instrum. Meth. Phys. Res. B 444 (2019) 68-73.

[6] J. G. Gigax, E. Aydogan, T. Chen, D. Chen, Y. Wu, W. Y. Lo, Y. Yang, F. A. Garner, The influence of beam rastering on the swelling of self-ion irradiated pure iron at 450°C, J. Nucl. Mater. 465 (2015) 343-348.

[7] Wikipedia contributors. (2019, January 24). Electron energy loss spectroscopy. In Wikipedia, The Free Encyclopedia. Retrieved 04:10, February 21, 2019, from https://en.wikipedia.org/w/index.php?title=Electron_energy_loss_spectroscopy&oldid=879945000

3. OXIDE DISPERSOID COHERENCY STUDY ON 12CR ODS ALLOY

3.1. Introduction

The oxide dispersion strengthened (ODS) alloys have been considered for advanced nuclear fusion and fission reactor component materials [1-3] due to its superior stability under irradiation [4] and high temperature strength [5]. Among many ODS alloys, dual-phase ferritic-martensitic (FM) 12Cr ODS alloy was selected for this study due to its good radiation tolerance with improved corrosion and oxidation resistance compared to 9Cr ODS alloys [6,7,10]. It is known that oxide dispersoids help stabilize grain boundaries and act as sinks for both point defects. Also, dispersoids hinder dislocation glide so that dislocation can work as recombination site for point defects in the matrix [19,20]. Therefore, stability of oxide dispersoids is very important that determines the ODS alloy material property under irradiation. One of the important components that affects dispersoid stability is coherency. It is known that coherent dispersoids are more stable than incoherent dispersoids under irradiation [7]. Chen et al. showed that large incoherent oxide dispersoids were observed in unirradiated tempered martensite (TM) phase and they disappeared after ~60 local dpa irradiation while small coherent dispersoids were stable in the same 12Cr ODS alloy [7]. However, the previous coherency study on this 12Cr ODS alloy was limited to only TM phase, and the systematic study on relationship between coherency, size and density of dispersoids in different phases has not been conducted yet. In this study, therefore, the dispersoid coherency in each ferrite and TM

phase as a function of irradiation depth was characterized along with dispersoid size and density analyses.

The interfaces of solid-solid phases can be divided into three different types; coherent, semi-coherent, and incoherent. The dispersoid coherency with the matrix is related to the interfacial energy as shown in Eq. 3.1 [21,22,28],

$$\text{Free energy} = \text{Interfacial energy } [4\pi r^2 \gamma_i] + \text{Elastic energy } \left[\frac{4}{3}\pi r^3 \cdot \varepsilon^2 c\right] \quad (3.1)$$

where r is radius of oxide dispersoid, γ_i is interfacial energy, ε is relative strain from lattice misfit, and c is the elastic constant. When the oxide dispersoid is small, the interfacial term contributes more on total free energy, and the volumetric elastic energy term dominates when dispersoid size is large. The coherent dispersoid has lower interfacial energy (γ_i<200mJ/m^2) while incoherent dispersoid has larger value (γ_i>800 mJ/m^2) [21,28], and therefore, small dispersoids prone to take a coherent relationship with matrix to lower down the total free energy by having lower γ_i value [6,26-28]. The critical radii of semi-coherent dispersoid were introduced by Ribis et al. [25] calculated from this equation using interfacial energy (200-800 mJ/m^2) and elastic constant introduced in Ref. [23,24] for $Y_2Ti_2O_7$ and Y_2O_3.

Previous studies confirmed that this 12Cr ODS alloy contains pyrochlore $Y_2Ti_2O_7$ type dispersoids [6], and Ohnuma et al. showed that this type of oxide nanoparticles has the finest size and highest number density [29]. The pyrochlore structure has cube-on-cube orientation with bcc Fe matrix, and {110} plane of Fe matrix matches with {440}$Y_2Ti_2O_7$ plane [25]. Therefore, small dispersoids will favorably take a coherent

relationship with matrix {110}. Therefore, in this study, g_{110} reflection is utilized for dark field imaging to differentiate coherency of dispersoid at each depth and in each phase.

3.2. Experimental Procedure

The 12Cr ODS dual-phase alloy was fabricated by Shigeharu Ukai of Hokkaido University, Japan by MA process. The chemical composition of this alloy is shown in Table 3.1. The Y_2O_3 powder is added to the rest of the element powder and mechanically alloyed in argon gas atmosphere and consolidated at 1100 ℃ for 2 hours. After hot-extrusion at 1150 ℃ and normalization at 1050 ℃ for an hour, it is tempered at 800 ℃ for an hour. The Ti and excess O contents were well controlled in this alloy to produce small size high density oxide dispersoids to maximize creep resistivity [10,29]. Other fabrication details can be found in the paper published by Ukai et al. [10]. The alloy was cut into 3 mm×6 mm×2 mm specimen, and mechanically polished down to a 0.7 mm thickness by using SiC paper (down to p4000 grit). A 0.04 μm silica suspension and polishing cloth were used for final polishing step to remove cold-work surface region.

Table 3.1 Composition of as-received 12Cr ODS alloy (wt. %).

Fe	Cr	C	Ni	W	Ti	N	Ar	Y_2O_3	Excess O
Bal.	11.52	0.16	0.34	1.44	0.28	0.007	0.006	0.33	0.10

The specimen was then irradiated using a 1.7 MV Ionex tandem ion accelerator at Texas A&M University. Beam energy of 3.5 MeV Fe^{2+} ions were used to a fluence of 9.54×10^{16} ions/cm^2 (100 peak dpa). The fluence is calculated by Stopping and Range of

Ions in Matter (SRIM) using Kinchin-Pease option with Fe displacement threshold energy of 40 eV [11,12]. The irradiation temperature was chosen to 475 ℃ which is close to the maximum swelling temperature for ferritic alloys, and it was kept within ±5 ℃ during irradiation [13-16]. The beam was defocused over by 6 mm x 6 mm area. The target chamber vacuum was kept at 4-6 × 10^{-8} torr by using liquid nitrogen cold traps during irradiation, and three beam deflectors with liquid nitrogen cold trap were located on the beam line to avoid carbon contamination [17,18,30].

After irradiation, focused ion beam (FIB) lift-out technique was used to make a transmission electron microscopy (TEM) specimen. The FIB specimen was cut and thinned by 30 keV Ga^+ ion beam to reach ~10 μm × ~10 μm × ~200 nm size first. Then, Ga^+ beam energy was dropped to 5 keV for fine thinning to reach a thickness less than 100 nm and to remove any FIB induced damage on the surface. The TEM characterization was conducted using 200 kV electron beam, and bright field (BF), weak beam dark field (WBDF), and electron energy loss spectroscopy (EELS) techniques were used. TEM and FIB equipment used in this study are FEI Tecnai G2 F20 Super-Twin, FEI Tecnai F20, and Tescan Lyra-3 located at Texas A&M University Microscopy Imaging Center and Material Characterization Facility.

3.3. Results

3.3.1. Grain Stability

Figure 3.1(a) shows grain morphology of 12Cr ODS alloy after 100 peak dpa irradiation, and the irradiated area is enclosed by two dashed lines. The top black dashed line refers to sample surface, and the bottom white dashed line indicates end of ion range

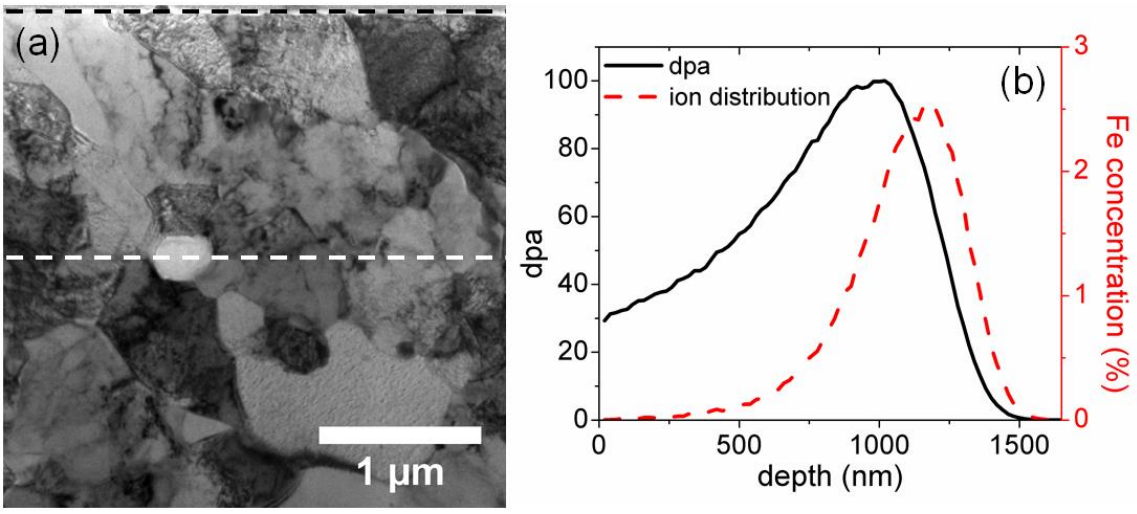

Figure 3.1 (a) TEM BF micrograph of 100 peak dpa irradiated 12Cr ODS alloy. Superimposed black dashed line in (a) indicates irradiation surface and white dashed line refers to end of ion range (~ 1.6 μm depth from surface). (b) SRIM calculation of dpa (black solid line) and Fe ion implant (red dash line) as a function of depth.

for 3.5 MeV Fe beam. Grain size for irradiated region is 412 ± 79 nm, and grain size for irradiation free thermally annealed region is 557 ± 130 nm. Considering error bars, grain size is stable after 100 peak dpa irradiation, which agrees with previous grain stability study on this alloy that showed stable grain morphologies even after 800 peak dpa irradiation [6]. Figure 3.1(b) shows the Fe ion distribution and dpa curve indicated by red dashed line and black solid line respectively as a function of depth calculated by SRIM.

3.3.2. Dispersoid Stability

Figures 3.2 shows TEM micrographs of ferrite grains taken from different depths. Figures 3.2(a1-e1) show the bright field micrographs at depth of 200 nm, 500 nm, 800 nm, 1000 nm, and 2000 nm respectively. Corresponding dark field images were taken by using WBDF technique with g_{110} direction excited at (g, 3g) tilting condition, and diffraction

patterns are superimposed on each DF image. The scale bar in Fig. 3.2(a1) applies to other micrographs too. The oxide dispersoids have dark contrast in BF image, and the

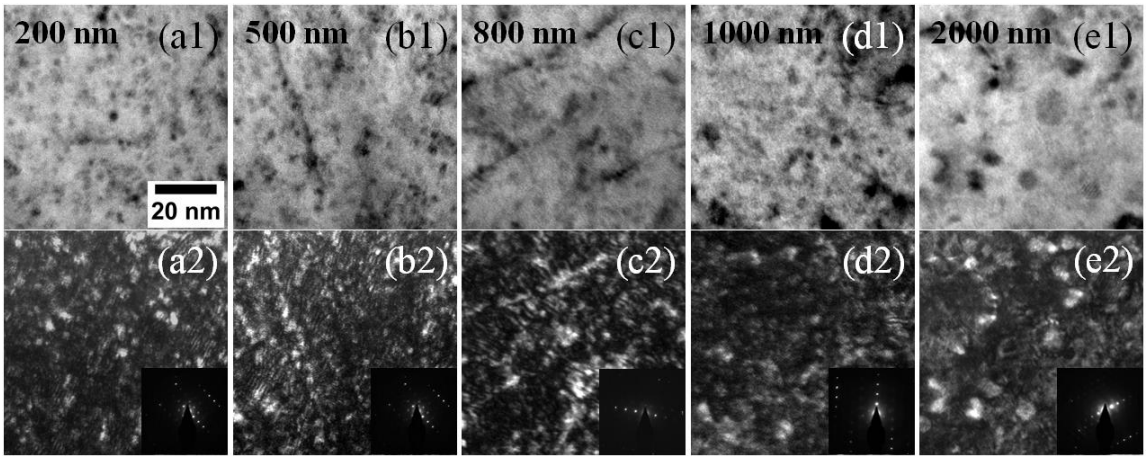

Figure 3.2 (a1-e1) TEM BF micrographs and (a2-e2) WBDF micrographs of ferrite phase at depth of 200 nm, 500 nm, 800 nm, 1000 nm, and 2000 nm, respectively, with TEM diffraction patterns superimposed on each DF image.

dispersoids coherent to (110) of matrix will appear bright in DF image, while incoherent dispersoids will not show up or show lattice misfit in DF image. The same technique is applied to get BF and DF images from martensite phases as shown in Figures 3.3. Images were taken from the same depths with ferrite grain to compare dispersoid size and density against ferrite phase. Diffraction patterns are superimposed on each DF image. The 2000 nm depth represents thermally annealed region without any radiation damage. This region can be used as a reference because previous study revealed that the dispersoid size after 1000 nm depth region is close to the dispersoid size of unirradiated as-received sample [6], which means that oxide dispersoid size and density are not affected by thermal annealing at 475 ℃.

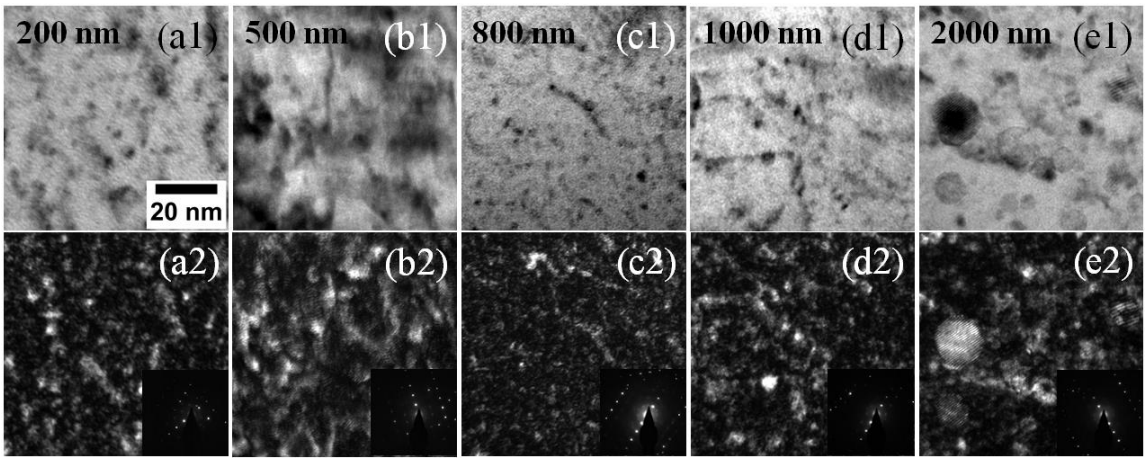

Figure 3.4 (a1-e1) TEM BF micrographs and (a2-e2) WBDF micrographs of TM phase at depth of 200 nm, 500 nm, 800 nm, 1000 nm, and 2000 nm, respectively, with TEM diffraction patterns superimposed on each DF image.

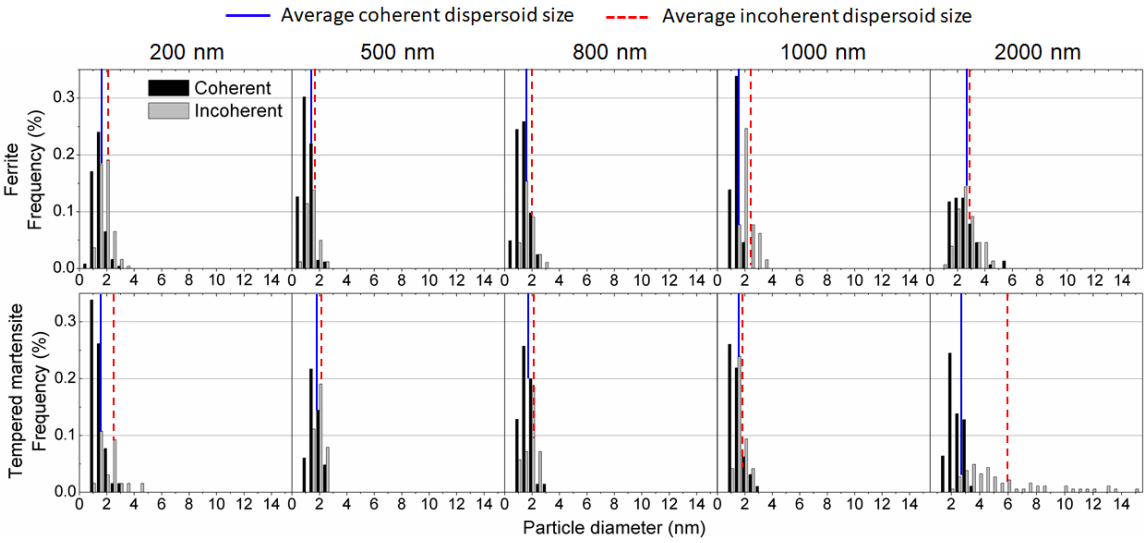

Figure 3.3 Oxide dispersoid size distributions in ferrite and TM phases at different depths. Black bars refer to coherent dispersoids and gray bars refer to incoherent dispersoids. Superimposed blue solid line and red dashed line are average coherent and incoherent dispersoid sizes, respectively.

Figures 3.4 show the coherent and incoherent dispersoid size distributions in ferrite and TM phases at different depths. The top five histograms show ferrite phase and the

bottom five histograms are from TM phase. Black and gray bars in histogram refer to coherent and incoherent dispersoids, respectively. The average coherent and incoherent dispersoid sizes are indicated by blue solid lines and red dashed lines, respectively. In ferrite grain, the coherent and incoherent dispersoid size shows similar distribution at 2000 nm region (out of ion range). Under irradiation, both coherent and incoherent average dispersoid sizes reduce, and the density of coherent dispersoid increases compare to 2000 nm region. Also, incoherent dispersoid size is slightly larger than coherent one within the irradiated region.

In TM phase, the coherent and incoherent size distributions are very different at 2000 nm depth, and incoherent dispersoids take larger size and wider distribution compare to coherent dispersoids due to the reason explained in the introduction section (3.1). However, within the ion range (≤1000 nm), those large incoherent dispersoids disappear, and both coherent and incoherent dispersoid size distribution and density become similar.

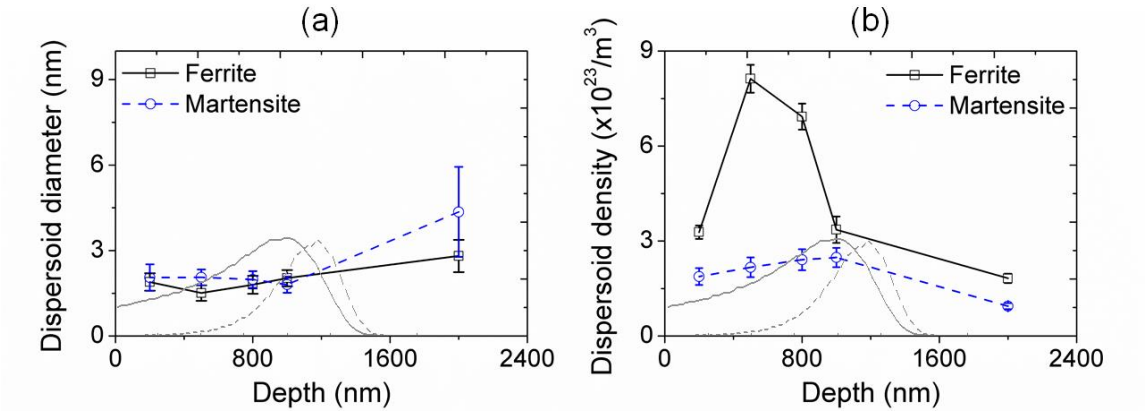

Figure 3.5 Depth distributions of (a) mean dispersoid diameter and (b) total dispersoid density in ferrite and TM grains. Superimposed gray solid lines refer to Fe dpa curve and dashed lines indicate Fe ion distribution calculated by SRIM.

Note that the coherent dispersoid size distribution in TM phase does not show a big difference under irradiation compare to out of ion range region. At all depths, the average incoherent dispersoid sizes are larger than those of coherent dispersoids.

Figure 3.5(a) shows the average dispersoid diameter in ferrite and TM phases as a function of depth. The dpa curves and Fe ion distributions calculated by SRIM are superimposed on each figure. The average dispersoid diameters shrink to similar size (1.5 ~ 2 nm) for both ferrite and TM phases in irradiated region (≤ 1000nm), and TM phase

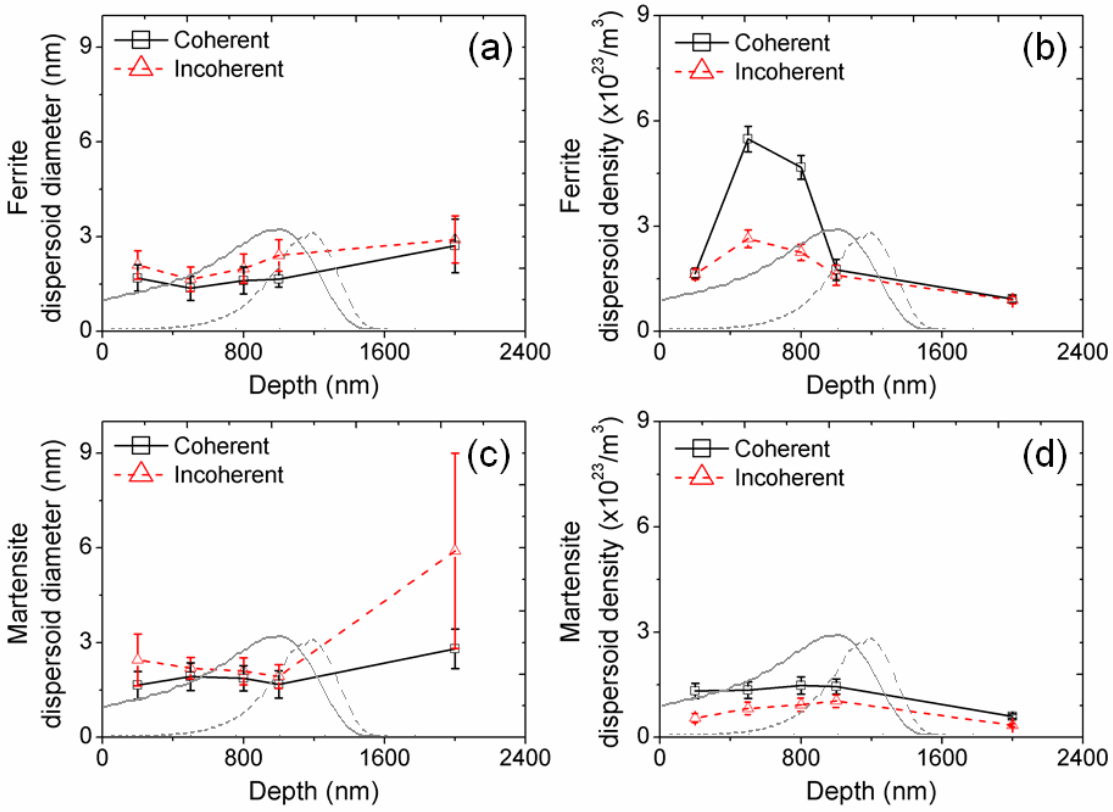

Figure 3.6 Depth distributions of coherent and incoherent (a) dispersoid diameter, and (b) dispersoid density in ferrite grains, and (c) dispersoid diameter, and (d) dispersoid density in TM grains. Gray solid and dashed lines superimposed on each graph refer to Fe ion distribution profile, respectively.

shows more dramatic change than ferrite phase under irradiation. As shown in figure 3.5(b), ferrite phase shows huge increase in dispersoid density under irradiation showing at most 4.5 times of increment especially at 500 – 800 nm depth, while TM phase shows only 1.8 times of increment.

The size and density data are further subdivided into coherent and incoherent dispersoids as shown in figures 3.6. Fig. 3.6(a) shows dispersoid size change as a function of depth in ferrite phase. There is a slight dispersoid size reduction under irradiation for both coherent and incoherent dispersoids, and incoherent dispersoids are slightly larger than coherent dispersoids within the ion range. Fig. 3.6(b) further shows that the dramatic density increment in ferrite grain is mostly caused by coherent dispersoid density jump rather than incoherent dispersoid. As shown in Fig. 3.6(c), in martensite grain, coherent dispersoid size slightly decreases under irradiation, while large incoherent dispersoids disappear under irradiation and become similar size to coherent dispersoids. Note that the large error bar at 2000 nm is due to wide size distribution of incoherent dispersoids varying from 2 nm to 16 nm diameter. In Fig. 3.6(d), coherent and incoherent dispersoid densities in martensite phase show minor increment within 1000 nm depth, and density of coherent dispersoids is higher than incoherent dispersoids at all depths.

The volume fraction of dispersoid per unit volume is shown in Table 3.2. Volume fraction of oxide dispersoids in ferrite grain is almost consistent considering error bar, while large volume fraction change is observed in martensite grain under irradiation. This means that dissolved large oxide dispersoids are not reprecipitated to a new oxide dispersoid under irradiation and they rather stay as a solute in the matrix.

Table 3.2 Volume fraction of oxide dispersoids per unit volume.

Depth (nm)		200	500	800	1000	2000
Volume fraction (%)	Ferrite	0.12±0.06	0.14±0.08	0.20±0.10	0.16±0.08	0.21±0.13
	Tempered martensite	0.07±0.05	0.10±0.04	0.10±0.04	0.07±0.04	0.58±0.77

3.4. Discussion

It is known that the coherent dispersoids are more favored to be nucleated than incoherent dispersoids under certain condition due to their lower interfacial energy [31]. The experimental result of ferrite phase also showed that the dispersoid density increment is mostly contributed by coherent dispersoid density increase rather than incoherent dispersoid. This increment of coherent dispersoid density under irradiation is good for material property because small size with high density dispersoids are good for hindering dislocation movement and strengthening the material [28,32,33], and also coherent dispersoids are better at grain boundary pinning [34,35] compare to the incoherent dispersoids. Incoherent dispersoids also give dispersion strengthening effect by giving a resistance when dislocation tries to overcome incoherent dispersoids [36]. Although large incoherent dispersoids in TM phase are susceptible to irradiation, the small size incoherent dispersoids still exist under irradiation, and the density remains almost the same or even shows slight increment as shown in Fig. 3.6(d), which will still give dislocation pinning effect. Even though coherent dispersoids are more favorable for nucleation as dislocation and matrix lattices already match each other, semi-coherent and incoherent dispersoids

can still be nucleated and they will be preferentially nucleated at dislocations for lower free energy [36]. The good stability of both coherent and incoherent small dispersoids under irradiation helps material to sustain its properties under irradiation at high temperature. On top of that, nucleation of new oxide dispersoids under irradiation in both ferrite and TM phases even promotes material strength by giving more resistance on dislocation glide and by providing more surface sink for defect recombination, and this is why ODS alloy shows good creep resistance and swelling resistance.

The ferrite and the TM phase showed different dispersoid density behaviors under irradiation as shown in Fig. 3.6(b and d). The ferrite phase showed more dramatic density increment especially from coherent dispersoids compared to the TM phase. Both ferrite and TM phases are bcc structures, but they have some intrinsic differences. First, for this 12Cr ODS dual-phase alloy, TM grain size is much smaller (~200 nm) with higher dislocation density, while ferrite grains are larger (~ 1 μm) [6]. It is also known that martensite phase has more carbon than ferrite phase resulted from rapid phase transformation process. Due to these intrinsic differences, ferrite and TM phase have shown very different void swelling behavior in previous study [6]. The TM phase swells much less than ferrite phase, showing less than 0.06 % swelling, while ferrite exhibits about 1.6 % swelling after 800 peak dpa irradiation [6]. Also, a depth where the void swelling occurred in ferrite phase (500-800 nm) in previous study matches with the depth where coherent dispersoid density is increased (500-800 nm) in ferrite phase of this study. Consequently, a hypothesis can be set up that the nucleation of new coherent oxide dispersoid is related to the voids generated from irradiation. This is fair postulation since

it is known that coherent particles with large elastic strain are favorably nucleated on vacancies [36], and those with no or small elastic strain can be nucleated at any place since oxygen has higher affinity with vacancy [37]. Fu et al. [37] showed that O in interstitial position has high affinity for vacancies due to weak bonding with host element Fe from Density Functional Theory (DFT) calculation. Once they form O-vacancy cluster, high O affinity solutes like Ti and Y will be attracted to O-vacancy cluster and once it reaches the critical concentration for nucleation, they will form new oxide dispersoids [37]. Therefore, there is a high possibility that the higher swelling behavior in ferrite phase may affect nucleation of oxide dispersoids under irradiation. However, to verify this hypothesis, a follow-up study with proper experiment design is needed.

3.5. References

[1] L. K. Mansur, A. F. Rowcliffe, R. K. Nanstad, S. J. Zinkle, W. R. Corwin, R. E. Stoller, Materials needs for fusion, Generation IV fission reactors and spallation neutron sources - similarities and differences, J. Nucl. Mater. 329-333 (2004) 166–172.

[2] S. Ukai, T. Nishida, H. Okada, T. Okuda, M. Fujiwara, K. Asabe, Development of oxide dispersion strengthened ferritic steels for FBR core application, J. Nucl. Sci. Technol., 34 (1997), p. 256-263.

[3] D. K. Mukhopadhayay, F. H. Froes, D. S. Gelles, Development of oxide dispersion strengthened ferritic steels for fusion, J. Nucl. Mater., 258–263 (1998), p. 1209-1215.

[4] J. Ohta, T. Ohmura, K. Kako, M. Tokiwai, T. Suzuki, Hardness of 12Cr-8Mo ferritic steels irradiated by Ni ions, J. Nucl. Mater., 225 (1995), p. 187-191.

[5] T. Okuda, S. Nomura, M. Nakanishi, M. Fujiwara, H. Takahashi, in: Proceedings of the First Japan International SAMPE Symposium, 28 November–1 December 1989, p. 1616.

[6] T. Chen, E. Aydogan, J. G. Gigax, D. Chen, J. Wang, X. Wang, S. Ukai, F. A. Garner, L. Shao, Microstructural changes and void swelling of a 12Cr ODS ferritic-martensitic alloy after high-dpa self-ion irradiation, J. Nucl. Mater. 467 (2015) 42–49.

[7] T. Chen, J. G. Gigax, L. Price, D. Chen, S. Ukai, E. Aydogan, S. A. Maloy, F. A. Garner, L. Shao, Temperature dependent dispersoid stability in ion-irradiated ferritic-martensitic dual-phase oxide-dispersion-strengthened alloy: Coherent interfaces vs. incoherent interfaces, Acta Mater. 116 (2016) 29-42.

[8] G. R. Odette, M. J. Alinger, B. D. Wirth, Recent developments in irradiation- resistant steels, Annu. Rev. Mat. Res. 38 (2008) 471-503.

[9] J. Chen, P. Jung, T. Rebac, F. Duval, T. Sauvage, Y. de Carlan, M. F. Barthe, Helium effects on creep properties of Fe-14CrWTi ODS steel at 650 C, J. Nucl. Mater. 453 (2014) 253-258.

[10] S. Ukai, Y. Kudo, X. Wu, N. Oono, S. Hayashi, S. Ohtsuka, T. Kaito, Residual ferrite formation in 12CrODS steels, J. Nucl. Mater. 455 (2014) 700-703.

[11] J. F. Ziegler, M. D. Ziegler, J. P. Biersack, SRIM – the stopping and range of ions in matter, Nucl. Instr. Meth. Phys. Res. B 268 (2010).

[12] R. E. Stoller, M. B. Toloczko, G. S. Was, A. G. Certain, S. Dwaraknath, F. A. Garner, On the use of SRIM for computing radiation damage exposure, Nucl. Instr. Meth. Phys. Res. B 310 (2013) 75-80.

[13] F. A. Garner, M. B. Toloczko, B. H. Sencer, Comparison of swelling and irradiation creep behavior of fcc-austenitic and bcc-ferritic/martensitic alloys at high neutron exposure, J. Nucl. Mater. 276 (2000) 123-142.

[14] F. A. Smidt Jr., P. R. Malmberg, J. A. Sprague, J. E. Westmoreland, Swelling behavior of commercial ferritic alloys, EM-12 and HT-9, as assessed by heavy ion bombardment, vol. STP 611, ASTM International, Philadelphia, PA, 1976, pp. 227-241.

[15] J. G. Gigax, H. Kim, T. Chen, F. A. Garner, L. Shao, Radiation instability of equal channel angular extruded T91 at ultra-high damage levels, Acta Mater. 132 (2017) 395-404.

[16] J. G. Gigax, T. Chen, H. Kim, J. Wang, L. M. Price, E. Aydogan, S. A. Maloy, D. K. Schreiber, M. B. Toloczko, F. A. Garner, L. Shao, Radiation response of alloy T91 at damage levels up to 1000 peak dpa, J. Nucl. Mater. 482 (2016) 257-265.

[17] J. G. Gigax, H. Kim, E. Aydogan, F. A. Garner, S. A. Maloy, L. Shao, Beam-contamination-induced compositional alteration and its neutron-atypical consequences in ion simulation of neutron-induced void swelling, Mater. Res. Lett.5 (7) (2018) 478-495.

[18] L. Shao, J. G. Gigax, D. Chen, H. Kim, F. A. Garner, J. Wang, M. B. Toloczko, Standardization of accelerator irradiation procedures for simulation of neutron induced

damage in reactor structural materials, Nucl. Instr. Meth. Phys. Res. B 409 (2017) 251-254.

[19] S. Ohtsuka, S. Ukai, M. Fujiwara, T. Kaito, T. Narita, Nano-structure control in ODS martensitic steels by means of selecting titanium and oxygen contents, Mater. Trans. 46 (3) (2005) 487-492.

[20] S. Ukai, M. Fujiwara, Perspective of ODS alloys application in nuclear environments, J. Nucl. Mater. 307-311 (2002) 749-757.

[21] J. M. Howe, Interfaces in materials, atomic structure, thermodynamics and kinetics of solid-vapor, solid-liquid and solid-solid interfaces, John Wiley & Sons, New York (1997).

[22] A. Maheshwari, A. J. Andrell, Morphological evolution of coherent misfitting precipitates in anisotropic elastic media, Phys. Rev. Lett. 70 (1993) 2305-2308.

[23] J. M. Pruneda, E. Artacho, First-principles study of structural, elastic, and bonding properties of pyrochlores, Phys. Rev. B 72 (2005) 085107.

[24] J. W. Palko, W. M. Kriven, S. V. Sinogeikin, J. D. Bass, A. Sayir, Elastic constants of yttria (Y_2O_3) monocrystals to high temperatures, J. Appl. Phys. 89 (2001) 7791-7796.

[25] J. Ribis, Y. de Carlan, Interfacial strained structure and orientation relationships of the nanosized oxide particles deduced from elasticity-driven morphology in oxide dispersion strengthened materials, Acta Mater. 60 (2012) 238-252.

[26] Y. Miao, K. Mo, B. Cui, W. Y. Chen, M. K. Miller, K. A. Powers, V. McCreary, D. Gross, J. Almer, I. M Robertson, J. F. Stubbins, The interfacial orientation relationship of oxide nanoparticles in a hafnium-containing oxide dispersion-strengthened-austenitic stainless steel, Mater. Charact. 101 (2015) 136-143.

[27] P. Dou, A. Kimura, T. Okuda, M. Inoue, S. Ukai, S. Ohnuki, T. Fujisawa, F. Abe, Effects of extrusion temperature on nano-mesoscopic structure and mechanical properties of an Al-alloyed high -Cr ODS ferritic steel, J. Nucl. Mater. 417 (2011) 166-170.

[28] D. A. Porter, K. E. Easterling, M. Y. Sherif, Phase transformations in metals and alloys, 3rd ed., CRC Press, (2006).

[29] M. Ohnuma, J. Suzuki, S. Ohtsuka, S. W. Kim, T. Kaito, M. Inoue, H. Kitazawa, A new method for the quantitative analysis of the scale and composition of nanosized oxide in 9Cr-ODS steel, Acta Mater. 57 (2009) 5571-5581.

[30] J. G. Gigax, H. Kim, E. Aydogan, L. M. Price, X. Wang, S. A. Maloy, F. A. Garner, L. Shao, Impact of composition modification induced by ion beam Coulomb-drag effects

on the nanoindentation hardness of HT9, Nucl. Inst. Meth. Phys. Res. B 444 (2019) 68-73.

[31] R. E. Smallman, A. H. W. Ngan, Physical metallurgy and advanced materials, 7th ed. Elsevier (2007).

[32] V. C. Nardone, J. K. Tien, Pinning of dislocations on the departure side of strengthening dispersoids, Scripta Metal. 17 (1983) 467-470.

[33] V. C. Nardone, D. E. Matejczyk, J. K. Tien, The threshold stress and departure side pinning of dislocations by dispersoids, Acta Mater. 32 (1984) 1509-1517.

[34] E. Nes, N. Ryum, O. Hunderi, On the Zener drag, Acta Metal. 33 (1985) 11-22.

[35] M. Mujahid, J. W. Martin, The effect of oxide particle coherency on Zener pinning in ODS superalloys, J. Mater. Sci. Lett. 13 (1994) 153-155.

[36] O. S. Erik, Critical materials: Underlying causes and sustainable mitigation strategies, Vol. 5, World Scientific Publishing Company Pte Limited (2019).

[37] C. L. Fu, M. Krcmar, G. S. Painter, X. Q. Chen, Vacancy mechanism of high oxygen solubility and nucleation of stable oxygen-enriched clusters in Fe, Phys. Rev. Lett. 99 (2007) 225502.

4. HE PREIMPLNATATION STUDY ON 12CR ODS ALLOY

4.1. Introduction

The previous dispersoid coherency study in chapter 3 on 12Cr ODS alloy revealed a different response of coherent dispersoid density in ferrite and tempered martensite (TM) phases under irradiation. The ferrite phase showed much higher coherent dispersoid density increment compare to the TM phase. One hypothesis made is that the difference in nucleation of coherent dispersoid may be related to the difference in void swelling behavior between ferrite and TM phases, as previous studies on this alloy showed that ferrite phase swells much more than TM phase [16,17]. Therefore, to see the effect of void, He pre-implantation method is used since He and vacancy forms He-vacancy clusters in the bcc Fe matrix [9-13], and also by using He bubbles, (n,α) transmutation reaction in real reactor environment can be emulated which causes He embrittlement in the material [18-22]. The previous He pre-implantation studies on ODS alloys showed how oxide dispersoid suppress the He bubble coarsening after He ion implantation, but this study only focused on the He bubble size and density change rather than focusing on oxide dispersoid stability and also high dpa Fe irradiation was not conducted after He implantation [23]. Chen et al. [24] showed defect evolution under electron irradiation after He pre-implantation and they reported that He bubbles help suppression of loop and cavity growth. Lu et al. [19] used heavy-ion irradiation after He pre-implantation on 9Cr ODS alloy and reported reduced oxide dispersoid size and increased density with increasing dose (dpa). However, the systematic study on oxide dispersoid size and density change in

terms of coherency before and after He pre-implantation was not conducted yet, and the mechanism of density increment along with He presence is not explained well in the previous studies.

Therefore, in this chapter, the experiment is designed and conducted to see the effect of pre-existing He bubbles in the matrix on nucleation of coherent dispersoids under irradiation by varying He doses. For consistency with the previous coherency study, the same 12Cr ODS alloy is used for this study which showed high swelling resistant behavior in previous studies [16,17].

4.2. Experiment Procedure

The dual-phase 12Cr ODS alloy was fabricated by Shigeharu Ukai from Hokkaido University, Japan by using MA process. The detail fabrication process and chemical composition of this alloy is elucidated in chapter 3. Three identical 12Cr ODS alloy samples were prepared and cut into 3 mm × 6 mm × 1.5 mm dimension. Then, samples were mechanically polished by using SiC paper up to p-4000 grit, and further polished down with 0.25 μm diamond suspension and 0.04 μm silica suspension to remove cold worked region. The final sample thicknesses were ~0.7 mm.

The experiment design of this study is shown in Figure 4.1. Two samples were irradiated by using 140 kV linear accelerator with 120 keV energy He^{+} raster beam with dose of 1×10^{15} and 1×10^{16} ions/cm^2 at room temperature. The 1E15 He sample was characterized using FIB and TEM to see an effect of He implantation on oxide dispersoid size and density. Then, the same sample was irradiated by using 1.7 MV tandem accelerator with 3.5 MeV Fe^{2+} defocused beam to reach 100 peak dpa at 475 ℃ together

with 1E16 sample and other polished 12Cr ODS sample without He preimplantation. The average dpa rate was 1.74×10^{-3} dpa/s for Fe ion beam. Note that three beam deflectors were used on 1.7 MV accelerator beam line to filter out charged carbon and other contaminants during irradiation, and vacuum was kept at $4.0\text{-}6.0 \times 10^{-8}$ torr range by using liquid nitrogen cold trap on a target chamber [1-3]. Also, liquid nitrogen cold trap was located at beam line close to the chamber to eliminate neutral charge contaminants from the beam [1-3].

After Fe ion irradiation, all three samples were characterized after FIB preparation and the TEM results were compared against each other to see the He preimplantation effect on nucleation of coherent dispersoids. To simulate 3.5 MeV Fe dpa curve and 120 keV He ion distributions in the material, the SRIM-2013 Kinchin-Pease option with Fe displacement threshold energy of 40 eV was used [4,5] as shown in figure 4.2.

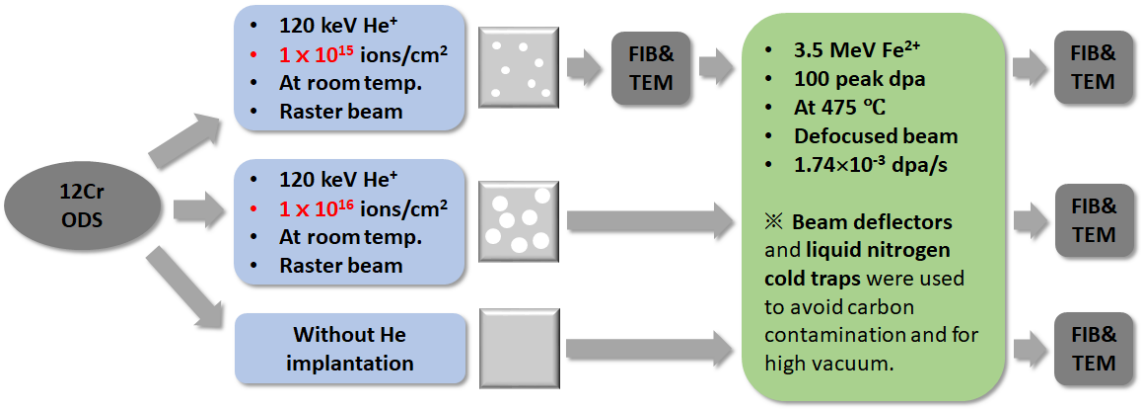

Figure 4.1 The experiment overview of this study.

Fig. 4.2 shows SRIM calculation of 120 keV He ion profiles for both 1E15 and 1E16 doses and 3.5 MeV Fe 100 peak dpa curve as a function of depth in pure Fe. The 3.5 MeV Fe beam can penetrate 1.5 μm deep from the surface while showing the maximum damage at 1 μm depth region. In case of 120 keV He, the penetration depth is about 0.5 μm from the surface. The blue patterned area of 120 keV He curve refers 1E15 He, while blue dotted curve indicates 1E16 He. The 1E16 He dose reaches over 6000 appm in the matrix. The 120 keV energy is selected for He implantation to avoid both free surface sinking effect and defect imbalance effect from injected interstitial of Fe beam [6]. The 300-400 nm depth region where He ion concentration peaks is the region of interest of this study. Note that the averaged Fe local dpa for this region is about 43 dpa.

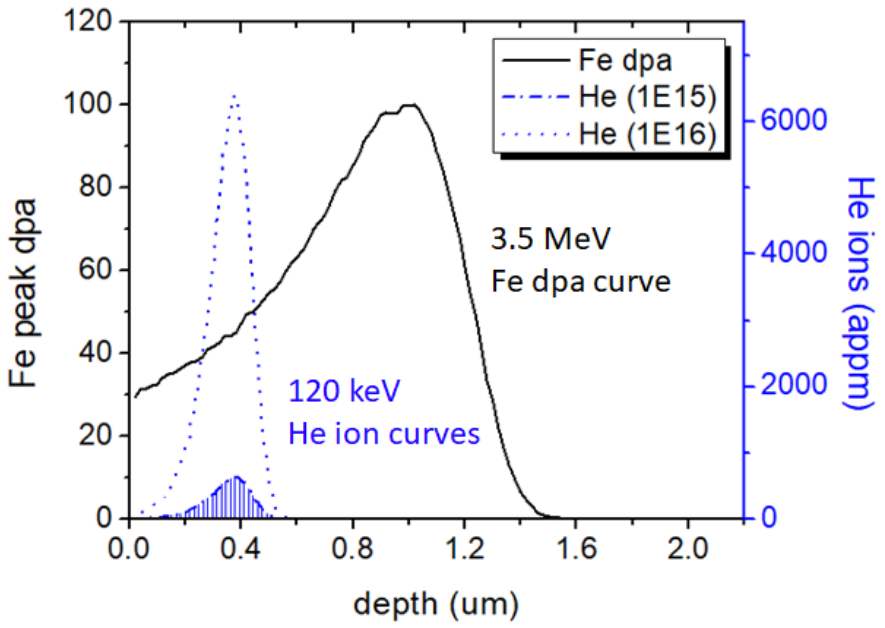

Figure 4.2 SRIM calculation of He ion (blue dashed line) and Fe damage (black solid line) profiles as a function of depth.

4.3. Results

4.3.1. After He implantation

The TEM images were taken from 350 nm depth region where the He ion peak is located to see the effect of He implantation on oxide dispersoid size and density. Figures 4.3(a) and (b) show bright field and dark field images of He implanted sample taken by using (g, 3g) condition with g_{110} direction excited as indicated in inset diffraction image in 4.3(b). The oxide dispersoids have dark contrast in bright field image regardless of coherency, while only coherent dispersoids look bright in dark field image. By comparing both images, coherent and incoherent dispersoids can be counted separately. Note that

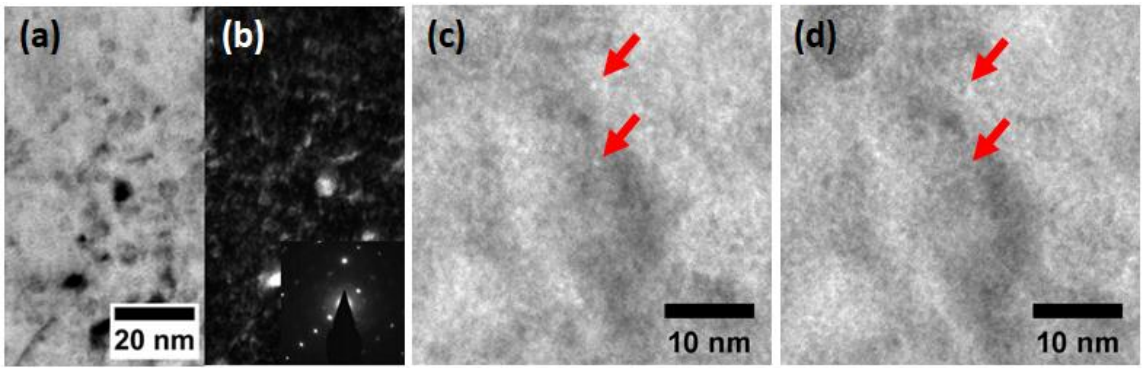

Figure 4.3 TEM (a) bright field and (b) dark field image, (c) under focused image and (d) over focused image taken from 350 nm depth region.

only TM phase was analyzed in this study due to two reasons. First, the TM phase takes 80 % of the volume of the alloy. Second, the ferrite phase already showed dramatic density change even without He implantation in previous study which will make it harder to judge the He implantation effect itself. Therefore, to see the impact of He preimplantation

clearer, only TM phase was characterized in this study. Also, only coherent dispersoids were counted because newly nucleated oxide dispersoids are prone to take a coherent relationship with matrix for lower surface (free) energy.

Figures 4.3(c) and (d) are TEM bright field under and over focused image respectively taken from 350 nm depth region. In under focused image, He bubbles look white, while they look dark in over focused image. The He bubble size was measured to be less than 1 nm diameter at this depth. The size and density data of oxide dispersoids will be shown and compared in chapter 4.3.4.

4.3.2. After Fe irradiation

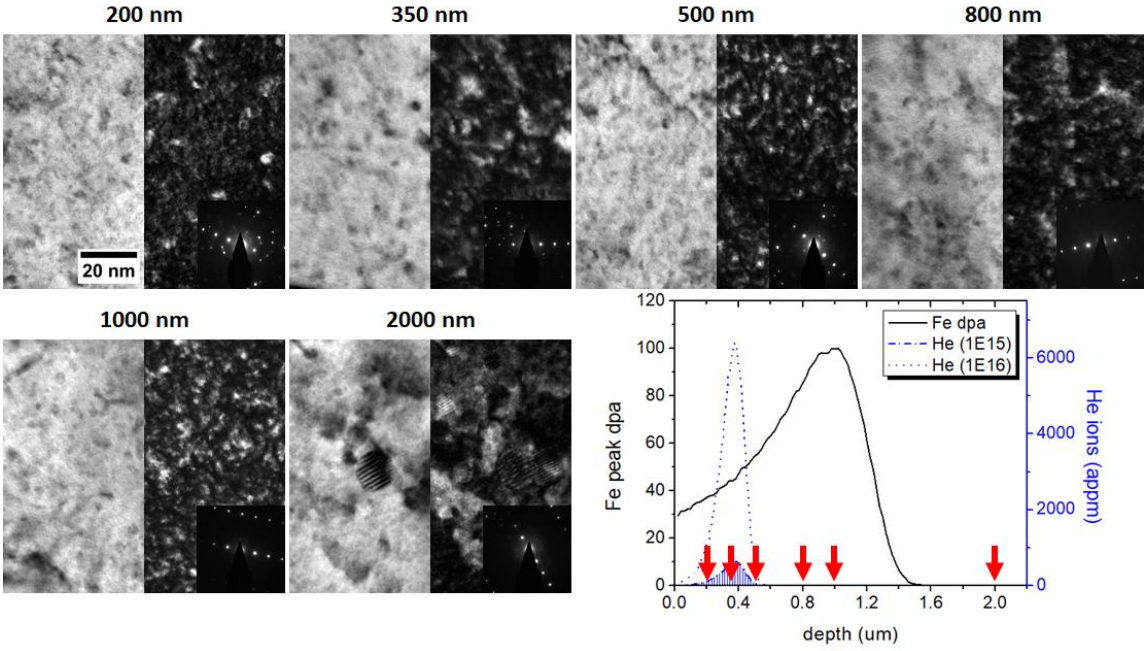

Figure 4.4 TEM bright field and dark field images of Fe irradiated sample taken from 200, 350, 500, 800, 1000, and 2000 nm depth with diffraction patterns superimposed in dark field images. SRIM Fe dpa and He ion profiles are shown with red arrows overlaid where each depth was characterized.

Figures 4.4 show bright field and dark field images taken from Fe irradiated sample at each depth. Images were taken from six different depths including out of ion range region (2000 nm) which will be a reference point, just annealed without irradiation. The same WBDF condition is used with previous Fig. 4.3 for consistency, and each diffraction pattern was inset into DF images. The red arrows superimposed on the SRIM profiles indicate the depth characterized for this sample. As shown in Figs. 4.4, large incoherent dispersoids are observed at 2000 nm depth, but only small size, mostly coherent dispersoids are observed within the ion range (≤1000 nm).

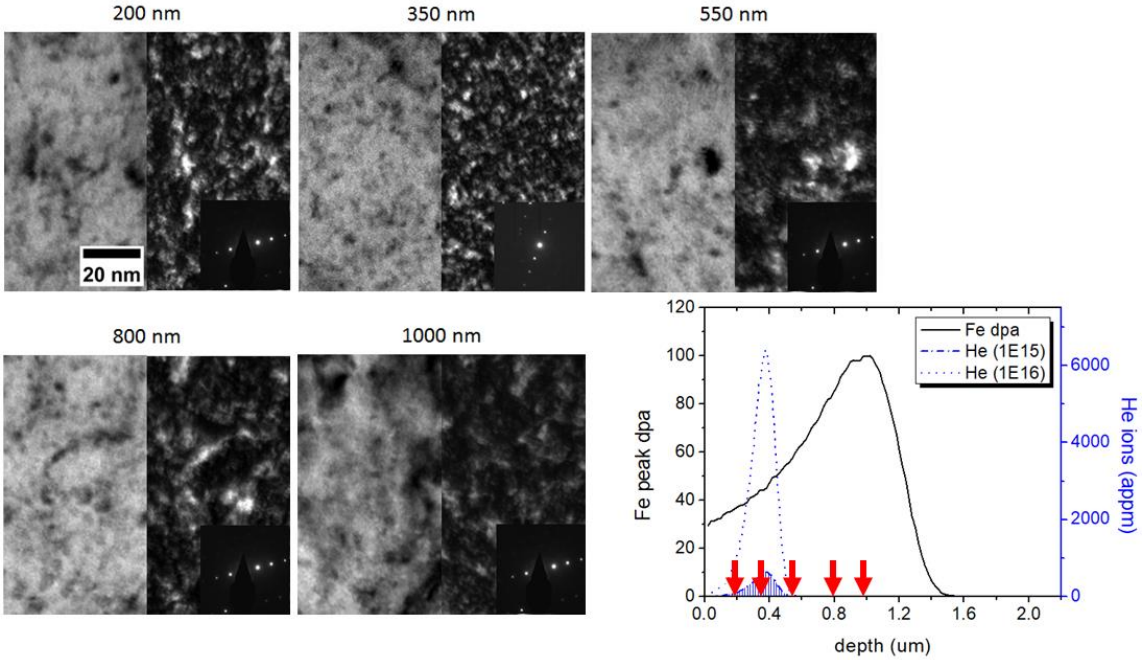

Figure 4.5 TEM bright field and dark field images of 1E15 He preimplanted Fe irradiated sample taken from 200, 350, 550, 800, and 1000 nm depth with diffraction patterns superimposed on each dark field image. SRIM Fe dpa and He ion profiles are shown with red arrow representing the depth where the TEM images are taken.

4.3.3. After He preimplantation and Fe irradiation

Figures 4.5 show TEM BF and DF sets of 1E15 He preimplantated and Fe irradiated sample. The same WBDF condition is used again to take these figures for fair comparison with other two previous samples. The 2000 nm depth was not characterized this time because it is away from He preimplanted region and the data will be the same with Fig.4.4 2000 nm depth. TEM DF image taken from 350 nm region where He ion peaks shows higher density of coherent dispersoid in the matrix compare to other DF images taken from other depths. Figures 4.6 show TEM BF and DF micrographs of 1E16 He pre-implanted and Fe irradiated sample taken from the same WBDF condition with

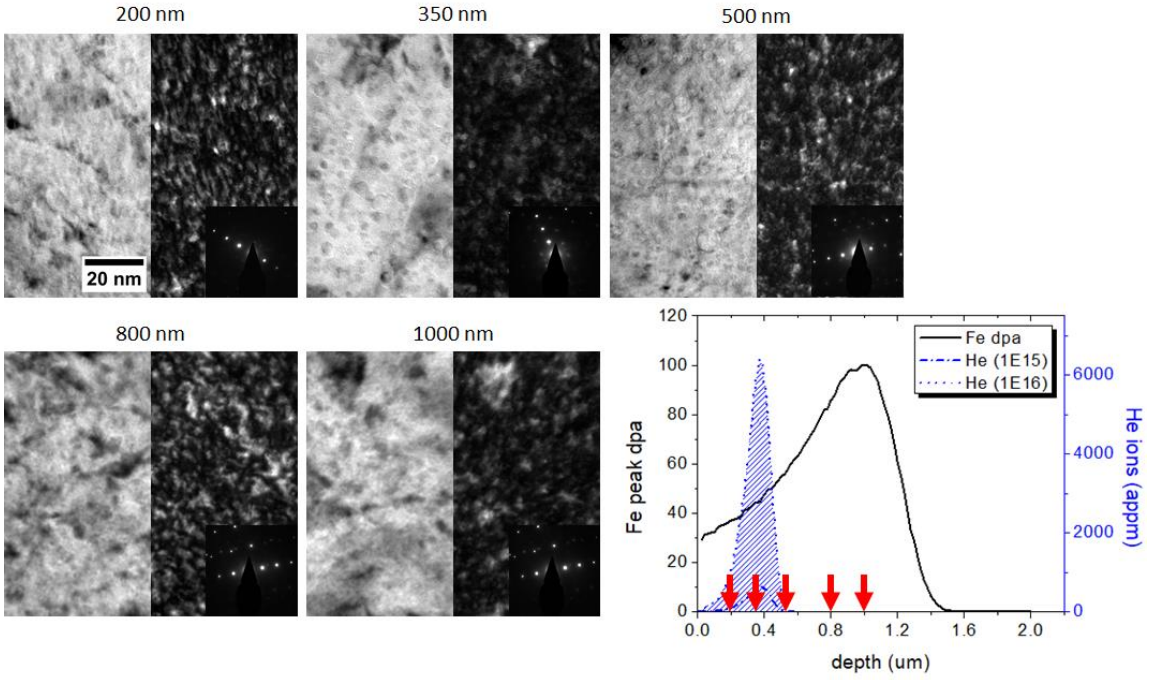

Figure 4.6 TEM bright field and dark field micrographs of 1E16 He preimplanted and Fe irradiated specimen.

others. Unlike Fig. 4.5 1E15 350 nm depth dark field image, Fig. 4.6 1E16 350 nm depth dark field image does not have many bright features shown which implies that higher dose He implantation did not help with the nucleation. Further analysis on size and density on this data will be introduced in section 4.4. Figures 4.7 provide TEM bright field images of

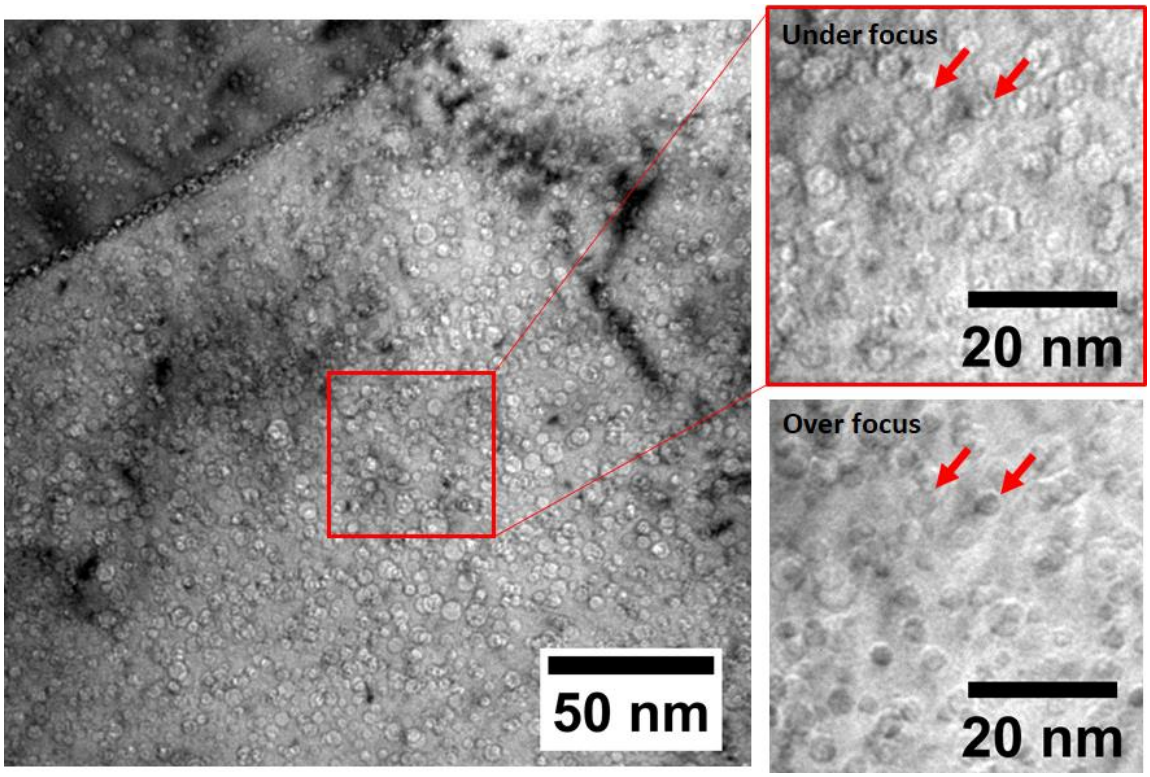

Figure 4.7 TEM bright field micrograph of 1E16 He preimplanted and Fe irradiated specimen taken from 300-500 nm depth region. Under and over focus images were shown on the right side with red arrows indicating two same He bubbles.

1E16 + Fe irradiated sample taken from 300-500 nm depth region. The He bubble size is much larger than 1E15 specimen and the density also look denser. A lot of bubbles were observed on the grain boundaries as shown in Fig. 4.7 due to high grain boundary defect sink strength. It is a common phenomenon at high He environment, and it can further

cause intergranular cracking. Those He bubbles look bright with enhanced edge contrast in under focus image and they look dark with vague boundary in over focus image as shown in Fig. 4.7 right two images. Two same He bubbles are indicated by red arrows in both images.

4.3.4. Oxide Dispersoid Size and Density Comparison

Figure 4.8 shows the dispersoid diameters as a function of depth with different irradiation conditions. Superimposed blue dotted line refers to He ion profile and the black

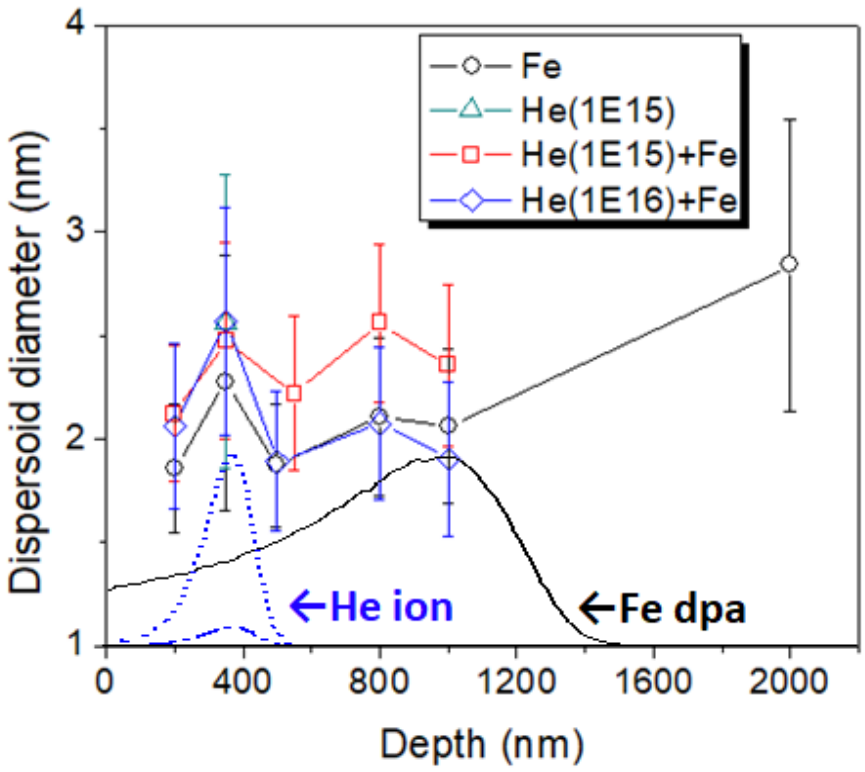

Figure 4.8 Oxide dispersoid diameters of Fe irradiated, He implanted and He+Fe irradiated samples as a function of depth. He ion profile and Fe damage curve are superimposed on the figure.

solid line shows Fe damage profile from SRIM calculation. For just Fe irradiated sample referred by black solid line with circle marker, dispersoid sizes in the ion range are all in the similar range considering the error bars because they are all coherent dispersoids. The size of dispersoid after 1E15 He implantation referred by cyan triangle marker shows almost the same with the size of dispersoid in out of ion range region, which means He implantation itself does not affect dispersoid size.

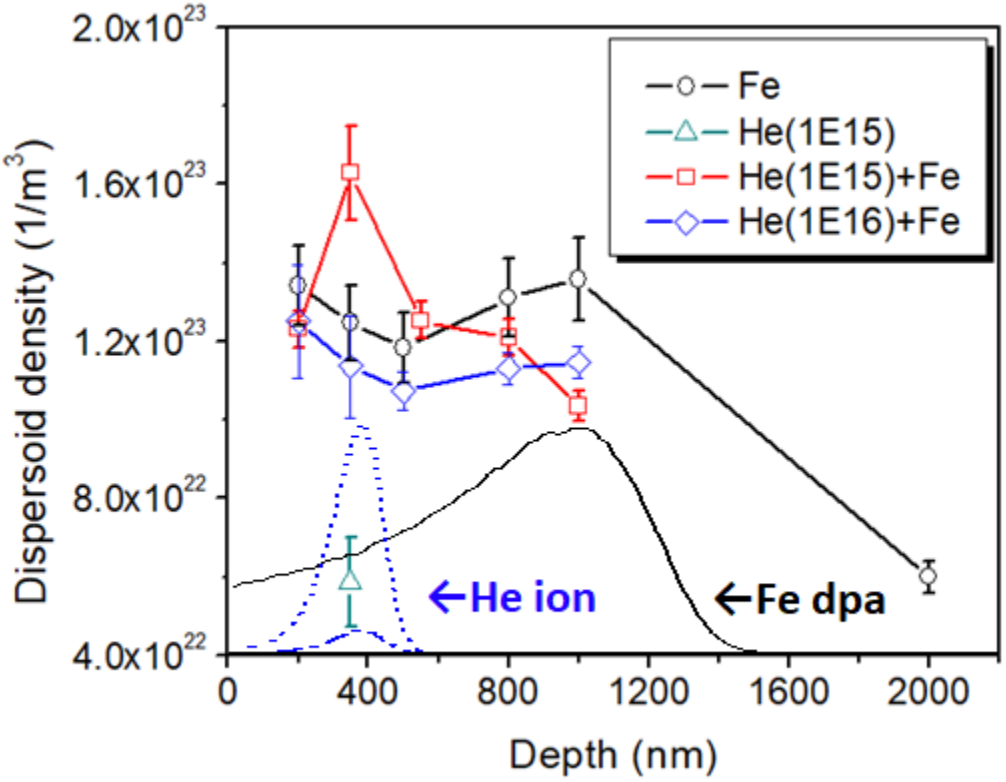

Figure 4.9 Oxide dispersoid densities of Fe irradiated, He implanted and He+Fe irradiated samples as a function of depth. He ion profile and Fe damage curve are superimposed on the figure.

The 1E15 He + Fe irradiated sample indicated by red solid line with square marker showed slightly larger dispersoid sizes in ion range, but this is not related to He preimplantation because the size is also larger after He ion peak (600-1000 nm depth). Therefore, considering the error bars, it can be regarded as fluctuations from sample to sample or grain to grain. The 1E16 He + Fe irradiated sample data is referred by blue solid line with diamond marker and they showed similar dispersoid size profile with the Fe irradiated specimen (black solid with circle marker), which tells us that the 1E16 dose of He preimplantation does not affect on dispersoid size change.

Figure 4.9 shows the dispersoid densities of each sample as a function of depth. The He implanted sample marked with cyan triangle shows similar density with the out of ion range of Fe irradiated sample (2000 nm), which means He implantation itself does not affect dispersoid density. As shown in chapter 3, the coherent dispersoid density increased after Fe irradiation as marked with black solid line with circle markers, and there is 2 times of density increasement at 350 nm depth compared to 2000 nm depth. On the other hand, 1E15 He preimplanted and Fe irradiated sample marked with red solid line with square markers shows the highest coherent dispersoid density at He ion peak which is almost 2.7 times higher than 2000 nm depth of Fe irradiated sample. The lower dispersoid densities at 200 nm and 500-1000 nm region are maybe caused by diffused solutes to 350 nm depth area. In 1E16 He preimplanted and Fe irradiated specimen, the densities of dispersoid are systematically lower than that of Fe irradiated sample within the ion range ($\leq$1000 nm). From this observation, we learned that large size He bubbles do not affect on dispersoid nucleation under irradiation and there is a possibility that the large bubbles even

deteriorate nucleation process. Therefore, we believe that the small size He bubbles in the matrix help dispersoid nucleation during Fe irradiation, resulting in higher density of coherent dispersoids at that region. However, that effect is only valid when the He bubble size is small, and large the He bubbles do not affect on dispersoid nucleation. The coherent dispersoid size and density for each case at 350 nm depth and 2000 nm depth for Fe irradiated case are summarized in Table 4.1.

Table 4.1 Summary of coherent dispersoid size and density for each irradiation case.

	Diameter [nm]	Density [particles/m^3]
Fe (350 nm)	2.3±0.6	$1.2\times10^{23}\pm9.6\times10^{21}$
He (350 nm)	2.6±0.7	$5.9\times10^{22}\pm1.1\times10^{22}$
1E15 He+Fe (350 nm)	2.5±0.5	$1.6\times10^{23}\pm1.2\times10^{22}$
1E16 He+Fe (350 nm)	2.6±0.6	$1.1\times10^{23}\pm1.3\times10^{22}$
Fe (2000 nm)	2.8±0.6	$6.0\times10^{22}\pm4.0\times10^{21}$

Figures 4.10 show oxide dispersoid size distributions of Fe irradiated, He implanted, 1E15 He+Fe irradiated, and 1E16 He+Fe irradiated specimens taken from 350 nm depth region. The black solid lines superimposed on each figure are the size distribution of 2000 nm depth region from Fe irradiated sample for comparison. With an exception of He implanted sample, the size distributions follow gaussian distribution and they show very similar distribution with those from Fe 2000 nm region. The size distributions at 350 nm depth of Fe irradiated sample and 1E16+Fe sample show shifted

size to right direction compared to out of ion range region (2000 nm depth) while other two cases show similar distribution with 2000 nm depth. As only coherent dispersoids were counted in TM phase, the dispersoid size distribution remains in the similar range (1.5 ~ 5.5 nm diameter) for all cases. The He implanted sample (top right) size distribution looks like it has two separated size peaks. However, it is highly likely just caused from

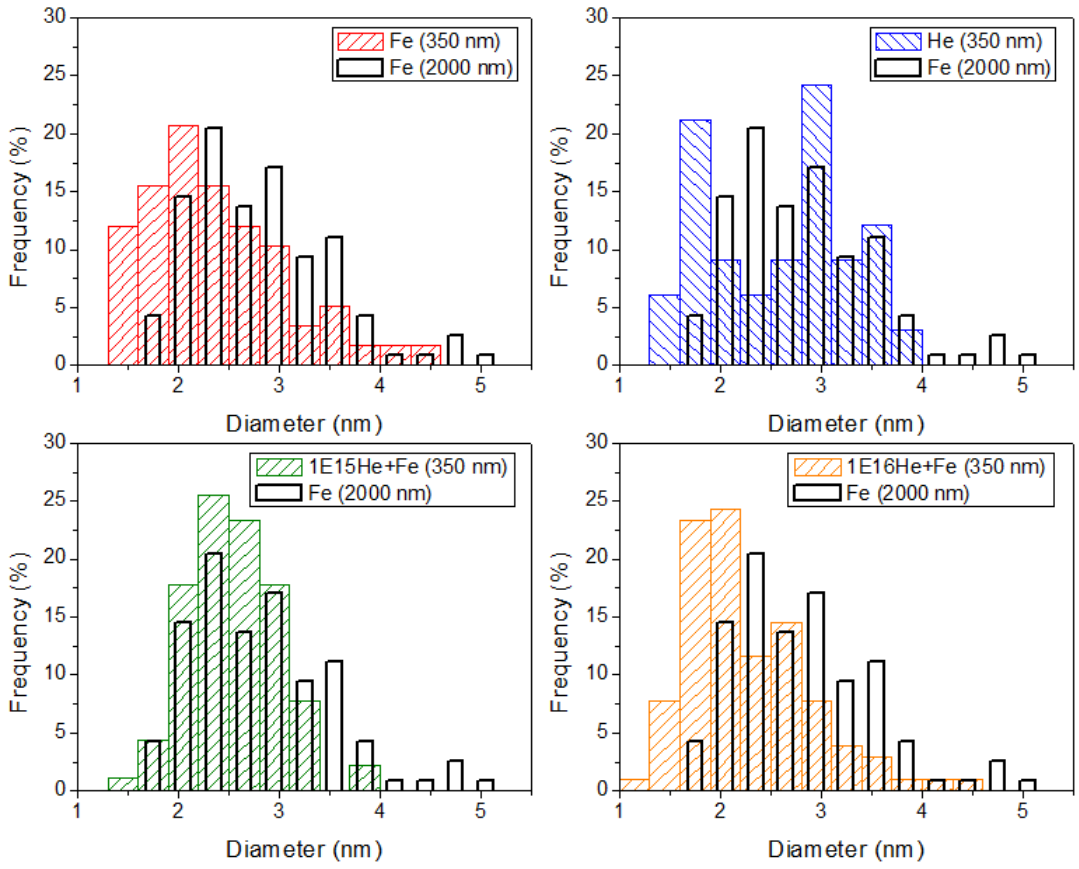

Figure 4.10 Oxide dispersoid size distribution of Fe irradiated, He implanted, 1E15 He+Fe, and 1E16 He+Fe irradiated samples at 350 nm depth. Black lines superimposed are size distribution of 2000 nm depth region of Fe irradiated sample for comparison.

statistic fluctuation due to not enough oxide dispersoid counts from this sample instead of containing any meaning in it.

4.4. Discussion

As He migration energy is low as 0.078 eV, it can migrate fast and be easily trapped at defects such as vacancy, dislocation, grain boundaries, and precipitate surfaces [8]. When He is trapped by vacancy, they form He-vacancy clusters in the matrix [9-13], and those He-vacancy clusters are further can attract oxygen due to high vacancy-oxygen affinity. According to the previous DFT study on vacancy mechanism of high oxygen solubility and nucleation of stable oxygen enriched clusters in Fe, oxygen in interstitial position shows high affinity for vacancies due to weak bonding with host Fe [7]. As shown in Figure 4.11, this O-vacancy mechanism further enables the nucleation of O-enriched nanoclusters, and it further attracts solutes with high oxygen affinities like Ti and Y. And finally, if it riches certain concentration, oxide dispersoids are formed. In a similar

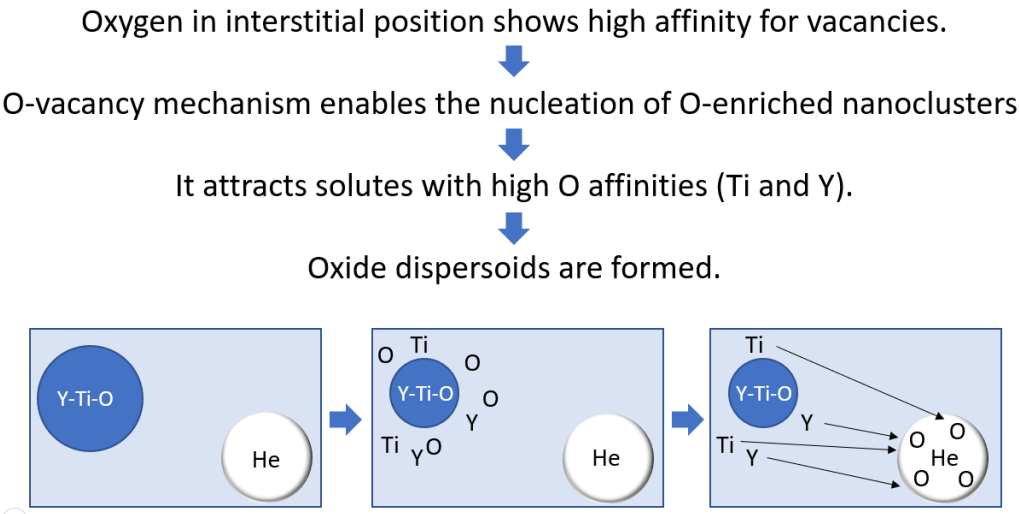

Figure 4.11 Mechanism of nucleation of oxide dispersoid with presence of vacancy.

mechanism, when oxide dispersoid and He bubble are present in the matrix, oxide dispersoid will dissolve under irradiation. Then, oxygens from dispersoid and matrix will form oxygen enriched nanoclusters which further attract Ti and Y to form oxide dispersoids. Therefore, increment of coherent dispersoid density was observed in 1E15 He + Fe irradiation case due to this mechanism. However, when 1E16 He was implanted followed by Fe irradiation, dispersoid density did not show an increment. We believe, in this case, the same mechanism happens in the matrix, but the solute concentration around the He-vacancy cluster does not reach critical point for nucleation due to large surface area and volume of 1E16 He bubbles.

Although we can use this vacancy mechanism to explain how new oxide dispersoid can be formed, still the better way to confirm this hypothesis is conducting in-situ TEM while irradiating material at high temperature and also using a modeling to support the experimental results.

4.5. References

[1] J. G. Gigax, H. Kim, E. Aydogan, F. A. Garner, S. A. Maloy, L. Shao, Beam-contamination-induced compositional alteration and its neutron-atypical consequences in ion simulation of neutron-induced void swelling, Mater. Res. Lett 5 (7) (2018) 478-495.

[2] L. Shao, J. G. Gigax, D. Chen, H. Kim, F. A. Garner, J. Wang, M. B. Toloczko, Standardization of accelerator irradiation procedures for simulation of neutron induced damage in reactor structural materials, Nucl. Instrum. Meth. Phys. Res. B 409 (2017) 251-254.

[3] J. G. Gigax, H. Kim, E. Aydogan, L. M. Price, X. Wang, S. A. Maloy, Impact of composition modification induced by ion beam Coulomb-drag effects on the nanoindentation hardness of HT9, Nucl. Instrum. Meth. Phys. Res. B 444 (2019) 68-73.

[4] J. F. Ziegler, M. D. Ziegler, J. P. Biersack, SRIM e the stopping and range of ions in matter, Nucl. Instrum. Meth. Phys. Res. B 268 (2010) 1818-1823.

[5] R. E. Stoller, M. B. Toloczko, G. S. Was, A. G. Certain, S. Dwaraknath, F. A. Garner, On the use of SRIM for computing radiation damage exposure, Nucl. Instrum. Meth. Phys. Res. B 310 (2013) 75-80.

[6] S. J. Zinkle, L. L. Snead, Opportunities and limitations for ion beams in radiation effects studies: bridging critical gaps between charged particle and neutron irradiations, Scripta Mater. 143 (2018) 154-160.

[7] C. L. Fu, M. Krcmar, G. S. Painter, X. Chen, Vacancy mechanism of high oxygen solubility and nucleation of stable oxygen-enriched clusters in Fe, Phys. Rev. Lett. 99, 225502 (2007).

[8] R. Kemp, G. Cottrell, H. K. D. Bhadeshia, Classical thermodynamic approach to void nucleation in irradiated materials, Energy Mater. 1 (2) (2006) 103–105.

[9] K. Morishita, K. Sugano, B. D. Wirth, T. Diaz de la Rubia, Thermal stability of helium-vacancy clusters in iron, Nucl. Instrum. Meth. B 202 (2003) 76–81.

[10] C. L. Fu, F. Willaime, Ab initio study of helium in α-Fe: Dissolution, migration, and clustering with vacancies, Phys. Rev. B 72 (2005) 064117.

[11] L. Ventelon, B. D. Wirth, C. Domain, Helium-self-interstitial atom interaction in α-iron, J. Nucl. Mater. 351 (2006) 119–132.

[12] V. A. Borodin, P. V. Vladimirov, A. Möslang, Lattice kinetic Monte-Carlo modelling of helium-vacancy cluster formation in bcc iron, J. Nucl. Mater. 367–370 (2007) 286–291.

[13] N. Gao, M. Victoria, J. Chen, H. Van Swygenhoven, Formation of dislocation loops during He clustering in bcc Fe, J. Phys.: Condens. Matter 23 (2011) 245403.

[14] D. Stewart, Y. Osetskiy, R. Stoller, Atomistic studies of formation and diffusion of helium clusters and bubbles in bcc iron, J. Nucl. Mater. 417 (2011) 1110–1114.

[15] H. Q. Deng, W. Y. Hu, F. Gao, H. L. Heinisch, S. Y. Hu, Y. L. Li, R. J. Kurtz, Diffusion of small He clusters in bulk and grain boundaries in α-Fe, J. Nucl. Mater. 442 (2013) S667–S673.

[16] T. Chen, E. Aydogan, J. G. Gigax, D. Chen, J. Wang, X. Wang, S. Ukai, F. A. Garner, L. Shao, Microstructural changes and void swelling of a 12Cr ODS ferritic-martensitic alloy after high-dpa self-ion irradiation, J. Nucl. Mater. 467 (2015) 42–49.

[17] T. Chen, J. G. Gigax, L. Price, D. Chen, S. Ukai, E. Aydogan, S. A. Maloy, F. A. Garner, L. Shao, Temperature dependent dispersoid stability in ion-irradiated ferritic-

martensitic dual-phase oxide-dispersion-strengthened alloy: Coherent interfaces vs. incoherent interfaces, Acta Mater. 116 (2016) 29-42.

[18] G. R. Odette, M. J. Alinger, B. D. Wirth, Recent Developments in Irradiation-Resistant Steels, Annu. Rev. Mater. Res. 38, (2008) 471–503.

[19] C. Lu, Z. Lu, X. Wang, R. Xie, Z. Li, M. Higgins, C. Liu, F. Gao, L. Wang, Enhanced radiation-tolerant oxide dispersion strengthened steel and its microstructure evolution under helium-implantation and heavy-ion irradiation, Sci. Rep. 7 (2017) 40343.

[20] G. L. Kulcinski, D. G. Doran, M. A. Abdou, Properties of Reactor Structural Alloys after Neutron or Particle Irradiation, in ASTM STP 570, ASTM, Philadelphia (1974) 329-351.

[21] R. E. Stoller, G. R. Odette, F. A. Garner, N. H. Packan, A. S. Kumar, A Comparison of the Relative Importance of Helium and Vacancy Accumulation in Void Nucleation ASTM STP 955, ASTM, Philadelphia (1987) 358–370.

[22] Y. Dai, G. R. Odette, T. Yamamoto, The Effects of Helium in Irradiated Structural Alloys, Comprehensive Nuclear Materials, Elsevier, Oxford, (2012) 141–193.

[23] C. Lu, Z. Lu, R. Xie, C. Liu, L. Wang, Microstructure of a 14Cr-ODS ferritic steel before and after helium ion implantation, J. Nucl. Mater. 455 (2014) 366-370.

[24] S. Chen, K. Tadaki, Y. Wang, N. Hashimoto, S. Ohnuki, Effect of oxide particles and pre-implanted helium on defect evolution during electron irradiation, Mater. Trans. 55 (2014) 443-446.

5. DPA RATE STUDY ON HF DOPED ODS ALLOY*

5.1. Introduction

Oxide-dispersion-strengthened (ODS) alloys represent one class of candidate alloys with promising application in nuclear reactors due to their good creep resistance and high temperature strength [1-4]. The oxide dispersions help to stabilize grain boundaries, block dislocation motion, and act as possible defect sinks for point defect trapping and defect annihilation [2,7,8]. However, the superior performance of ODS alloys, in general, depends on the stability and structural morphologies of the dispersoids. Numerous studies have shown that under ion irradiation, dispersoids are not stable in their sizes, densities, volume fractions or chemical compositions [5, 6, 9-16]. Wharry and Swenson summarized a wide variety of dispersoid morphology evolution including reduced, increased, and no change in the dispersoid sizes, suggesting that multiple active mechanisms influencing dispersoid irradiation evolution [10]. Recent studies have brought insights into the complicated nature of dispersoid stability under irradiation [11, 12, 14], such as cascade morphology effect and dose rate effect [11], chemical composition effect [12], and dissolution-reprecipitation mechanism [14]. Swenson et al. conducted a study comparing neutron, proton and heavy ion irradiation for the dose rate

* Reprinted with permission from "Dispersoid stability of ion irradiated oxide-dispersion-strengthened alloy" by Hyosim Kim, Jonathan G. Gigax, Tianyi Chen, Shigeharu Ukai, Frank A. Garner, Lin Shao, 2018. *Journal of Nuclear Materials*, 509, 504-512, Copyright 2018 by Elsevier.

effects in dispersoid stability [11]. Their study has four orders of magnitude in dose rates, and the dose rate effect is coupled with different cascade morphologies [11]. Therefore, it is valuable to investigate the dose rate effects by using one single particle type, which is the motivation of the present study.

The dispersoid evolution under irradiation is governed by two competing effects: dispersoid dissolution due to damage cascade recoiling and recovery arising from back-diffusion. The shrinkage of dispersoids under irradiation is described by [17].

$$\frac{dr}{dt} = -K\psi \tag{5.1}$$

where r is the dispersoid radius, t is time, K is the dpa (displacements per atom) rate, ψ is a parameter to describe the efficiency of damage cascades to dissolve dispersoids. ψ is a product of l and f, where l is the thickness of a dispersoid shell which are affected by recoil damage cascades and f is the fraction of solute atoms dissolved. Hence ψ has a unit of length.

The dissolution of dispersoids leads to a concentration increase in the matrix surrounding dispersoids. Driven by a concentration gradient, back-diffusion of recoiled solutes tends to increase the dispersoid size. When these two competing effects are balanced, dispersoid sizes approach to an equilibrium value, r_e, as calculated by [18].

$$r_e = \frac{D}{K\psi} \cdot \frac{c - c_r}{c_p - c_r} \tag{5.2}$$

where D is the solute diffusion coefficient influenced by radiation-induced defects, c is the solute concentration in the matrix, c_p is the solute concentration in the dispersoid, c_r

is the solubility limit at the dispersoid-matrix interface. The solubility limit at the interface is expressed as [18]

$$c_r = c_\infty \exp\left(\frac{2\gamma_i v_{at}}{kTr}\right) \tag{5.3}$$

where c_∞ is the solubility for a flat interface (r=∞), γ_i is the unit interfacial energy at the dispersoid-matrix interface, v_{at} is the average atomic volume in the dispersoid, T is the temperature, and k is the Boltzmann constant.

Early studies did not observe a strong dose-rate dependency of dispersoid sizes [6]. According to Eq. 2, the dispersoid sizes depend on K. Hence, diffusivity D must consider dose rate effects, which counterbalances dispersoid dissolution (the effect from K) and let dispersoid diameters become insensitive to dose rate effects.

Heavy ion irradiation can induce solute redistribution and has been modelled via rate theory [19,20]. Solute migration mediated by defects produced by irradiation (i.e. vacancies and self-interstitial atoms) was shown to result in solute gradients that, in some cases, mirror irradiation-induced defect profiles. Early studies using a focused electron beam to locally introduce damage has shown that dose rate gradients over a length scale of one micron can significantly change microchemistry due to point defect flow. The dose rate gradient effect in heavy ion irradiation, if there is any, should be detectable [20]. The sensitivities of both dispersoid dissolution and solute migration to dpa rates can be well tested in ion irradiation experiments through depth profiling of void evolution and depth dependent dispersoid characterization. Although the magnitudes of dpa rate difference are limited, the study has certain advantage of minimizing beam-heating effects, since only

one beam current is used. Therefore, we utilized heavy ion irradiation in the present study to examine the oxide evolution in an Hf-doped ODS alloy. The Hf-doped alloy is specifically selected since it is extreme swelling resistant, which minimizes the complexity from dispersoid-void interactions.

5.2. Experimental Procedure

An Hf-doped ferritic ODS alloy fabricated by Kobelco Research Company was used in this study. The details of fabrication procedure are reported elsewhere [21]. First, the ferritic steel powder and Y_2O_3 powder are mechanically alloyed and agitated for up to 48 hrs under argon gas atmosphere. Then, it is degassed at high temperature in 0.1 Pa vacuum for 2 hrs, followed by hot extrusion at 1423 K. Hf was intentionally added for dispersoid refinement [22]. The chemical composition of this alloy is provided in Table 5.1. The alloy was cut into specimens of 5 mm×3 mm×2 mm, and mechanically polished down to a 0.7 mm thickness by using SiC paper (down to 4000 grit). The final polishing step used a 0.04 micron alumina suspension. The sample was then electropolished at room temperature using a mixture of 7% perchloric acid and 93% acetic acid. The graphite cathode and the sample were biased at a voltage of 2 V and separated at a distance of 4 cm. A magnetic stirring bar was kept spinning while polishing, and the total polishing time was 20 sec.

The specimen was irradiated at 475°C by 3.5 MeV Fe2+ ions to a fluence of 9.54×1016 ions/cm2, equivalent to 100 peak dpa. The temperature was selected since it is close to maximum swelling temperature of ferritic alloys [23-26]. The beam was static as the best practice to avoid the rastering/pulse beam effect [27]. The beam spot was about 6

mm×6 mm and the current was controlled to be ~200 nA. Liquid nitrogen cold traps located in the beam line and target chamber were used during irradiation to keep high vacuum (<10-8 torr). To reduce beam-induced carbon contamination, multiple beam deflectors were used to filter the carbon contaminants off the Fe beam trajectories. Details of these instrumental setups to reduce beam contamination can be found elsewhere [28,29]. The damage calculation used Stopping and Range of Ions in Matter (SRIM) [30], with Kinchin-Pease option and an Fe displacement threshold energy of 40 eV [31].

Irradiated samples were characterized by transmission electron microscopy (TEM) with TEM specimens prepared by using the focused ion beam (FIB) lift-out technique. The FIB specimen size was ~10 μm × ~7 μm × ~200 nm in the first-stage of preparation. Then 30 keV Ga beam was changed to 5 keV for the second-stage fine thinning to a thickness of ~100 nm. TEM characterization was performed using 200 keV FEI Tecnai G2 F20 Super-Twin and FEI Tecnai F20, and FIB was performed using Tescan Lyra-3. Bright field (BF), weak beam dark field (WBDF), scanning transmission electron microscopy (STEM) – high angle annular dark field (HAADF), high resolution TEM (HRTEM), energy dispersive spectroscopy (EDS), and electron energy loss spectroscopy (EELS) were used to characterize the samples. Dispersoids size measurement is challenging for ultra-fine dispersoids (< 1 nm) due to the resolution limit of TEM. Atom probe tomography (APT) is more appropriate to characterize small dispersoids. Recent comparison studies suggest that sizes and densities of small oxide dispersoids measured by TEM and APT are comparable to each other [9]. The dispersoid sizes in the present study, although small, are still in the reliable characterization capability of TEM.

Furthermore, TEM is critical for the present study in order to check coherency of dispersoids.

Table 5.1 Composition of Hf-doped ODS alloy (wt.%)

Fe	Cr	C	Si	Mn	P
Bal.	15.44	0.024	0.03	0.01	<0.005
S	W	Al	Ti	Hf	Y_2O_3	Excess O
0.002	1.80	3.90	0.12	0.59	0.33	0.10

5.3. Results

Figures 5.1 compare TEM cross-sectional micrographs before and after irradiation. The upper white dashed lines designate the sample surface and lower white dashed line in Fig. 5.1(b) defines the end of the ion bombarded region. The red solid line and red dashed line superimposed on Fig. 5.1(b) are the dpa profile and the Fe implant profile, respectively, calculated by using the SRIM code [30]. There are no noticeable changes in grain morphologies after irradiation. The inset in Fig. 1a shows typical oxide dispersoid morphologies in the as-received condition. Dispersoid size in the unirradiated specimen (Fig. 5.1(a)) were measured to be 5.1±0.8 nm, while the dispersoid sizes were measured to be 4.2±0.7 nm in the region beyond the ion range in the irradiated specimen (Fig. 5.1(b)). Hence, thermal annealing (corresponding to depths beyond the bombarded region) does not significantly change the dispersoid size, considering statistics. In both samples, there are large particles exhibiting either white contrast or dark contrast. The large particles (>100 nm) of white contrast are Hf-Ti-O, while the large particles (>50 nm) of

dark contrast are Al_2O_3. Ar gas bubbles over 50 nm diameter were occasionally observed in the matrix as well. These particles and bubbles were introduced during alloy fabrication

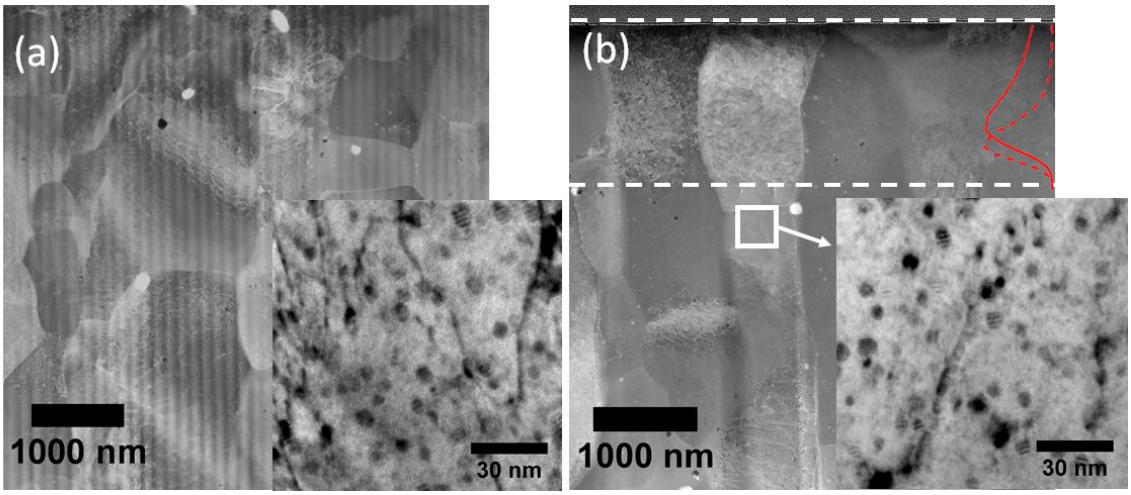

and their densities are very low. Hence, they are not subjects of interest in the present study.

Figure 5.1 STEM-HAADF and TEM BF micrographs of Hf-doped ODS (a) before irradiation and (b) after 100 peak dpa irradiation. SRIM calculation of dpa (red solid line) and Fe implant (red dashed line) are superimposed in (b). Two white dashed lines in (b) refer to boundaries of the damaged region.

Figure 5.2 shows a TEM cross-sectional micrograph of an irradiated sample, superimposed with the SRIM dpa and Fe implant profiles. The dpa peaks at a depth of ~1000 nm and the Fe implant peaks at ~1200 nm. In order to study the local dpa rate effect, five locations (as marked by black dashed lines) at depths of 250 nm (6.71×10^{-4} dpa/s), 650 nm (1.19×10^{-3} dpa/s), 1000 nm (1.73×10^{-3} dpa/s), 1200 nm (1.06×10^{-3} dpa/s), and 2000 nm (0 dpa/s) are characterized.

Dispersoids in the unirradiated sample were analyzed with EDS and HRTEM for chemical composition and structural information. HRTEM is useful to tell interfacial coherency of dispersoids and matrix. Recent studies have shown that the chemical composition of dispersoid plays an important role in the microstructure and radiation stability of the materials [11-13,32]. Figure 5.3(a) shows a STEM-HAADF image of an oxide particle smaller than 10 nm (in an unirradiated sample). The line in Fig. 5.3(a) refers to EDS line scan across the particle. The circle and the cross refer to EDS point analysis within the particle and in the matrix, respectively. As shown in Fig. 5.3(b), the Fe, Cr, and Al yields statistically fluctuate without a conclusive compositional variation, but Y enrichment is

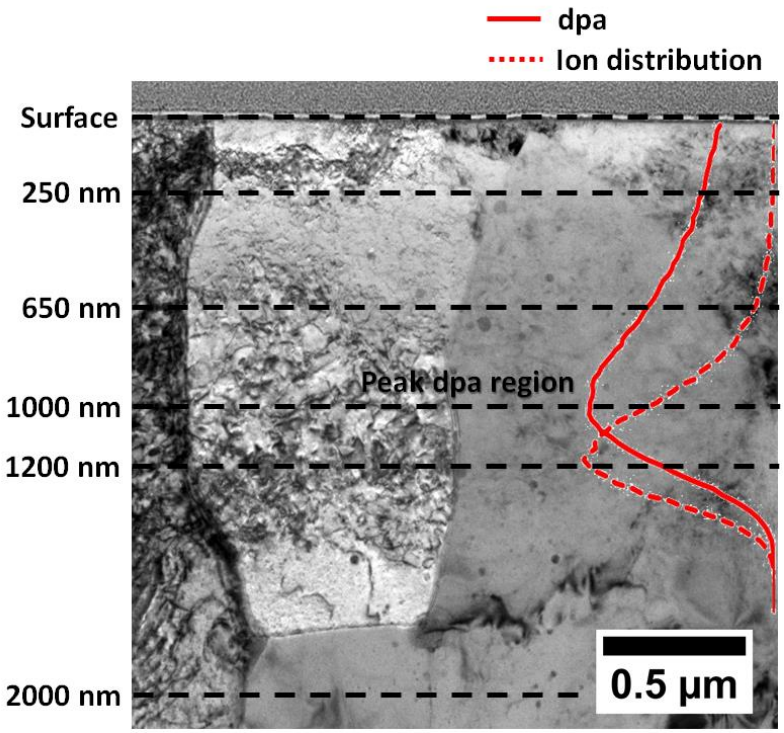

Figure 5.2 TEM bright field image of 100 peak dpa irradiated Hf-doped ODS. Five different depth regions are characterized, as marked by black dashed lines. SRIM-calculated dpa and Fe ion distribution profiles are superimposed.

obvious within the particle. The two black dashed lines are used to mark where the particle starts and ends. Fig. 5.3(c and d) show two point scan results from oxide particle and matrix, respectively. Two red arrows point to yttrium signals. Yttrium appears within the dispersoid but disappears in the matrix.

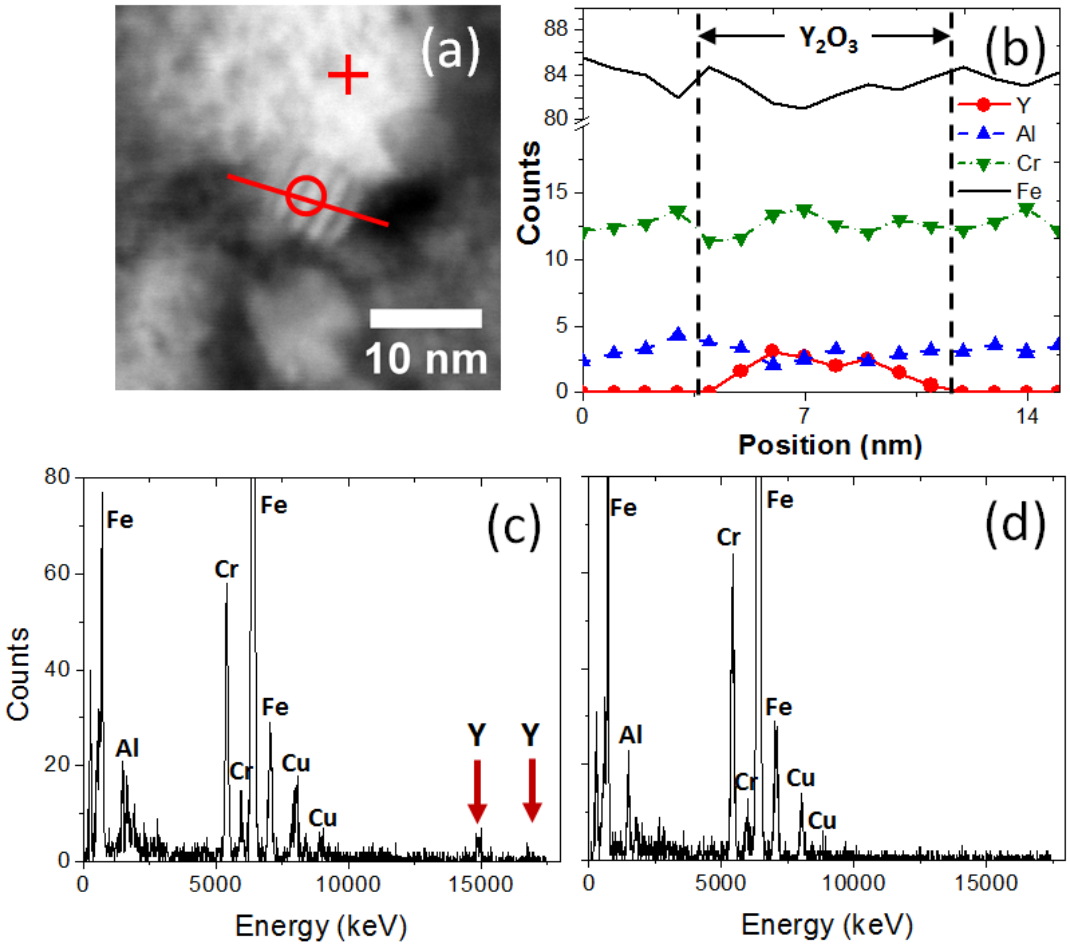

Figure 5.3 (a) STEM-HAADF image of an oxide particle smaller than 10 nm in unirradiated sample, (b) EDS line spectrum (as marked by the red line marked in (a)), with two dash lines marking the starting and ending positions of the oxide particle, (c) point spectrum obtained within the nano-oxide particle (as marked by the red circle in (a)), and (d) point spectrum from matrix (as marked by the red cross in (a)).

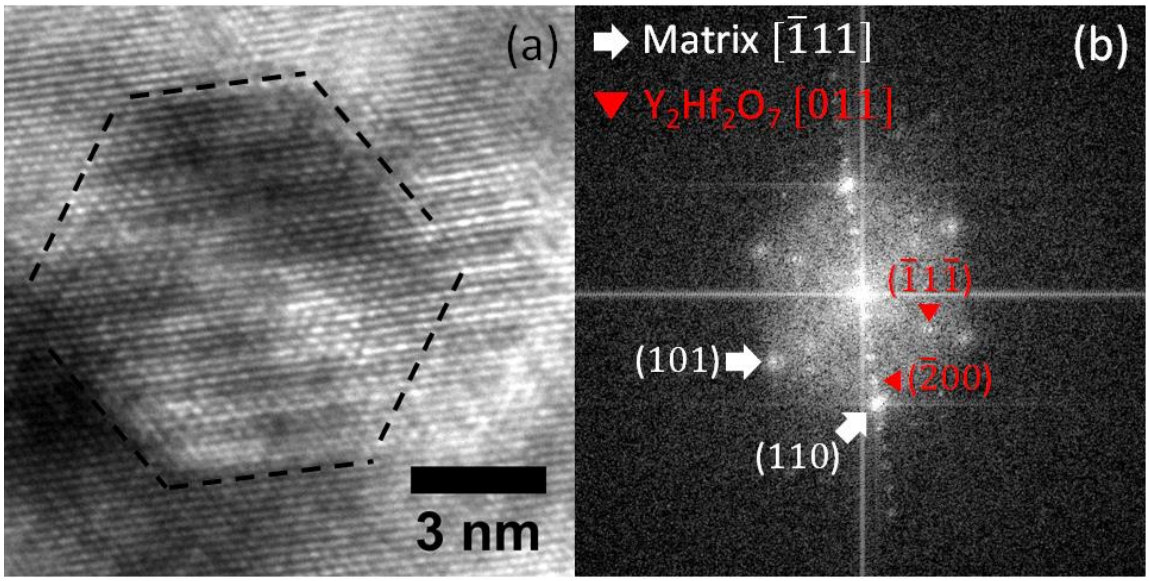

Figure 5.4 (a) HRTEM image of a dispersoid in an unirradiated sample with dispersoid-matrix interfaces marked by black dashed lines and (b) the corresponding Fast Fourier Transformation (FFT) image.

Figure 5.4(a) shows a high resolution TEM (HRTEM) micrograph of an oxide particle of ~8 nm in diameter, taken from the [$\bar{1}$11] zone axis of the matrix. The particle has a faceted morphology, which is a sign of developing coherent interfaces. Fig. 5.4(b) shows the corresponding Fast Fourier Transform (FFT) image, with the patterns of the matrix marked with white arrows and the patterns of the particle marked with red triangles. The patterns of the particle suggest a fluorite structure of $Y_2Hf_2O_7$. The FFT pattern also shows matrix-oxide interface coherency of $(110)_{Matrix}//(\bar{2}00)_{Particle}$ and $[\bar{1}11]_{Matrix}//[011]_{Particle}$. It is reported by Dou et al. that $Y_2Hf_2O_7$ particle and bcc Fe-Cr matrix can have orientation correlation of $(1\bar{1}0)_{Matrix}//(0\bar{2}0)_{Particle}$ and $(001)_{Matrix}//(001)_{Particle}$ [33].

Figure 5.5(a) plots the damage and Fe implant profiles, with arrows marking the regions locally characterized by TEM. Figs. 5.5(b-f) show the bright field and dark field micrographs at depths of 250 nm, 650 nm, 1000 nm, 1200 nm and 2000 nm, respectively. The above depths correspond to 39 dpa (at 250 nm, 6.7×10^{-4} dpa/s), 69 dpa (at 650 nm, 1.2×10^{-3} dpa/s), 100 dpa (at 1000 nm, 1.7×10^{-3} dpa/s), 61 dpa (at 1200 nm, 1.1×10^{-3} dpa/s), and 0 dpa (at 2000 nm). The particles having dark contrast in the bright field TEM images are oxide dispersoids. Similar to the previous studies by Chen et al. [6], when the **g**110 direction is excited, dispersoids coherent to (110) of the matrix appear as bright features in the dark field imaging. Both dispersoid types appear dark or gray in the bright field images, but only coherent dispersoids appear bright in the dark field images. Hence, the comparison between bright field and dark field images can differentiate coherent and incoherent dispersoids. Note that, as we selected one of the six (110) planes by selecting one specific **g**110 direction to check the coherency, there is a possibility that some coherent dispersoids may not show up in the dark field image. However, as both coherent and incoherent dispersoid diameters are smaller than 10 nm, we assumed that all six (110) planes will develop the same coherency with the matrix, and one dark field image taken from one specific **g**110 direction can represent other five directions. For large dispersoids in Fig. 5.5(f), they appear with Moiré fringes, suggesting a slight lattice mismatch of the dispersoid to $(110)_{Matrix}$. These semi-coherent dispersoids also appear as bright in the dark field images. In comparison with the dispersoids at 2000 nm, which is beyond the Fe range, all dispersoids within the irradiated regions are smaller.

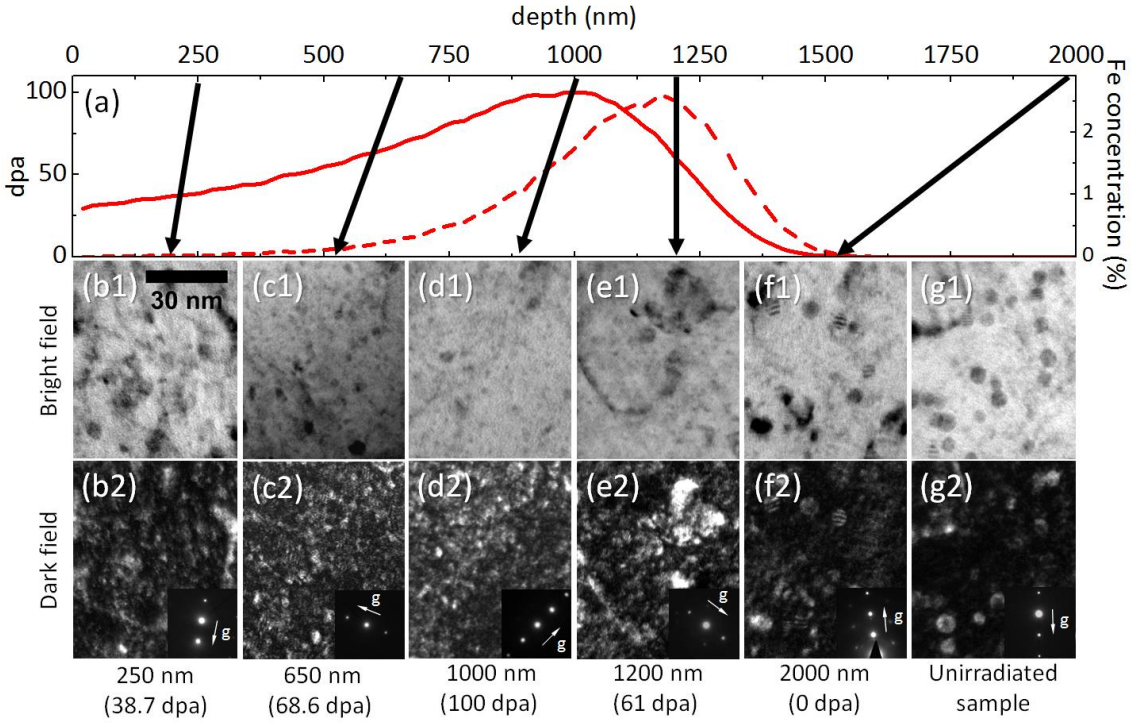

Figure 5.5 (a) Dpa (red solid line) and Fe implant (red dashed line) profiles, and (b1-g1) BF micrographs at depths of 250 nm (irradiated), 650 nm (irradiated), 1000 nm (irradiated), 1200 nm (irradiated), 2000 nm (irradiated), and from unirradiated sample (as a comparison with irradiated samples), and (b2-g2) corresponding WBDF micrographs and TEM diffraction patterns taken at (g, 3g) condition with g_{110} direction excited.

Figures 5.6(a-e) summarize the detail statistical distributions of dispersoid sizes at different depths of the irradiated sample and compare the data with the sizes of unirradiated sample (Fig. 5.6(f)). The dark bars refer to coherent dispersoids and the gray bars refer to incoherent dispersoids. The solid blue line refers to the mean size of coherent dispersoids and the dash red line refers to the incoherent dispersoids. In unirradiated sample, the mean sizes of coherent dispersoids and incoherent dispersoid are very close to each other. After ion irradiation, both types of dispersoids shrink. But the mean sizes of

coherent dispersoids are consistently smaller than that of incoherent dispersoids. The size distributions of dispersoids at the depth of 2000 nm (corresponding to 0 dpa) are different from that obtained from unirradiated sample, suggesting that thermal annealing effect only during the irradiation plays a role to change dispersoids.

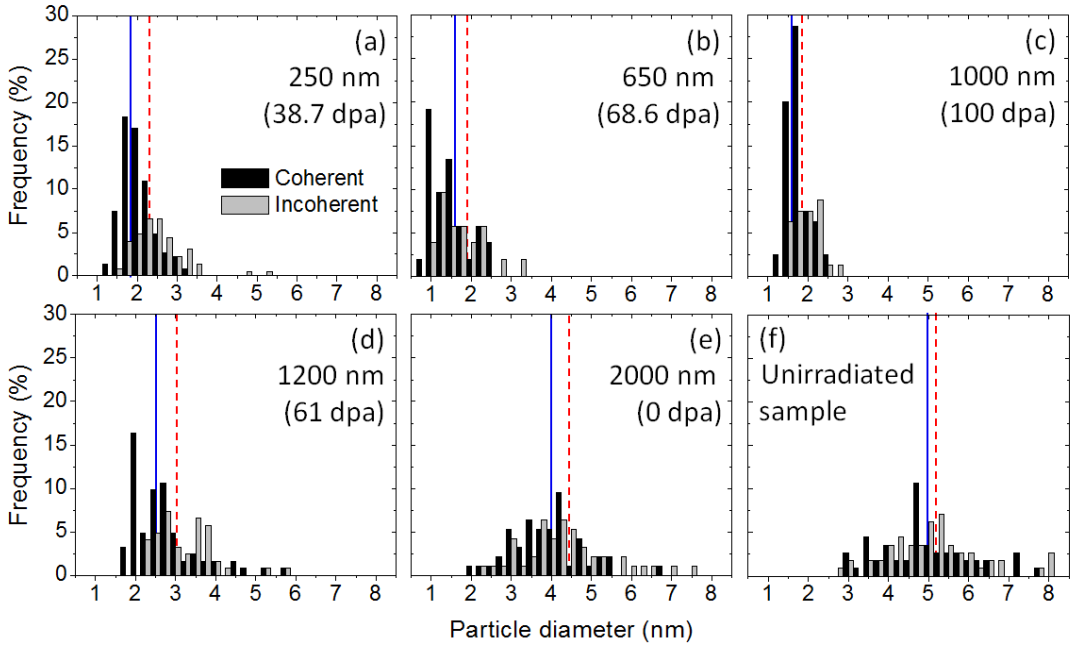

Figure 5.6 Dispersoid size distributions of irradiated Hf ODS alloy at depths of (a) 250 nm (38.7 dpa), (b) 650 nm (68.6 dpa), (c) 1000 nm (100 dpa), (d) 1200 nm (61 dpa), (e) 2000 nm (0 dpa), and (f) unirradiated sample, respectively. The dark bars refer to coherent dispersoids and the gray bars refer to incoherent dispersoids. The solid blue lines and dashed red lines refer to mean diameters of coherent dispersoids and incoherent dispersoids, respectively.

Figure 5.7(a) summarizes the size distributions at different depths. For each depth, more than 70 oxide particles were characterized. Although ion irradiation shrinks dispersoids, incoherent dispersoids are still statistically larger than coherent dispersoids at

all depths. Within the irradiation region shallower than 1000 nm, the mean sizes of dispersoids of both types do not show obvious depth (or equivalently, dpa and dpa rate) dependencies. The mean sizes of incoherent dispersoids are 2.4±0.7 nm at depth 250 nm, 1.9±0.6 nm at depth 650 nm, 1.8±0.4 nm at depth 1000 nm, 3.1±0.7 nm at depth 1200 nm, 4.5±1.2 nm at depth 2000 nm, and 5.2±1.2 nm for unirradiated sample. The mean sizes of coherent dispersoids are 1.9±0.4 nm, 1.6±0.5 nm, 1.6±0.3 nm, 2.6±0.8 nm, 4.4±1.0 nm at the corresponding depths, respectively, and 5.0±1.2 nm for unirradiated sample. Table 5.2 lists mean, standard, skewness and kurtosis values of dispersoid size distributions.

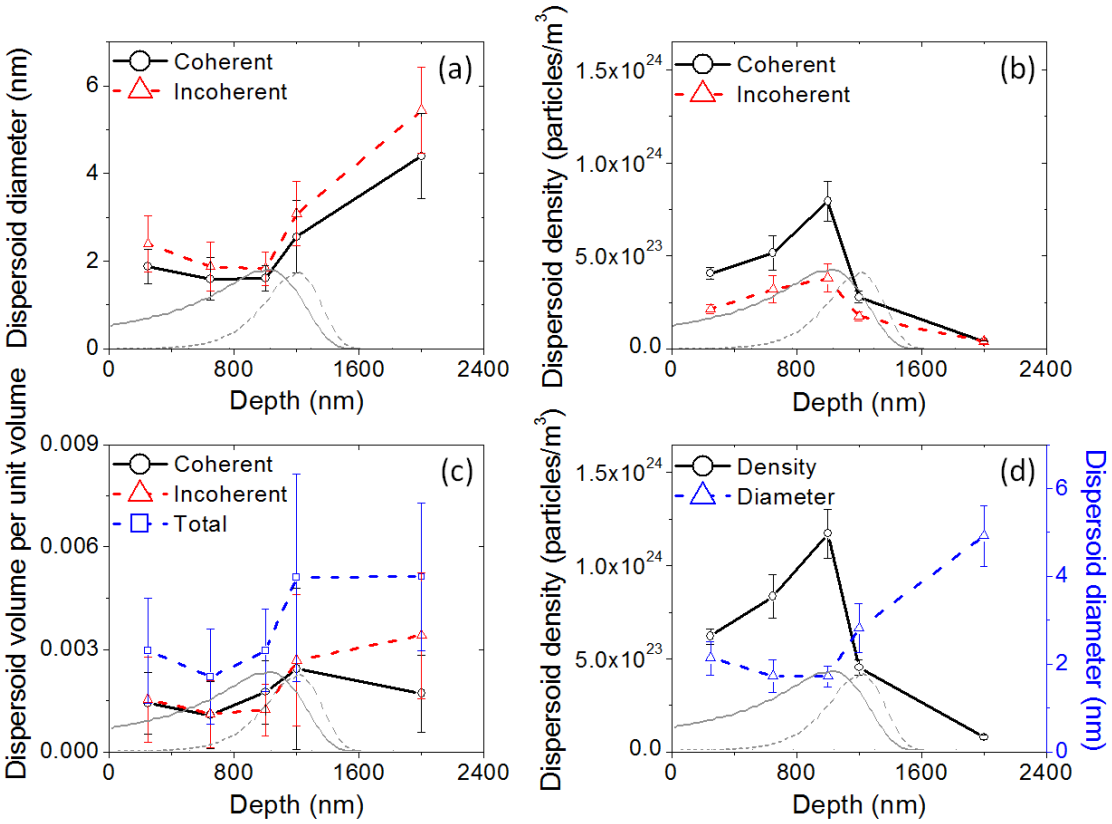

Figure 5.7 Depth distributions of (a) dispersoid diameter, (b) dispersoid density, (c) dispersoid volume fraction, and (d) total dispersoid density and average diameter. Dpa (gray solid line) and Fe implant (gray dashed line) profiles are superimposed on each graph.

Fig. 5.7(b) plots the dispersoid densities as a function of depth. Coherent dispersoids are systematically denser than incoherent dispersoids. Dispersoid densities at 250 nm and 650 nm are comparable to each other (about ~5×10^{23} m^{-3} for coherent dispersoids and ~3×10^{23} m^{-3} for incoherent dispersoids for both depths). At 1000 nm corresponding to the dpa peak, the dispersoid densities are higher (~8×10^{23} m^{-3} for coherent dispersoids, and ~4×10^{23} m^{-3} for incoherent dispersoids). The total dispersoid density at 1000 nm is about 1.5 times that at 250 nm.

Table 5.2 Mean, standard deviation, skewness and kurtosis values of dispersoid size distribution.

Depth		250 nm	650 nm	1000 nm	1200 nm	2000 nm	Unirradiated
Mean	Coherent	1.89	1.59	1.62	2.55	4.02	5.00
	Incoherent	2.39	1.88	1.83	3.08	4.47	5.23
Standard deviation	Coherent	0.39	0.48	0.29	0.82	0.92	1.16
	Incoherent	0.65	0.55	0.38	0.73	1.16	1.19
Skewness	Coherent	0.79	0.78	0.72	1.60	0.46	0.46
	Incoherent	1.50	1.03	0.75	1.11	0.80	0.57
Kurtosis	Coherent	0.46	-0.06	0.21	2.76	0.57	-0.07
	Incoherent	4.16	0.88	0.97	2.04	0.73	0.43

Fig. 5.7(c) presents the dispersoid volume fraction. The volume fractions of coherent and incoherent dispersoids are comparable to each other within the irradiated region. For the irradiated region at depths ≤1200 nm, the total dispersoid volume fractions

are systematically lower than that out of the irradiation region. The missing solute atoms can either diffuse towards the surface or be dissolved into the matrix under irradiation. Due to the fact that there is no enhancement of yttrium-rich precipitates near the surface, it is most likely that these solutes are dissolved in the matrix. Based on the volume fraction difference, the atomic density of dissolved solute atoms is estimated to around 0.18 %. It is worth noting that, under irradiation, coherent particles undergo a much less significant volume reduction than incoherent particles do, suggesting that, at the irradiation temperature of 475 °C, coherent particles are more stable than incoherent particles. This agrees with results of previous studies by Chen et al. [5,6].

As shown in Fig. 5.7(d), total dispersoid densities within the irradiation region (at depths ≤1200 nm) are systematically higher than that beyond the irradiated region. The total dispersoid density at 2000 nm is 7.9×10^{22} m^{-3}, while the density at 1000 nm is 1.17×10^{24} m^{-3}, larger by a factor of 15. The much higher dispersoid densities must result from nucleation of new dispersoids. The highest dispersoid density occurs at the dpa peak. Two possible mechanisms can contribute to this: (1) with the highest local dpa rates, the effective diffusivity of solute is peaked. Hence the likelihood of solute clustering for forming new nucleation sites is peaked, and (2) the likelihood of directly breaking large dispersoids into smaller ones is increased in the peak dpa region due to the higher density of damage cascades.

The observation that coherent dispersoids are systematically smaller than incoherent dispersoids within the irradiated region agrees with predictions of Eq. 5.3 in which γ_i of coherent dispersoids is smaller than that of incoherent dispersoids. The

interfacial energy of coherent interfaces was reported by Ribs et al. to be 0.26 - 0.29 J/m^2 [34], while the interfacial energy of incoherent or semi-coherent interfaces was reported by Howe to be 0.3-2.5 J/m^2 energy range [35]. Using the experimentally extracted c (=0.18 %) in the present study as the upper limit of c_r (since r_e in Eq. (2) must be positive), and using the estimated $c\ \infty$ (=0.013% at 475 °C) [36], we obtain the upper limit of γ_i to be about 0.4 J/m^2 in the irradiated region and 1.0 J/m^2 in the damage-free region in the present study.

5.4. Discussion

According to Eq. 5.2 and further assuming that D is a constant without radiation enhancement, the equilibrium dispersoid size r_e should be inversely proportional to the dpa rate K. At depths of 250 nm, 650 nm, and 1000 nm, their dpa rate ratios are 1:1.8:2.6. Figure 5.8 plots the dpa rates. In a comparison, experimentally measured r_e values are roughly a constant. To explain the observations, we believe that solute diffusion must be strongly defect-assisted, as explained below.

At high temperatures in the presence of defect sinks, defect annihilation at the sinks plays a dominant role in determining defect concentrations, and therefore point defect recombination does not contribute as much. Under quasi-steady state condition, local defect reactions are governed by equations [37]

$$\frac{dC_V}{dt} = K - K_{VS}C_SC_V, \text{and } \frac{dC_I}{dt} = K - K_{IS}C_SC_I, \tag{5.4}$$

where C_V, C_I and C_S are vacancy, interstitial and sink concentrations, respectively. K_{VS} and K_{IS} are vacancy-sink reaction, and interstitial-sink reaction rate coefficients,

respectively. Defect populations first increase linearly with irradiation time and approach to an equilibrium steady state with constant defect concentrations expressed by,

$$C_{V_e} = \frac{K}{K_{VS}C_S}, \text{and } C_{I_e} = \frac{K}{K_{IS}C_S} \tag{5.5}$$

On the other hand, for solute atoms which diffuse via interaction with point defects, a general expression of their diffusivity is given by [38]

$$D = f_V D_V C_V + f_I D_I C_I + \cdots \tag{5.6}$$

where f is a weight factor determined by both diffusion mechanism and diffusion correlation. D_V and D_I are the diffusivities of vacancies and interstitials, respectively. The defect-assisted diffusion can extend to other defect types such as di-interstitial or di-vacancy. For simplicity, we ignore the mechanisms involving defect clusters.

Combining Eqs. 5.2, 5.5 and 5.6, we obtain

$$r_e = \frac{\frac{f_V D_V}{K_{VS}} + \frac{f_I D_I}{K_{IS}}}{\psi C_S} \cdot \frac{c - c_r}{c_p - c_r} \tag{5.7}$$

Hence, there is no dependence of r_e on dpa rate *K*.

The defect sinks (C_S) can be dislocations, voids, or oxide dispersoids. In our irradiated samples, voids are not observed due to the good swelling resistance of the alloy matrix. Therefore, the most dominant sinks are the dispersoids themselves. As an approximation, we can use local total dispersoid density to represent C_S and calculate r_e by using Eq. 5.7. As shown in Fig. 5.8, the predicted r_e values are reasonably close to the experimentally measured values.

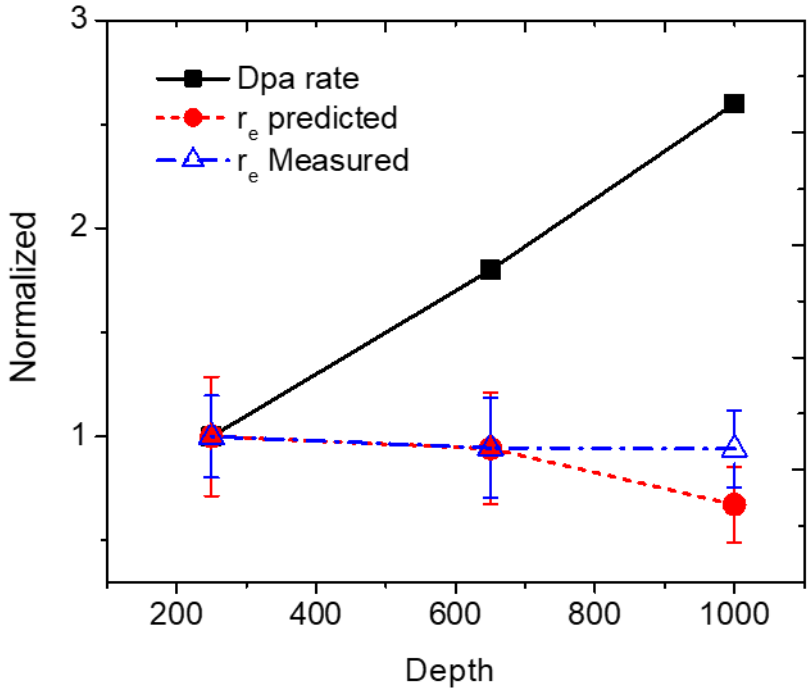

Figure 5.8 Depth dependence of dpa rates, experimentally measured r_e and predicated r_e by using Eq. 7. All values are normalized to that at 250 nm.

For Eq. 5.4, we assume a high temperature condition in which defect recombination contributes less in comparison with defect annihilation at sinks. Hence, interstitial-vacancy recombination is ignored. Even it is not a high temperature condition, Eq. 5.4 is still valid for the case having high density defect sinks such as dispersoids in the present case. In other words, it is valid for the condition that point defects find sinks first before they find their counterpart defects for recombination [37]. For a different and extreme case in which the temperature is low and the defect sink density is also low, defect reactions are governed by the defect creation rate and interstitial-vacancy recombination

only (ignoring defect-sink interaction), the defect reaction equation and the quasi-steady state defect concentration are expressed as [37]

$$\frac{dC}{dt} = K - K_{IV}C^2$$

$$C_e\left(= C_{I_e} = C_{V_e}\right) = \left(\frac{K}{K_{IV}}\right)^{\frac{1}{2}} \tag{5.8}$$

Note in this case, the defect concentrations under quasi-steady state are proportional to $\sqrt{K}$, instead of K. After substituting C_e into Eq. 5.6 for *D*, Eq. 5.2 leads to a r_e dependence on $1/\sqrt{K}$, a dependence which is quite weak. The defect concentrations under quasi-steady states of various conditions (low temperature vs. high temperature and low sink density vs. high sink density) have been systematically summarized by Was [37]. Various conditions lead to either a K dependence or $\sqrt{K}$ dependence of quasi-steady-state defect concentrations. Regardless of the complexity arising from variations in sink density and temperatures, the final r_e becomes either weakly dependent or completely independent of local dpa rates. In both cases discussed (Eqs. 5.5 and 5.8), we assume that quasi-steady states are reached. Our previous studies show that 3.5 MeV ion irradiation of a similar ODS alloy at 475°C leads to saturated dispersoid diameters at doses of 50 peak dpa and beyond [5,6]. Hence, we believe this assumption is valid. Otherwise, dispersoids will continue to evolve under changing defect densities.

Another significant consequence of the present study is to justify the use of ion irradiation to simulate neutron irradiation. If dispersoid sizes have weak or no dependence on dpa rates, then accelerated testing using accelerated ion irradiation can more accurately

predict dispersoid evolution in reactors. However, we need to point out that the currently study is limited to dpa rate differences that are less than one order of magnitude, while dpa rates in accelerator testing are typically a few orders of magnitude higher than those in reactors. Hence, more systematic comparative studies involving larger dpa rates (by adjusting beam current) are needed. Furthermore, there are many other factors affecting dispersoid morphology evolution. Void swelling, for example, may change dispersoid size and density. Small voids can act as nucleation sites of dispersoids. Since we did not observe void swelling in the Hf-doped ODS in the present study, such complexity was not considered. For alloys having high density grain boundaries, such as ODS alloys prepared with extrusion and severe deformation, radiation induced grain growth or radiation induced segregation can change defect sink property, which affects dispersoid stability. Previous studies have shown that radiation induced segregation can affect both voids nucleation and growth [39].

Accelerator-based heavy ion irradiation in general has the complexity including, but not limited to, surface sputtering, surface defect sink effect, injected interstitials, and defect imbalance. Some effects have been recently reviewed by Zinkle and Snead [40]. Due to the fact that these effects are sensitive to detail radiation conditions, we here limit our discussions below to the condition close to the present study. For surface sputtering effect, recent studies by Jing et al. estimated a sputtered thickness of about 14 nm by 100-peak-dpa 3.5 MeV Fe ion irradiation [41], based on sputtering yield calculated from SRIM simulations. The sputtering effect and its impact on damage profile shifting, therefore, are ignorable in the present study. As for surface defect sink effect, it is difficult to tell since

the ODS alloy used in the present study is swelling resistant and we cannot observe void depletion zone. In pure Fe, 3.5 MeV Fe ion irradiation (450°C, 105 peak dpa) creates a 120 nm wide void depletion zone (based on the half width of the zone) [42]. Therefore, assuming defect migration is comparable in Fe and the ODS alloy, the shallowest characterization depth of 250 nm in the present study is away from the surface-affected zone. Under the combined effects from injected interstitials due to extra atoms implanted and defect imbalance due to spatial difference between interstitials and vacancies, void swelling is greatly suppressed at the Fe projected range. Under 100-peak-dpa 3.5 MeV Fe ion irradiation at 450°C, void swelling in pure Fe appears within the region from 120 nm to 825 nm. Therefore, our characterization depths of 250 nm and 650 nm are not affected by both the surface effect and the defect imbalance effect. We further believe the characterization depth of 1000 nm, correspond to the damage peak, is also valuable for the dose rate effect studies due to the following reason. Under defect imbalance effect, the excessive interstitials ($\Delta C = C_I - C_V$) are peaked at about 9×10^4/cm^3 per incident 3.5 MeV Fe ion [42]. This number is much lower than the damage peak (C_I, C_V) of 2.6×10^8/cm^3 [42]. Void swelling is sensitive to defect imbalance (ΔC). But the defect assisted diffusion (Eq. 6) is sensitive to defect densities (C_I, C_V), which are orders of magnitude higher than ΔC. Therefore, the defect imbalance effect (including injected interstitial) plays a weak role in influencing D.

5.5. References

[1] L. K. Mansur, A. F. Rowcliffe, R. K. Nanstad, S. J. Zinkle, W. R. Corwin, R. E. Stoller, Materials needs for fusion, Generation IV fission reactors and spallation neutron sources - similarities and differences, J. Nucl. Mater. 329-333 (2004) 166–172.

[2] G. R. Odette, M. J. Alinger, B. D. Wirth, Recent developments in irradiation-resistant steels, Annu. Rev. Mater. Res. 38 (2008) 471–503.

[3] J. Chen, P. Jung, T. Rebac, F. Duval, T. Sauvage, Y. de Carlan, M. F. Barthe, Helium effects on creep properties of Fe-14CrWTi ODS steel at 650 ºC, J. Nucl. Mater. 453 (2014) 253-258.

[4] J. Chen, P. Jung, W. Hoffelner, H. Ullmaier, Dislocation loops and bubbles in oxide dispersion strengthened ferritic steel after helium implantation under stress, Acta Mater. 56 (2008) 250-258.

[5] T. Chen, E. Aydogan, J. G. Gigax, D. Chen, J. Wang, X. Wang, S. Ukai, F. A. Garner, L. Shao, Microstructural changes and void swelling of a 12Cr ODS ferritic-martensitic alloy after high-dpa self-ion irradiation, J. Nucl. Mater. 467 (2015) 42–49.

[6] T. Chen, J. G. Gigax, L. Price, D. Chen, S. Ukai, E. Aydogan, S. A. Maloy, F. A. Garner, L. Shao, Temperature dependent dispersoid stability in ion-irradiated ferritic-martensitic dual-phase oxide-dispersion-strengthened alloy: Coherent interfaces vs. incoherent interfaces, Acta Mater. 116 (2016) 29-42.

[7] G. R. Odette, Recent progress in developing and qualifying nanostructured ferritic alloys for advanced fission and fusion applications, JOM 66 (2014) 2427-2441.

[8] C. H. Zhang, Y. T. Yang, Y. Song, J. Chen, L. Q. Zhang, J. Jang, A. Kimura, Irradiation response of ODS ferritic steels to high-energy Ne ions at HIRFL, J. Nucl. Mater. 455 (2014) 61-67.

[9] E. Aydogan, N. Almirall, G. R. Odette, S. A. Maloy, O. Anderoglu, L. Shao, J. G. Gigax, L. Price, D. Chen, T. Chen, F. A. Garner, Y. Wu, P. Wells, J. J. Lewandowski, D. T. Hoelzer, Stability of nanosized oxides in ferrite under extremely high dose self-ion irradiations, J. Nucl. Mater. 486 (2017) 86-95.

[10] J. P. Wharry, M. J. Swenson, K. H. Yano, A review of the irradiation evolution of dispersed oxide nanoparticles in the b.c.c. Fe-Cr system: Current understanding and future directions, J. Nucl. Mater. 486 (2017) 11-20.

[11] M. J. Swenson, J. P. Wharry, Nanocluster irradiation evolution in Fe-9%Cr ODS and ferritic-martensitic alloys, J. Nucl. Mat. 496 (2017) 24-40.

[12] X. Liu, Y. Miao, Y. Wu, S. A. Maloy, J. F. Stubbins, Stability of nanoclusters in an oxide dispersion strengthened alloy under neutron irradiation, Scripta Mater. 138 (2017) 57-61.

[13] C. M. Parish, R. M. White, J. M. LeBeau, M. K. Miller, Response of nanostructured ferritic alloys to high-dose heavy ion irradiation, JNM 445 (2014) 251-260.

[14] C. Lu, Z. Lu, X. Wang, R. Xie, Z. Li, M. Higgins, C. Liu, F. Gao, L. Wang, Enhanced radiation-tolerant oxide dispersion strengthened steel and its microstructure evolution under helium-implantation and heavy-ion irradiation, Scientific Reports 7: 40343 (2017).

[15] M. L. Lescoat, J. Ribis, Y. Chen, E. A. Marquis, E. Bordas, P. Trocellier, Y. Serruys, A. Gentils, O. Kaïtasov, Y. de Carlan, A. Legris, Radiation-induced Ostwald ripening in oxide dispersion strengthened ferritic steels irradiated at high ion dose, Acta Mater. 78 (2014) 328-340.

[16] H. Kishimoto, R. Kasada, O. Hashitomi, A. Kimura, Stability of Y-Ti complex oxides in Fe-16Cr-0.1Ti ODS ferritic steel before and after heavy-ion irradiation, J. Nucl. Mater. 386e388 (2009) 533-536.

[17] R. S. Nelson, J. A. Hudson, D. J. Mazey, The stability of precipitates in an irradiation environment, J. Nucl. Mater. 44 (1972) 318–330.

[18] C. Wagner, Theory of the ageing of precipitates by redissolution (Ostwald maturing), Z. Elektrochem 65 (1961) 581–591.

[19] K. Vortler, M. Mamivand, L. Barnard, I. Szlufarska, F. A. Garner, D. Morgan, Simulated spatial and temporal dependence of chromium concentration in pure Fe and Fe-14%Cr under high dpa ion irradiation, J. Nucl. Mater. 479 (2016) 23-35.

[20] T. Ezawa and E. Wakai, Radiation-induced solute segregation in Al and Ni binary alloys under HVEM irradiation, Ultramicroscopy 39 (1991) 187-196.

[21] T. Okuda, M. Fujiwara, T. Nakai, K. Shibata, A. Kimura, M. Inoue, S. Ukai, S. Ohnuki, T. Fujisawa, F. Abe, Super ODS steels R&D for fuel cladding of next generation nuclear systems, 3; Development of high performance attrition type ball mill, Proc. Int. Conf. on Advanced Power Plant, Tokyo, Japan, May 10-14 (2009) Paper 9229.

[22] T. Furukawa, S. Ohtsuka, M. Inoue, T. Okuda, F. Abe, S. Ohnuki, T. Fujisawa and A. Kimura: Proc. Int. Conf. on Advanced Power Plant, Tokyo, Japan, May 10–14 (2009) Paper 9221.

[23] F. A. Garner, M. B. Toloczko, B. H. Sencer, Comparison of swelling and irradiation creep behavior of fcc-austenitic and bcc-ferritic/martensitic alloys at high neutron exposure, J. Nucl. Mater. 276 (2000) 123-142.

[24] F. A. Smidt Jr., P. R. Malmberg, J. A. Sprague, J. E. Westmoreland, Swelling behavior of commercial ferritic alloys, EM-12 and HT-9, as assessed by heavy ion bombardment, vol. STP 611, ASTM International, Philadelphia, PA, 1976, pp. 227-241.

[25] E. Aydogan, T. Chen, J. G. Gigax, D. Chen, X. Wang, P. S. Dzhumaev, O. V. Emelyanova, M. G. Ganchenkova, B. A. Kalin, M. Leontiva-Smirnova, R. Z. Valiev, N.

A. Enikeev, M. M. Abramova, Y. Wu, W.Y. Lo, Y. Yang, M. Short, S. A. Maloy, F. A. Garner, L. Shao, Effect of self-ion irradiation on the microstructural changes of alloy EK-181 in annealed and severely deformed condition, J. Nucl. Mat. 487 (2017) 96-104.

[26] J. G. Gigax, T. Chen, Hyosim Kim, J. Wang, L. M. Price, E. Aydogan, S. A. Maloy, D. K. Schreiber, M. B. Toloczko, F. A. Garner, L. Shao, Radiation response of alloy T91 at damage levels up to 1000 peak dpa, J. Nucl. Mater. 482 (2016) 257-265.

[27] J. G. Gigax, E. Aydogan, T. Chen, D. Chen, Y. Wu, W. Y. Lo, Y. Yang, F. A. Garner, The influence of beam rastering on the swelling of self-ion irradiated pure iron at 450°C, J. Nucl. Mater. 465 (2015) 343-348.

[28] J. G. Gigax, H. Kim, E. Aydogan, F. A. Garner, S. A. Maloy, L. Shao, Beam-contamination-induced compositional alteration and its neutron-atypical consequences in ion simulation of neutron-induced void swelling, Mater. Res. Lett. 5 (2017) 478-485.

[29] L. Shao, J. G. Gigax, D. Chen, H. Kim, F. A. Garner, J. Wang, M. B. Toloczko, Standardization of accelerator irradiation procedures for simulation of neutron induced damage in reactor structural materials, Nucl. Instr. Meth. Phys. Res. B 409 (2017) 251-254.

[30] J. F. Ziegler, M. D. Ziegler, J. P. Biersack, SRIM – the stopping and range of ions in matter, Nucl. Instr. Meth. Phys. Res. B 268 (2010).

[31] R. E. Stoller, M. B. Toloczko, G. S. Was, A. G. Certain, S. Dwaraknath, F. A. Garner, On the use of SRIM for computing radiation damage exposure, Nucl. Instr. Meth. Phys. Res. B 310 (2013) 75-80.

[32] C. Lu, Z. Lu, R. Xie, Z. Li, C. Liu, L. Wang, Effect of Y/Ti atomic ratio on microstructure of oxide dispersion strengthened alloys, Materials Characterization 134 (2017) 35-40.

[33] P. Dou, A. Kimura, R. Kasada, T. Okuda, M. Inoue, S. Ukai, S. Ohnuki, T. Fujisawa, F. Abe, S. Jiang, Z. Yang, TEM and HRTEM study of oxide particles in an Al-alloyed high-Cr oxide dispersion strengthened ferritic steel with Hf addition, J. Nucl. Mat. 485 (2017) 189-201

[34] J. Ribis, Y. de Carlan, Interfacial strained structure and orientation relation- ships of the nanosized oxide particles deduced from elasticity-driven morphology in oxide dispersion strengthened materials, Acta Mater. 60 (2012) 238–252.

[35] J. M. Howe, Interfaces in materials, Wiley-Interscience, 1997.

[36] H. Okamoto, Journal of Phase Equilibria 16 (1995) 473.

[37] G. S. Was, Fundamentals of Radiation Materials Science: Metals and Alloys, Springer, 2007 p.218.

[38] M. Nastasi, J. Mayer, J. K. Hirvonen, Ion-solid interactions: fundamentals and applications, Cambridge University Press, New York, 1996.

[39] W. G. Wolfer and L. K. Mansur, J. Nucl. Mat. 91 (1980) 265.

[40] S. J. Zinkle and L. L. Snead, Opportunities and limitations for ion beams in radiation effects studies: Bridging critical gaps between charged particle and neutron irradiations, Scripta Materialia 143 (2018) 154-160.

[41] J. Wang, M. B. Toloczko, N. Bailey, F. A. Garner, J. G. Gigax, L. Shao, Modification of SRIM-calculated dose and injected ion profiles due to sputtering, injected ion buildup and void swelling, Nucl. Instrum. Methods in Phys. Res. B 387 (2016) 20-28.

[42] L. Shao, C. C. Wei, J. Gigax, A. Aitkaliyeva, D. Chen, B. H. Sencer, F. A. Garner, Effect of defect imbalance on void swelling distributions produced in pure iron irradiated with 3.5 MeV self-ions, J. Nucl. Mat. 453 (2014) 176-181.

6. CONCLUSIONS

6.1. Oxide Dispersoid Coherency Study on 12Cr ODS Alloy

The 100 peak dpa self-ion irradiation is carried out on dual-phase 12Cr ODS with 3.5 MeV Fe^{2+} at 475 °C to see the different behaviors on coherent and incoherent dispersoids in ferrite and tempered martensite phases. In ferrite grain, both coherent and incoherent dispersoid sizes were stable under irradiation. However, coherent dispersoid density increased dramatically at 500-800 nm depth indicating newly nucleated or precipitated dispersoid will mostly take coherent relationship with matrix. In martensite grain, almost all large incoherent dispersoids disappeared after irradiation, but the densities of both coherent and incoherent dispersoid just showed slight increase.

This stability of coherent oxide dispersoids and increment of density under irradiation demonstrates why ODS alloys show good creep strength under high dose irradiation and high swelling resistance.

6.2. He Preimplantation Study on 12Cr ODS Alloy

The 12Cr ODS alloy samples were irradiated by using 3.5 MeV Fe^{2+} beam with and without He preimplantation to see the effect of pre-existing He bubble on oxide dispersoid nucleation. The coherent oxide dispersoid size did not change much under irradiation, and He preimplantation did not affect on dispersoid size either. However, 1E15 He preimplanted sample showed higher oxide dispersoid density at 350 nm depth

compared to Fe irradiated sample without He preimplantation. This suggests that He bubbles in the matrix worked as a nucleation site for new oxide dispersoids during Fe irradiation, increasing oxide dispersoid density. However, 1E16 He preimplanted and Fe irradiated sample showed systematically lower dispersoid density than Fe irradiated sample, implying large He bubbles do not affect on dispersoid nucleation during Fe irradiation.

The experiment result was supported by studies on helium, vacancy and vacancy-oxygen affinity. As helium has low migration energy, it can be trapped to vacancy and form He-vacancy clusters in the matrix. Since vacancy has high affinity on oxygen, they form He-vacancy-oxygen rich cluster, which further attracts other solutes like Ti and Y, nucleating oxide dispersoids. The increment of coherent dispersoid density of 1E15 He + Fe case can be explained with this mechanism. The 1E16 He + Fe case, however, did not show the increase in density and we believe that the large surface area and volume of average 3.4 nm diameter He bubble make the solute concentration not to reach the critical nucleation limit.

6.3. Dpa Rate Study on Hf Doped ODS Alloy

The Hf-doped ferrite ODS alloy was irradiated using 3.5 MeV Fe^{2+} ion at 475 °C up to 100 peak dpa. The dispersoid coherencies, sizes and densities at different depths were characterized. Both coherent and incoherent dispersoid sizes shrunk in the ion range and the incoherent dispersoid sizes were larger than those of coherent dispersoids at all depths. The densities were increased in the ion range for both coherent and incoherent

dispersoids and the coherent dispersoid densities were higher than those of incoherent dispersoids. Despite of the dpa rate differences at each depth, the dispersoid sizes do not show noticeable depth dependent changes in the experiment. To explain this, defect-assisted-diffusion mechanisms were introduced, showing dispersoid size has weak or no dependence on dpa rate. Although the dpa rate differences in this study were much smaller than that between the real reactor environment and the accelerator test, the present study shows the possibility of using ion irradiation to simulate neutron irradiation on studying dispersoid stability in ODS alloys.